Towards Simulations of Self-propelled Janus Particles in a Critical Binary Mixture

Inaugural-Dissertation
zur
Erlangung des Doktorgrades

der Mathematisch-Naturwissenschaftlichen Fakultät
der Universität zu Köln

vorgelegt von

Fatemeh Alidadi Soleymani

aus Isfahan, Iran

Jülich 2019

Berichterstatter: **Prof. Dr. Gerhard Gompper**
Prof. Dr. Andreas Schadschneider

Tag der mündlichen Prüfung: 21.02.2019

Declaration

I hereby declare that except where specific reference is made to the work of others, the contents of this dissertation are original and have not been submitted in whole or in part for consideration for any other degree or qualification in this, or any other university. This dissertation is my own work and contains nothing which is the outcome of work done in collaboration with others, except as specified in the text and Acknowledgements. This dissertation contains fewer than 65,000 words including appendices, bibliography, footnotes, tables and equations and has fewer than 150 figures.

Fatemeh Alidadi Soleymani
Jülich 2019

Acknowledgements

This thesis is an outcome of lots of supports and guides. At this stage, I would like to thank all of the people helped me during my Ph.D. study.

I acknowledge my thesis committee: Prof. Dr. Gerhard Gompper, Prof. Dr. Andreas Schadschneider, and Prof. Dr. Annette Schmidt. I want to express my deep gratitude to Gerhard for providing me an opportunity to work on this project and also to attend many conferences.

My research would have been impossible without the aid and support of Dr. Dmitry Fedosov. Dmitry, I am profoundly grateful for all of your help and being friendly and open-minded about new ideas. I am extremely thankful to Dr. Marisol Ripoll for worthwhile suggestions and feedback. Marisol, I appreciate you for the time you spend on my project and all of your guides.

I would like to thank all ICS-2 members for discussions during my entire Ph.D. I am also very grateful to Sebastian Hillringhaus who translates the abstract to German. I thank Forschungszentrum Jülich for providing to me all the facilities and cluster computing and supercomputing center.

Heartfelt thanks go to my husband, Mohsen who is there for me always and encourages me all the time. My love, I appreciate your infinite kindness and supports.

Abstract

Artificial microswimmers have recently received a lot of attention due to the large number of applications in the development of biomimetic materials, microfluidic devices, and micromachines. A promising strategy to build such synthetic swimmers is based on phoretic phenomena. Phoresis refers to a directed particle motion in the presence of an external gradient. Janus particles generate a stable local gradient by an asymmetric structure which results in a self-propelled phoretic motion.

One of the interesting examples is a half-metal coated Janus particle in a critical binary mixture under laser irradiation. In the vicinity of the metallic cap, the temperature may be above the critical temperature and a droplet is formed at the Janus particle surface, such that propulsion is created. Although various theoretical studies have already investigated this system, simulations are still lacking. Providing a suitable simulation technique enables us to predict the behavior of more complicated cases which are not possible with theory e.g. a Janus particle in blood flow. Simulation of this system requires a technique which satisfies the three requisites at the same time: transport of mass and energy, phase separation and large size particles modeled during a large simulation time. A mesoscopic simulation technique that can achieve all these requirements is dissipative particle dynamics with energy conservation (DPDe). In this thesis, the DPDe technique is employed, and further developed to investigate this system.

The starting point is the validation of the previously suggested DPDe. Although DPDe was designed to exactly conserve energy, significant drift of the total energy has been reported by using different algorithms. Here, an efficient integration scheme with velocity Verlet algorithm is used such that energy is conserved on the order of machine precision. Simulation results of mass and energy transport are verified by analytical approaches.

Then, a partially heated Janus particle in a simple fluid is modeled as a thermophoretic particle. A pressure gradient, which is generated at the colloid poles as a consequence of temperature gradient, propels the particle. The direction of motion and its magnitude are determined mainly by the details of the interaction between fluid and colloid and, the Peclet number changes one order of magnitude. Interestingly, fluid properties such as viscosity,

conductivity, etc. affect propulsive velocity but the related Peclet number does not change significantly.

A proper method necessitates in order to model a binary mixture near the critical point which involves the wetting phenomenon in the presence of a solid surface (Janus particle). The conservative force used in the original DPD cannot fulfill this promise. Therefore, a short-range repulsive and long-range attractive interaction is employed for the conservative force which succeeds in matching the properties of real physical systems, such as correct phase behavior with respect to temperature, sufficiently large surface tension to form a stable droplet in a flow, and the inclusion of varying wetting properties.

Using the improved DPDe method, a Janus particle immersed in a binary mixture is simulated, in which droplet size, wetting properties, and surface tension can be varied by the model parameters. The value of the resulting propulsive velocity is mainly determined by the size of the adhering droplet. In agreement with experiments, a colloid with a smaller droplet displays larger propulsion, and a Janus with a very large droplet shows eventually motion in the reverse direction, this is towards the hot cap. Although the number fraction of binary mixture and the magnitude of the temperature gradient are the main parameters to determine the droplet size, a smaller surface tension also results in a smaller droplet. Besides, the shape of the droplet is influenced by the contact angle and affects the propulsion strength.

Kurzzusammenfassung

Künstliche Mikroschwimmer haben aufgrund der großen Zahl an Anwendungen in der Entwicklung von biomimetischen Materialien, mikrofluidischen Geräten und anderen Mikromaschinen in letzter Zeit viel Aufmerksamkeit erfahren. Eine vielversprechende Möglichkeit, diese Schwimmer zu produzieren beruht auf phoretischen Phänomenen. Phoresis bezieht sich dabei auf eine gerichtete Bewegung von Partikeln in Gegenwart eines externen Gradienten. Janus-Partikel erzeugen durch eine asymmetrische Struktur auf ihrer Oberfläche einen stabilen und lokalen Gradienten, der zu einer selbst angetriebenen, phoretischen Bewegung führt.

Ein interessantes Beispiel sind Janus-Partikel, die zur Hälfte mit Metall beschichtet sind, in einer kritischen binären Mischung, die durch Laser bestrahlt werden. In der Nähe der Metallkappe kann die Temperatur über der der kritischen Temperatur liegen, wodurch sich ein Tröpchen an der Oberfläche des Janus Teilchens bildet, das einen Antrieb erzeugt. Diese Art von Systemen wurden bereits in theoretischen Studien untersucht, es fehlen allerdings noch Simulationen. Um diese Systeme zu simulieren, muss die angewendete Technik drei Aspekte über einen langen Simulationszeitraum modellieren können: Massen- und Energietransport, Phasenseparation und die Simulation von großen Teilchen. Eine geeignete Technik ist die *dissipative particle dynamics* Methode mit Energieerhaltung (DPDe), welche in dieser Arbeit verwendet und weiterentwickelt wird.

Zu Beginn wird die ursprüngliche DPDe verwendete Methode auf ihre Eigenschaften getestet, da in verschiedenen Arbeiten mit unterschiedlichen Algorithmen entgegen der Konzipierung ein signifikanter Drift der Gesamtenergie gezeigt wurde. Durch die Verwendung einer effizienten Integrationsroutine basierend auf dem Verlet Algorithmus kann die Energie bis auf Maschinengenauigkeit erhalten werden. Weiter werden die Simulationsergebnisse bezüglich Massen- und Energietransport mit analytischen Ergebnissen verglichen und bestätigt.

Um ein thermophoretisches Teilchen zu modellieren, wird ein teilweise erhitztes Janus-Partikel in einer einfachen Flüssigkeit verwendet. Dieses wird durch einen Druckgradienten angetrieben, der durch den Temperaturgradienten an den Polen des Janus-Partikels erzeugt wird. Die Richtung der Bewegung sowie die Geschwindigkeit hängt dabei am meisten von

den Details der Wechselwirkung zwischen Flüssigkeit und Teichen ab. Die bewegung wird durch die Peclet-Zahl charakterisiert, welche sich um bis zu einer Größenordnung unterscheiden kann. Interessanterweise beeinflussen verschiedene Eigenschaften der Flüssigkeit wie die Viskosität oder die Leitfähigkeit die Antriebsgeschwindigkeit des Teilchen, ohne dabei wesentlich die Peclet-Zahl zu verändern.

Um eine binäre Mischung in der Nähe des kritischen Punktes unter Berücksichtigung von Benetzungphänomenen an einer harten Oberfläche (Janus-Partikel) zu modellieren, wird eine angepasste Simulationsmethode benötigt, da die konservative Kraft der originalen DPD Methode nicht geeignet ist. Daher wird eine kurzreichweitige, abstoßende Kraft sowie eine langreichweitige, anziehende Kraft verwendet, die erfolgreich die Eigenschaften von physikalischen Systemen darstellen kann. Dies beinhaltet das korrekte Phasenverhalten bei verschiedenen Temperaturen, ausreichend große Oberflächenspannungen, um stabile antreibende Tröpfenchen auch im Fluss zu formen, sowie die Einbeziehung verschiedener Benetzungseigenschaften.

Damit wird dann ein Janus-Partikel simuliert, das von einer binären Mischung umgeben ist. Hierbei wird die verbesserte DPDe Methode verwendet wobei Tröpfchengröße, die Benetzungseigenschaften sowie die Oberflächenspannung durch Simulationsparameter verändert werden können. Die resultierende, antreibende Geschwindigkeit wird dabei hauptsächlich durch die Tröpfchengröße beeinflusst, wobei Partikel mit einem kleineren Tröpfchen einen stärkeren Antrieb zeigen als gleiche Partikel mit größeren Tröpfchen. In Übereinstimmung mit Experimenten zeigen große Tröpfchen sogar einen Antrieb in die entgegengesetzte Richtung. Die entscheidenden Parameter für die Tröpfchengröße sind das Mischlungsverhältnis der binären Flüsigkeit sowie die Steigung des Temperaturgradienten, aber auch die Oberflächenspannung trägt bei. Neben der Größe beeinflusst auch die Form des Tröpfchens die Stärke des Antriebes, wobei die Form vom Kontaktwinkel zwischen Tröpfchen und Partikel abhängt.

Table of contents

List of figures **xv**

List of tables **xix**

Nomenclature **xxi**

1 Introduction **1**
1.1 Active Particles 1
1.2 Thermophoresis 3
1.2.1 Experiments on Thermodiffusion 5
1.2.2 Theory of Thermodiffusion 6
1.2.3 Simulations 9
1.2.4 Applications of Thermophoresis 10
1.3 Hydrodynamics 12
1.4 Outline of the thesis 14

2 Simulation Methods **17**
2.1 Molecular Dynamics and Mesoscopic Simulation 17
2.2 Energy Conserving Method 23
2.2.1 Dissipative Particle Dynamics with Energy Conservation 24
2.2.2 DPDe Variations 26
2.2.3 Integration of DPDe Equations 27
2.3 Implementation of a Temperature Gradient 28

3 Consistency Check of Various Approaches in DPDe **31**
3.1 General Consideration 31
3.2 Fluid at a Homogeneous Temperature 31
3.2.1 Simulation Setup and Parameters 31
3.2.2 Validation of Models 32

3.3 Fluid Under an Inhomogeneous Temperature 36
3.3.1 Implementation of a Thermal Gradient 36
3.3.2 Characterization of Heat Transfer 37
3.3.3 Heat Transfer 40
3.3.4 Analytical Approach to Energy Transfer 41
3.4 Energy Stability 46
3.5 Calculation of the Relevant Dimensionless Numbers 46
3.6 Summary 50

4 Thermophoretic Janus Colloid **53**
4.1 Simulation of Janus Colloid 53
4.2 Thermodynamic Properties 55
4.3 Propulsive Velocity 58
4.4 Rotational Dynamics 63
4.4.1 Einstein Relation for Rotational diffusion in 2D 64
4.5 Force Field in the Fluid and Total Force on Colloid 66
4.6 Measuring Friction Factor and Thermal Diffusion Factor 68
4.6.1 Soret Coefficient 71
4.7 Effect of Simulation Parameters on the Peclet Number 71
4.8 Effect of Attraction Interaction between Colloid and Fluid 77
4.9 Summary 79

5 Binary Mixture **81**
5.1 Model Implementation 83
5.2 Critical Point 83
5.2.1 Analysis of Phase Transition 83
5.3 Surface Tension 86
5.3.1 Young–Laplace Equation in 2D 86
5.3.2 Effect of Attraction Interaction of Fluid-Fluid 88
5.4 Contact Angle 91
5.5 Summary 94

6 Heated Janus Colloid in a Binary Mixture **95**
6.1 Simulation Setup 95
6.1.1 Method 95
6.1.2 Implementation of Temperature Gradient 96
6.2 Velocity Field 98

6.3 Effect of Number Fraction 98
6.4 Effect of Wetting 99
6.5 Effect of Temperature Gradient 101
6.6 Effect of Surface Tension 103
6.7 Summary 105

7 Conclusions and Outlook **107**

References **111**

Appendix A Distribution Function in Microcanonical Ensemble **123**

Appendix B Colloid-Solvent Boundary Conditions **125**

List of figures

1.1 Microscopic images of several unicellular swimming organisms (a) Oplina (b) The Salmonella bacteria (c) Photobacterium profundum. 2
1.2 Examples of artificial microswimmers (a) An artificial sperm (b) Diffusiophoresis particle 3
1.3 Examples of thermophoretic microswimmer (a) Asymmetric micrograer (b) Janus particle under a rotating electric field (c) Janus in a critical binary mixture (d) Assembling of thermophoretic dimers 4
1.4 Schematic picture of Soret effect 5
1.5 Temperature dependence of the Soret coefficient for (a) aqueous suspensions of polystyrene with different particle sizes. (b) Poly(N-isopropylacrylamide) (PNiPAM) chain in water. 6
1.6 Typical MST experiment 11

2.1 One DPD particle represents several atoms or molecules. 21
2.2 Weight functions for various values of the exponent s. 22

3.1 Time evolution of total energy 33
3.2 Kinetic temperature T_K and internal temperature T_I along the box length with periodic boundary conditions for two different timesteps. 35
3.3 Radial distribution function for different time 36
3.4 implantation of temperature gradient 37
3.5 Steady-state density profiles for the same thermal gradients of different models. 38
3.6 Temperature profiles for different heat rate $\dot{Q}$. The larger $\dot{Q}$ leads to the larger temperature gradient. 39
3.7 Heat conduction coefficient as a function of (a) temperature and density for the weak thermal gradients (b) heat flux $\dot{Q}$ 39
3.8 Ratio of energy transfer through a plane by different ways 40

3.9 Conduction and internal energy contribution to the energy transfer as a function of heat rate (a) at the two measuring planes (b) for different models. 41
3.10 Integration domain for the heat conduction 42
3.11 Collision time versus temperature over density 45
3.12 Velocity profile for the reverse-Poiseuille flow 48

4.1 Schematic diagram of the immersed Janus particle in simple fluid 54
4.2 (a) Streamlines of the flow in the temperature field of Janus particle (b) The heat exchange around the colloid 55
4.3 The temperature profile as a function of the angle and distance for the cases (a) $\kappa_0^{ff} = 0.001$ and (b) $\kappa_0^{ff} = 0.1$. 56
4.4 The normalized temperature as a function of the radial distance for axes with angles $\pi/2$ and $3\pi/2$. The temperature linearly increases (decreases) at the cold (hot) sides. 57
4.5 Pressure and density profiles around the Janus particle 57
4.6 (a) Density and (b) pressure profiles as a function of distance from center of the colloid 58
4.7 Normal shear stress profiles at $\pi/2$ and $3\pi/2$ (a) τ_{xx} and (b) τ_{yy}. Close to the colloid surface τ_{xx} and τ_{yy}, have different values but far from it they are equal. 59
4.8 Schematic drawing of the fluid particles (blue) close to the wall (green particles). 59
4.9 Shear stress as a function of angle at various distances from the center of colloid. 60
4.10 Propulsive velocity for different interactions between colloid and fluid for two cases: (a) non-ideal fluid and (b) ideal fluid. 61
4.11 Propulsive velocity as a function of DPD conservative interaction between colloid and fluid 62
4.12 Propulsive velocity as a function of time 62
4.13 Dependence of the propulsive velocity on the temperature gradient 63
4.14 Auto correlation function of the orientation vector 64
4.15 Rotational diffusion as a function of colloid size 66
4.16 Dynamic viscosity and rotational diffusion as a function of average temperature 66
4.17 Force profiles in the colloid frame $x' - y'$ as a function of the angle and distance (a and c) and as a function of the distance at $\theta = \pi/2$ and $\theta = 3\pi/2$ (b), and for two directions at $\theta = 0$ and $\theta = \pi$ (d). 67
4.18 Uniform flow around a fixed colloid for measuring the friction factor γ_f. . . 68

4.19 Dependence of the thermal diffusion factor α_T and friction coefficient γ_f on (a) number of colloid particles at the colloid surface, (b) mass of the fluid particles, (c) conductivity coefficient of fluid, (d) colloid radius, (e) average temperature, (f) random force coefficient. 70
4.20 Dependence of the Soret coefficient on temperature. 71
4.21 Peclet number of the Janus particle as a function of the size of colloid for the same temperature gradient $\nabla T = \text{const}$ and same temperature difference $\Delta T = \text{const}$. 76
4.22 Propulsive velocity and Peclet number as a function of temperature when (a) $\Delta T = \text{const}$. and (b) $\Delta T/\bar{T} = \text{const}$.. 76
4.23 Potential (a) and conservative force (b) with cubic spline weight function in equation (4.24) where $A = 2, B = 1.05$ and $a_{ij} = 6$. 78

5.1 A schematic phase diagram for water–2,6-lutidine as an example of binary mixture. 82
5.2 An active Brownian micro-swimmer in a critical binary mixture. 82
5.3 Gaussian distribution function fitted to the measured density distribution where $\varphi_{\mathrm{A}} = \varphi_{\mathrm{B}}$ 84
5.4 Gaussian distribution function fitted to the measured density distribution where $\varphi_{\mathrm{A}} = 0.25\varphi_{\mathrm{B}}$ 85
5.5 Variance and mean values of the density distribution function as a function of repulsion between A and B type for number fraction (a) $\varphi_A = \varphi_B$ (b) $\varphi_A = 0.25\varphi_B$ 86
5.6 (a) Density and (b) pressure profiles as a function of distance from the center of the drop 87
5.7 Steady drop profile in the periodic channel in the x direction (a) when there is no flow and (b) under shear flow. 88
5.8 Surface tension as a function of the strength of interaction force. 90
5.9 The droplet size and surface tension as a function of number fraction φ_A. . 90
5.10 Performance of a steady drop in shear flow. 91
5.11 Schematic of a drop and definition of contact angle 92
5.12 Measurement of contact angle 93
5.13 Contact angle as a function of the potential coefficient for different number fractions. 93
5.14 Contact angle as a function of the potential coefficient between the wall and fluid for two different surface tensions. 94

6.1 Temperature profile around a heated colloid in a critical binary mixture for the three different ways of implementing temperature gradient: (*i*) temperature fixed at two caps (blue), (*ii*) heat rate fixed at two caps (green) and (*iii*) heating on the colloid while cooling is performed in whole fluid (magenta). The maximum temperature is fixed to $T_h = 0.83$ for all cases. 97
6.2 Temperature fields for the three cases when (a) temperature of colloid particles is fixed at high and low values, (b) colloid particle are cooled down and heated up with a constant heat rate, (c) half of the colloid is heated up and the fluid far from the colloid surface is cooled down with a constant heat rate. The Janus colloid is shown by white color. 97
6.3 Flow streamlines and the temperature profile around a Janus colloid immersed in a binary mixture close to the critical point with a droplet in the vicinity of the hot cap. (a) Simulation with DPDe. (b) Numerical solution of Navier–Stokes equation 98
6.4 Peclet number as a function of number fraction for different methods of implementing temperature gradient 100
6.5 Propulsive velocity as a function of contact angle for (a) various sizes of the droplet with a fixed temperature on the Janus particle and (b) for different temperature control strategies. 101
6.6 Size of the droplet (blue) and density inside the droplet (red) as a function of temperature gradient for the number fraction fixed at $\varphi_A = 0.01$ and with the fixed temperature strategy. 102
6.7 (a) Temperature difference as a function of heat rate and (b) propulsive velocity as a function of temperature difference 102
6.8 (a) Density in a drop and (b) drop size as a function of number fraction for two different surface tensions. 104
6.9 Peclet number as a function of the strength of interactions between unlike fluids. 105
6.10 Peclet number as a function of number fraction for two different surface tensions. 105
6.11 Peclet number as a function of wetting (potential coefficient between the wall and fluid) for two different surface tensions. 106

B.1 Schematic diagram of the immersed Janus in simple fluid 125

List of tables

1.1 Reynolds number of several swimmers in water. 14

3.1 Temperature profile data for different models. Presented values are valid for both q^E and q^{RE} models. 37
3.2 Comparison of analytical approach and simulation data for heat conduction. 43
3.3 Comparison of analytical approach and simulation data for heat transfer by internal energy. 46
3.4 Schmidt and Prandtl numbers of some liquids [1–3] 49
3.5 Transport coefficients in SI units for some relevant liquids at room condition together with the corresponding Prandtl and Schmidt numbers. 50

4.1 Effect of s exponent on Peclet number. 72
4.2 Relation between σ and Peclect number. 72
4.3 Fluid conductivity and Peclet number. 73
4.4 Effect of heat conduction at the interface of colloid on Peclet number. . . . 73
4.5 Cutoff radius of fluid interaction affects weakly the Peclet number 73
4.6 The system size is scaled and the Peclet number increases 74
4.7 Cut off radius for the colloid and fluid interaction and Peclet number 74
4.8 Density of particles representing the colloid does not change Peclet number 75
4.9 Particle mass does not affect the Peclet number 75

6.1 Droplet shape for different droplet sizes 99
6.2 Droplet shape for different contact angles 100
6.3 Droplet shape for different surface tension 104

Nomenclature

A	area
A_d	area occupied by a drop
C_{LJ}	shift parameter of LJ
C_P	specific heat capacity of constant pressure
C_v	specific heat capacity of constant volume
Dr	rotational diffusion
E_{mec}	mechanical energy
E_{tot}	total energy
F^D	dissipative force
I, Υ, ε	internal energy
K	kinetic energy
N	number of particles
N_c	number of particles on colloid
PE	potential energy
Pr	Prandtl number
R	radius of Janus
$Rot(\theta)$	rotation matrix
T_I	internal temperature

T_k	kinetic temperature
V	volume
Γ	interfacial energy
Ω	angular velocity
α_T	thermal diffusion factor
α	surface tension
$\bar{x}$	average value of variable x
β	compressibility
ε_{LJ}	depth of LJ potential well
ε	internal energy
γ	friction amplitude
κ	conductivity coefficient
ω	weight function
ψ_B	Boltzmann distribution function
ψ	distribution function
σ_{LJ}	interaction length parameter of LJ
σ_{var}	variance
θ_C	contact angle
ξ	Gaussian white noise
a_{ij}	conservative force coefficient
f_D	drag force
$g(r), RDF$	radial distribution function
n	number density
r_c	cutoff radius

v_p	propulsive velocity
D	diffusion coefficient
D_T	thermal diffusion coefficient
D_m	interdiffusion coefficient
$E_{I,C,PE,K}$	energy transfer by I, C, PE, K
F^C	conservative force
G	Gibbs energy
H_k	partial molar enthalpy
J'_q	measurable heat flux
J_k	flux of particle type k
J_m	mass flux
J_q	total heat flux
J_s	entropy flux
M	torque
P	pressure
Re	Reynolds number
S	entropy density
S_T	Soret coefficient
S_k	partial molar entropy
Sc	Schmidt number
T	temperature
U	conservative potential
V_k	partial molar entropy
X	tensor of force

Δt	timestep
Σ	entropy production
Υ	internal energy of system
$\delta(x-x')$	Dirac delta function
δ_{ij}	Kronecker delta
$\delta x, \delta y, \delta z$	length element
$\dot{Q}$	heat rate
$\dot{\gamma}$	strain rate tensor
$\dot{r}, v, \mathbf{v}$	velocity
η	dynamic viscosity
γ_f	friction coefficient
κ_0	mesoscopic conduction coefficient
λ_{MFP}	mean free path
λ	bulk viscosity
$\mathrm{d}S_x, \mathrm{d}S_y$	displacement
μ_k	chemical potential
ρ	fluid density
σ	noise amplitude
τ_0	time unit
τ_c	collision time
τ_i	inertial time scale
τ	stress
$\mathbf{f}_R, \mathbf{F}_R$	random force
$\mathbf{f}_{ext}$	external force

$\mathbf{f}_{sur}$	surface force
$\mathbf{f}_v$	viscous force
$\mathbf{r}$	Position
θ	angle
φ_k	number fraction
c_v	heat capacity at constant volume
f_T	thermophoretic force
f_r	rotational friction factor
k_B	Boltzmann constant
m	mass
s	exponent of the weight function
s_m	source of mass
t	time
$u(t)$	orientation vector
LJ	Lennard-Jones

Chapter 1

Introduction

1.1 Active Particles

There is a wide range of examples of diffusion in nature from diffusion of tiny dust particles in a room to diffusion of calcium through bones and diffusion of charges in a semiconductor. Particles which are able to convert environmental energy to a targeted motion are called active Brownian particles. Active Brownian particles are able to move in a specific direction using some propulsion mechanisms but show a diffusive behavior at long times due to e.g. the presence of rotational diffusion. Active motion is crucial for many biological systems for example in search of food (chemotaxis) [4] or light (phototaxis) [5] or in response to infections [6]. Figure 1.1 illustrates several bacteria as examples of microswimmers moving by the activation of flagella.

Man-made swimmers at nano and micro scale are widely studied in experiments [10–13], simulations [14–16] and theories [17–19] due to their potential application in drug delivery [20–22], as micro and nanomachines in fluid [23–25] or as a substitution of microorganisms [26–31]. Artificial sperm [32] and bacteria [33] are examples of self-propelled swimmers which move by different physical mechanisms. Note that many living cells propel themselves due to interactions at their surface [34]. A field gradient such as concentration, temperature or electric field gradients is one of the mechanisms which leads to the propulsion of a swimmer. Motion in the concentration and temperature gradients are called respectively diffusiophoresis [15, 35–37] and thermophoresis phenomenon [15, 38–40]. Several examples of artificial microswimmers are shown in figure 1.2. Figure 1.2a presents an artificial sperm constructed as an elastic filament with a rigid head and a small single cluster of contractile cells between the head and tail which generate propulsion. Diffusiophoretic Janus particle is shown in figure 1.2b. This particle with a meso-porous structure on its coated cap propels

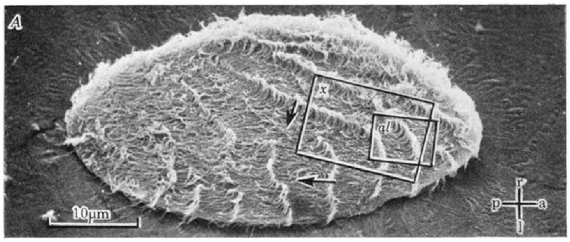

(a)

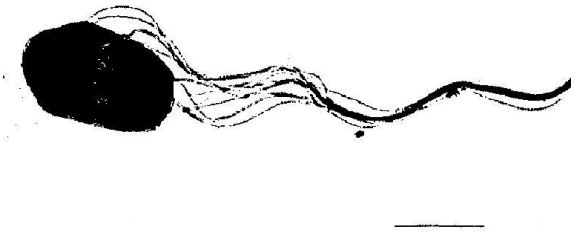

(b)

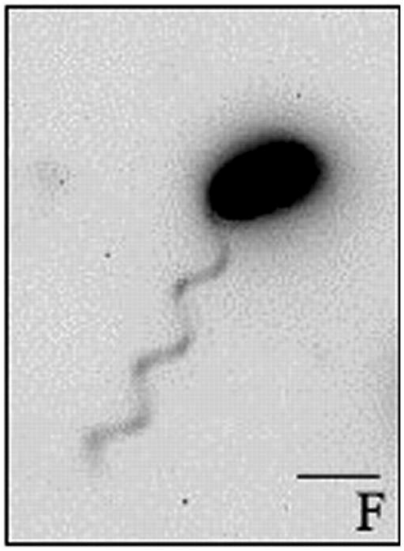

(c)

Fig. 1.1 Microscopic images of several unicellular swimming organisms (a) Oplina is covered by hairlike flagella called cilia that forms the motion. The scale bar is $10\mu m$. Figure republished with permission of Royal Society, from reference [7]; permission conveyed through Copyright Clearance Center, Inc. (b) The Salmonella bacteria swim using several long flagella attached to the surface of the cell. The scale bar is $1\mu m$. Figure republished with permission of Annual Review of Fluid Mechanics, from reference [8]; permission conveyed through Copyright Clearance Center, Inc. (c) Photobacterium profundum consists of a rod shape head and a single flagellum. Scale bar is $2\mu m$. Figure republished with permission from reference [9] ©2008 American Society for Microbiology.

in hydrogen peroxide solution with the anticancerdrug (doxorubicin hydrochloride DOX) loaded in the meso-porous cap. Lipid bilayer covers the carried cap which facilitates a slow drug release within cells.

Janus particles are characterized by inhomogeneous surface features which can form a field gradient. For example a diffusophoretic Janus particle has one cap which catalyzes a chemical reaction in the fluid. This leads to changes in the concentration of chemical components in the vicinity of the cap which brakes the symmetry. As a result of anisotropic environment, unbalanced forces (e.g. osmotic force [41]) generate propulsion. In the case of a thermophoretic Janus particle, a metallic cap absorbs more energy from an external source which can be a heat source (laser beam [10, 42, 43]) or a magnetic field [44]. Energy absorption increases the temperature around that cap, generating a temperature gradient which results in the particle propulsion. Figure 1.3 shows self-propelled particles in a

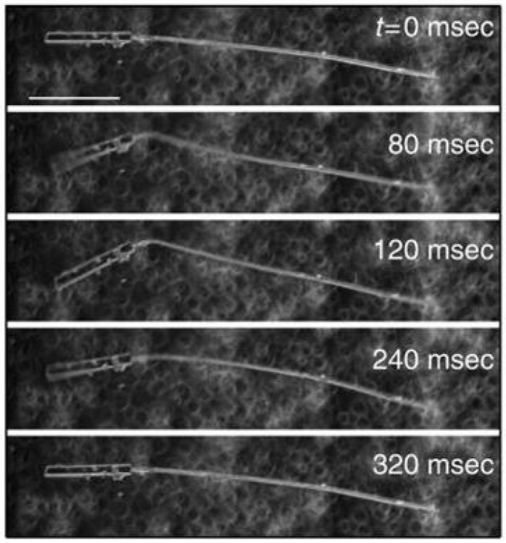

(a)

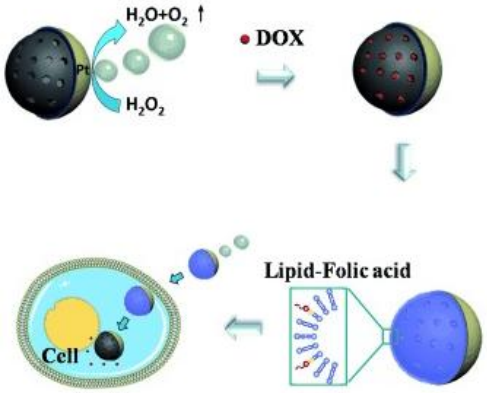

(b)

Fig. 1.2 Examples of artificial microswimmers (a) An artificial sperm. Figure reprinted by permission from Springer Nature Customer Service Centre GmbH: reference [32] ©2014. (b) Diffusiophoresis particle. Figure reprinted by permission from reference [20] ©2014 by John Wiley Sons.

temperature gradient with different mechanisms of propulsion. Asymmetric micrograer is shown in figure 1.3a which with a homogeneous surface rotates by heating its surface, while the average temperature of surrounding fluid is fixed. Figure 1.3b shows a laser-heated Janus particle under a rotating electric field which presents the circular motion. A self-propelled Janus particle suspended in a critical binary liquid mixture with a drop at its surface is shown in figure 5.1. A snapshot of self-assembly of thermophoretic dimers is presented in figure 1.3d.

1.2 Thermophoresis

Temperature gradients lead to several natural phenomena such as convection in presence of external field, and have many applications in technology such as distillation [48], separation and measurement of the concentrations of multicomponent mixtures [49], or thermoelectric generators [50].

The effect of temperature inhomogeneities in a multicomponent mixture can be identified by phase separation (see figure 1.4). If a mixture consists of particles of the same size (e.g. a

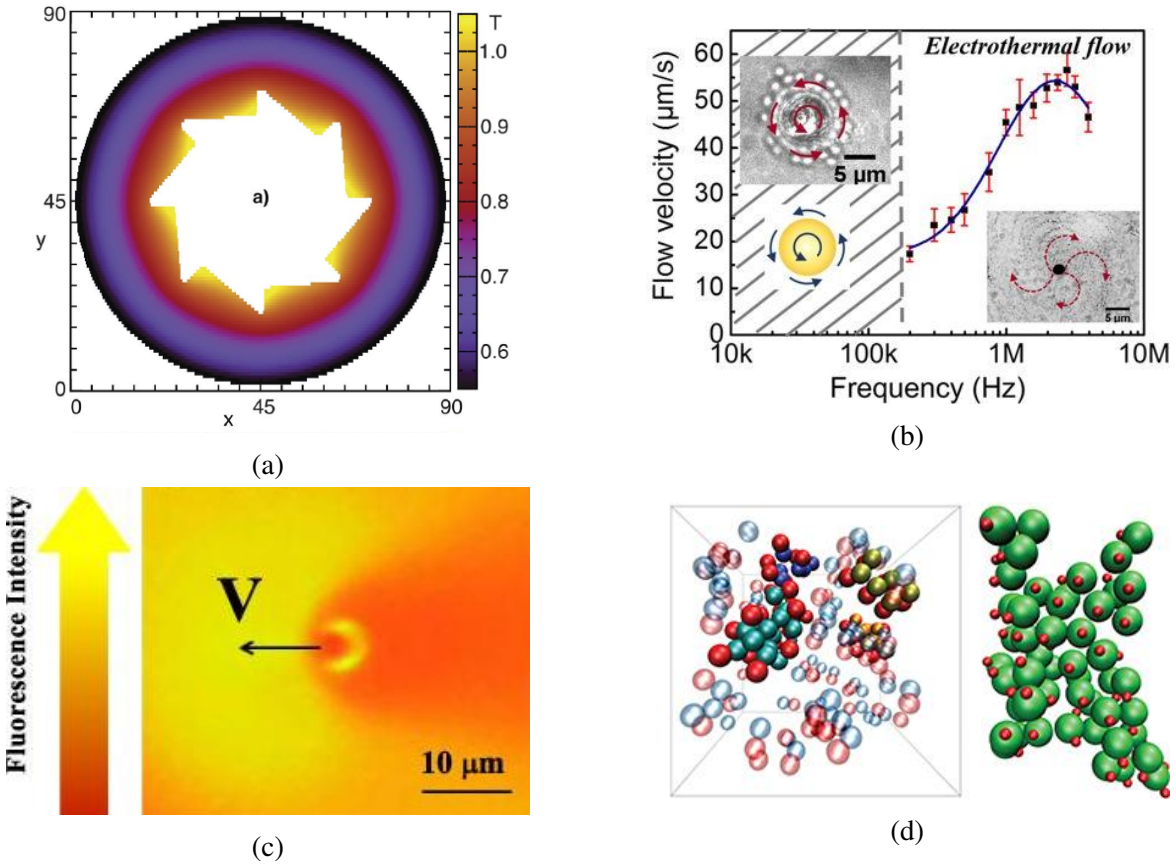

(a) (b) (c) (d)

Fig. 1.3 Examples of thermophoretic microswimmer (a) Asymmetric micrograer (figure from reference [45] reproduced by permission of The Royal Society of Chemistry) (b) Janus particle under a rotating electric field (Figure adopted from reference [46], available under a Creative Commons license.) (c) Janus in a critical binary mixture (figure from reference [42]©IOP Publishing. Reproduced with permission. All rights reserved.) (d) Assembling of thermophoretic dimers. Figure republished with permission of Europhysics letters, from reference [47].

binary mixture) the phenomenon is called thermodiffusion otherwise thermophoresis (e.g. colloid solution). Both can be explained by hydrodynamics theory [51, 52] or non-equilibrium thermodynamics [53, 54]. Some studies suggest that thermodiffusion and thermophoresis are of the same origin [55], while other theoretical works have showed that they are different phenomena [56, 57]. However, in most cases, these thermodiffusion and thermophoresis are used interchangeably. This phenomenon is also called the Soret effect, in honor of Charles Soret who described it in detail [58].

When the temperature gradient is established all species start moving and eventually get separated such that they are assembled in regions either at the highest or lowest temperature.

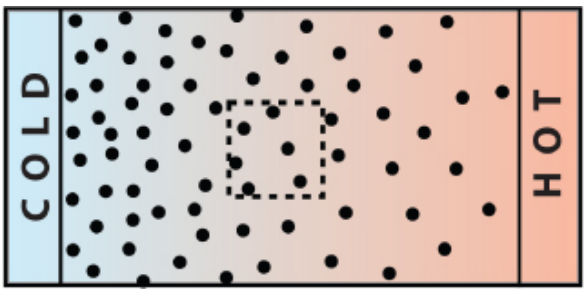

Fig. 1.4 Schematic picture of Soret effect. Figure from reference [59] ©IOP Publishing. Reproduced with permission. All rights reserved.

If suspended particles drift towards the cold side, they are called thermophobic and otherwise thermophilic. Most of the experiments demonstrate thermophobic behavior, but some examples of thermophilic behavior also exist [60].

The motion of thermophoretic particles is achieved by a driving force which is generated by the temperature gradient. In some cases, the temperature gradient facilitates driving directly (Janus particle in simple fluid [61]) while in other cases, other physical mechanisms might be at play (Janus in the critical binary mixture [62]). However, the driving force originates from particle interactions represented by either fluid-fluid interaction or fluid-suspended particle interaction. The interactions determine the direction of motion and its strength and the thermophoretic coefficients. Starting from 1856, experimental works, theoretical studies, and simulations of the Soret effect persist until now for different systems.

1.2.1 Experiments on Thermodiffusion

The first experimental observation of the Soret effect refers to 1856 by Carl Friedrich Wilhelm Ludwig [63] for a sodium sulfate solution in the temperature gradient. He used a U-shaped tube which two ends were cooled in ice water and the middle part was heated up in boiling water. He found salt accumulation at cold parts. After that, Soret between 1879-1884 had observed thermodiffusion in several experiments with NaCl and KNO_3 solutions in straight and U-shaped tubes, where heating and cooling were performed in the water at 78° and $15^\circ - 18^\circ$ respectively. The duration of his experiments was 10 to 25 days. He observed that the salt has assembled at the cold side.

The Soret coefficient S_T is introduced to quantify the separation between components. The sign of coefficient defines whether the solute or suspended particles move toward the cold (positive) or hot (negative) sides and the magnitude characterizes the strength of separation. The positive and negative Soret coefficients S_T correlated to respectively thermophobic and

thermophilic behavior. Different techniques were introduced to measure the Soret coefficient S_T in experiments [64]. Figure 1.5 presents the Soret coefficient S_T measured in (a) aqueous suspensions of polystyrene and (b) the polymer solution in water as a function of temperature. Clearly, the magnitude, sign, and behavior of the Soret coefficient are different for distinct chemical components.

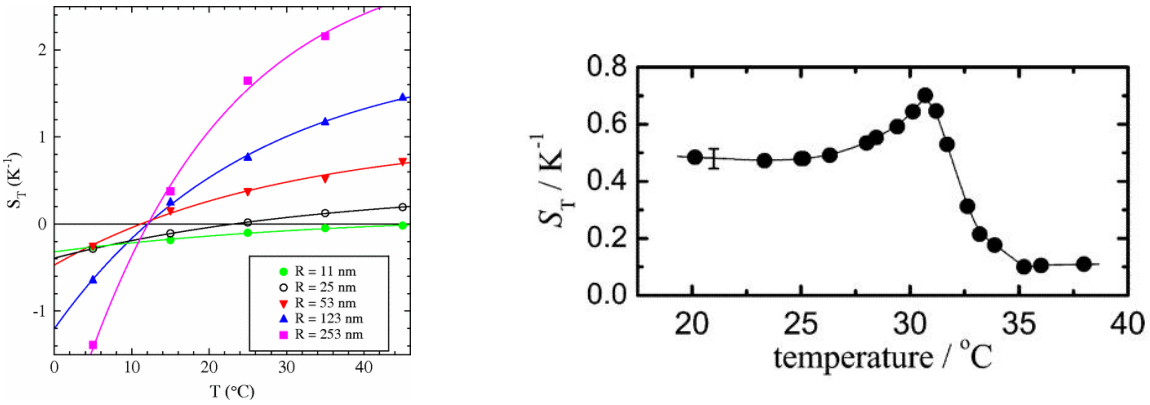

(a) (b)

Fig. 1.5 Temperature dependence of the Soret coefficient for (a) aqueous suspensions of polystyrene with different particle sizes. Reprinted figure with permission from reference [60] Copyright 2018 by the American Physical Society. (b) Poly(N-isopropylacrylamide) (PNiPAM) chain in water. Figure reprinted with permission from reference [65]. Copyright 2005 American Chemical Society.

1.2.2 Theory of Thermodiffusion

The Soret effect was explained theoretically after the first experiments in the 20th century. The phenomenological equation of thermodiffusion expresses the total mass flux using two terms acting against each other. In the steady state, they are equal in the magnitude but opposite in the direction. The first term represents mass flux due to the temperature gradient and the second one is related to the concentration gradient known as the standard Fick's diffusion. Thermodiffision coefficients are related to the coefficients of these two terms.

The kinetic theory, non-equilibrium thermodynamics and their combinations [66] have led to the most famous theories in thermodiffusion. However, most of the models contain variables that are usually obtained from other models and they depend on thermodynamics properties of a mixture. Here, the linear non-equilibrium thermodynamics theory from reference [67] will be discussed.

Thermodiffusion is non-equilibrium and irreversible process. The first law of thermodynamics is valid only locally in non-equilibrium thermodynamics. Expressions for thermophoretic coefficients, heat and mass transports are derived through the rate of entropy production in a small volume for the simplest heterogeneous system, i.e. one-dimensional transport of heat and mass in x direction. The volume element does not move in the laboratory frame and contains enough number of particles for the statistics of thermodynamic properties. The entropy production is given by:

$$\partial_t S = -\partial_x J_s + \Sigma \tag{1.1}$$

where S is the entropy density, $\partial_x J_s = \partial J_s / \partial x$, J_s is the entropy flux in or out of the volume element, and Σ is the entropy production in this volume. According to the first law of thermodynamics in local equilibrium for a constant volume element, $\mathrm{d}\Upsilon = T\mathrm{d}S + \sum_k \mu_k \mathrm{d}\varphi_k$, where Υ is internal energy, μ_k is chemical potential of component k, $\mathrm{d}\varphi_k$ is the infinitesimal change of number fraction φ_k as particles are added to or subtracted from the volume. Therefore, the rate of entropy production $\partial_t S$ becomes:

$$\partial_t S = \frac{1}{T}\left(\partial_t \Upsilon - \sum_k \mu_k \partial_t \varphi_k\right) \tag{1.2}$$

Equation (1.2) for the surface element turns into:

$$J_s = \frac{1}{T}\left(J_q - \sum_k \mu_k J_k\right) \tag{1.3}$$

where J_q is the total heat flux which in the chemical balance is $\partial_t \Upsilon = -\partial_x J_q$. The total heat flux is given by $J_q = J'_q + \sum_k H_k J_k$ where J'_q is the measurable heat flux, J_k is the flux of particles of type k and H_k is partial molar enthalpy. The flux of particles J_k with the assumption that particles are not produced during the chemical reaction is given by $\partial_x J_k = -\partial_t \varphi_k$. Gibbs energy is calculated through the chemical energy $G = \sum_k \mu_k \varphi_k$. Besides the differential of Gibbs energy usually is given by $\mathrm{d}G = -S\mathrm{d}T + V\mathrm{d}P + \sum_k \mathrm{d}\mu_k \varphi_k$. Comparison between the two definitions of G results in $\sum_k \varphi_k \mathrm{d}\mu_k = -S\mathrm{d}T + V\mathrm{d}P$. Then, we can define:

$$\mathrm{d}\mu_{k,T} = \mathrm{d}\mu_k + S_k \mathrm{d}T, \tag{1.4}$$

where $\mathrm{d}\mu_{k,T} = V_k \mathrm{d}P + \sum_j \left(\partial_{\varphi_j} \mu_k\right)_{T,P,\varphi_l} \mathrm{d}\varphi_j$, and S_k and V_k are the partial molar entropy and partial molar volume, respectively, which are given by $S_k = \left(\dfrac{\partial \mu_k}{\partial T}\right)_{p,\varphi_k}$ and $V_k =$

$\left(\frac{\partial \mu_k}{\partial P}\right)_{T,\varphi_k}$. Furthermore, partial molar enthalpy H_k is related to the chemical potential as $\mathrm{d}\mu_{k,T} = \mathrm{d}H_k - T\mathrm{d}S_k$. Substituting equations (1.3) and (1.4) on to the equation of entropy production (1.1) leads to:

$$\Sigma = \frac{-1}{T^2} J'_q \partial_x T - \sum_k J_k \frac{1}{T} \partial_x \mu_{k,T}. \tag{1.5}$$

In linear non-equilibrium thermodynamics, fluxes J_i (temperature flux J'_q and chemical potential fluxes J_k) are assumed to be linear functions of forces X_i:

$$J_i = \sum_j L_{ij} X_j. \tag{1.6}$$

According to the Onsager relation, $L_{ij} = L_{ji}$. In non-equilibrium thermodynamics, the second law is reformulated as:

$$\Sigma = \sum_i J_i X_i. \tag{1.7}$$

Then the comparison of equations (1.5) and (1.7) results in:

$$\begin{cases} X_q = -\dfrac{1}{T^2} \partial_x T \\ X_m = -\dfrac{1}{T} \sum_k \partial_x \mu_{k,T} \end{cases} \tag{1.8}$$

For a two-component system, $J^1_m = -J^2_m = J_m$ (for details see chapter 3 of [68]) and therefore:

$$X_m = \frac{-1}{T} \partial_x (\mu_{2,T} - \mu_{1,T}) \tag{1.9}$$

Differential of the chemical potential at a constant temperature $\mathrm{d}\mu_{k,T}$ with the Gibbs–Duhem equation can be rewritten as follows:

$$\sum_{k=1}^{2} \varphi_i \mathrm{d}\mu_{k,T} = 0 \Rightarrow \mathrm{d}\mu_{2,T} = -\frac{\varphi_1}{\varphi_2} \mathrm{d}\mu_{1,T} \tag{1.10}$$

Partial derivative relates chemical potential to particle fraction $\partial_x \mu_{k,T} = \partial_{\varphi_k} \mu_{k,T} \partial_x \varphi_k$ and for a two-component system $\varphi_2 = 1 - \varphi_1$ leading to:

$$\partial_x (\mu_{2,T} - \mu_{1,T}) = \frac{\partial_{c1} \mu_{1,T}}{1 - \varphi_1} \partial_x \varphi_1 \tag{1.11}$$

and the fluxes are given by:

$$\begin{cases} J_q = L_{qq}\dfrac{-1}{T^2}\partial_x T + L_{qm}\dfrac{-1}{T}\dfrac{\partial_{c1}\mu_{1,T}}{1-\varphi_1}\partial_x\varphi_1 \\ \\ J_m = L_{qm}\dfrac{-1}{T^2}\partial_x T + L_{mm}\dfrac{-1}{T}\dfrac{\partial_{c1}\mu_{1,T}}{1-\varphi_1}\partial_x\varphi_1 \end{cases} \tag{1.12}$$

The interdiffusion coefficient D_m and thermal diffusion coefficient D_T are defined through the mass flux as:

$$\begin{cases} D_m = -\left[\dfrac{J_m}{\partial_x\varphi_1}\right]_{T=const.} & = \dfrac{L_{mm}}{T}\dfrac{\partial_{\varphi_1}\mu_{1,T}}{1-\varphi_1} \\ \\ D_T = -\left[\dfrac{J_m}{\varphi_1(1-\varphi_1)\partial_x T}\right]_{\varphi_1=const.} & = \dfrac{L_{qm}}{\varphi_1(1-\varphi_1)T^2} \end{cases} \tag{1.13}$$

The mass flux then becomes:

$$J_m = -D_m\partial_x\varphi_1 - D_T\varphi_1(1-\varphi_1)\partial_x T \tag{1.14}$$

The Soret coefficient in the stationary state $J_m = 0$ is defined as:

$$S_T = \frac{D_T}{D_m} = -\frac{1}{\varphi_1(1-\varphi_1)}\frac{\partial_x\varphi_1}{\partial_x T} \tag{1.15}$$

According to equation (1.15), the Soret coefficient can be measured by the ratio of the concentration gradient and temperature gradient. The Soret coefficient has been defined positive if the concentration gradient and temperature gradient are pointing to different directions. The Soret coefficient (or in other words thermophoresis) in liquids is stronger than in gases since interactions in liquids are stronger. Nevertheless, thermophoresis is also used to separate isotopes of gas because they have different masses [67].

1.2.3 Simulations

There are many theoretical approaches to describe non-equilibrium thermodynamics. In the absence of a comprehensive theoretical model, simulation approaches are useful tools. Simulations allow us to determine the thermal diffusion coefficients directly. With the development of appropriate computational methods, simulations of thermophoretic effects have attracted more and more attention. One of the first thermophoretic simulations was done by

MacGowan and Evans in 1986 [69] for a binary mixture using non-equilibrium molecular dynamics (NEMD) (NEMD)[70]. They evaluated heat and mass transport coefficients for an equimolar argon-krypton mixture, modeled by Lennard-Jones 12-6 interactions.

However, more sophisticated systems such as a Janus particle in a binary mixture are still difficult to simulate. The difficulties include working with large particles, long integration times and more complicated interactions between solvent molecules and either colloid surface or solvent. Multi-particle collision dynamics and Lattice Boltzmann methods are coarse-grained simulation techniques used successfully in some thermophoretic studies [71, 72, 45, 73]. Dissipative particle dynamics is another well known coarse-grained technique which can be used to advance over understanding of thermophoresis [74].

1.2.4 Applications of Thermophoresis

Thermophoresis is important in many natural phenomena such as convection [75], isotope separation in Lava [76] or even in the origin of life. The idea is that the thermal gradient between warm volcanic rocks and cold ocean water during the early stages of Earth might have contributed to the creation of essential molecules of life [77]).

In addition to the importance of thermophoresis in natural processes, it is also often used in industry. The Soret effect depends strongly on the properties of molecular mixture including particle size, interaction between particles, charge, conformation and etc. (see figure 1.5). Therefore, thermophoresis is employed as a separation technique based on component properties for various systems such as chemical solutions [78], suspension of polymers, protein solutions, etc. [79].

As a consequence, microscale thermophoresis (MST) technology has been developed to analyze biomolecular interactions using fluorescent molecules observed on microscopic temperature gradients [80]. The procedure of MST is illustrated in figure 1.6. Typical MST process consists of four parts: (a) A laser is focused at a point in the center of the picture. Suspended particles move outwards after turning on the laser. Then, the laser is switched off and the particles again are distributed uniformly, (b) In this method, interactions are analyzed by the intensity of florescence. Some of the particles are fluorescently labeled. For example, for the hybridization of DNA, particles are labeled as illustrated in this figure, (c) The temperature gradient and movement of fluorescent molecules lead to a change in the intensity of fluorescence. By switching on the laser, the intensity decreases. Part of the molecules that are labeled with florescence (black trace, unbound) show different intensity

changes in comparison to the non-labeled ones (red trace, bound). For analysis, the change in thermophoresis is expressed as the change in the normalized fluorescence F_{norm}, which is defined as F_{hot}/F_{cold}. F-values correspond to average fluorescence values between defined areas marked by the red and blue cursors, respectively, (d) The binding constant of the under investigation biological molecule is obtained by fitting the gradual change of ΔF_{norm} with a function of thermophoretic depletion of non-fluorescent ligands in a titration process.

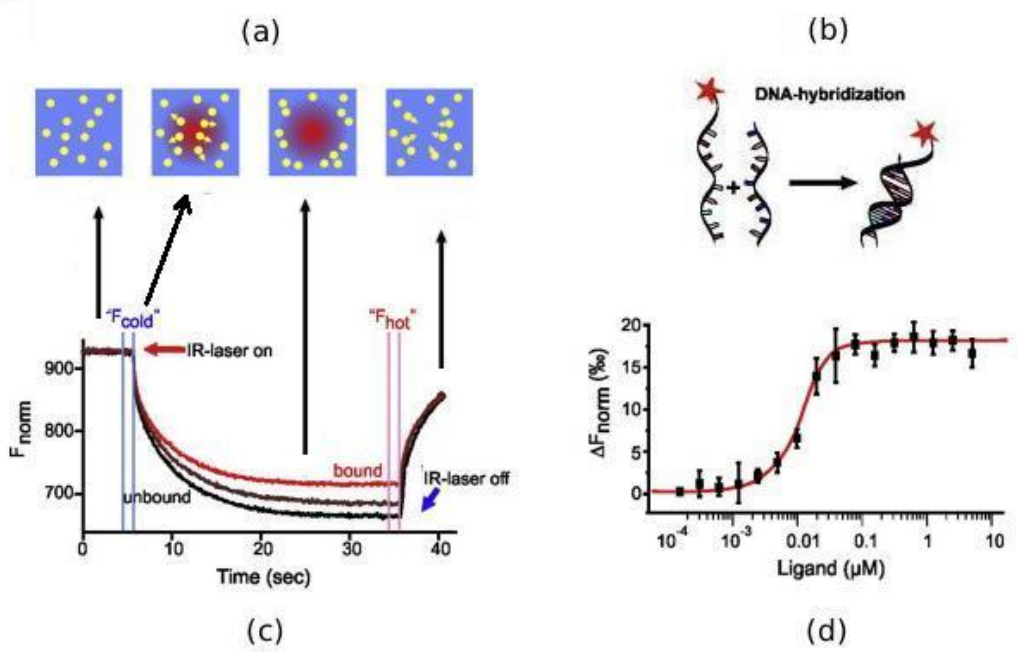

Fig. 1.6 Typical MST process: (a) A laser is focused at a point in the center of the picture. Suspended particles move outwards after turning on the laser. Then, the laser is switched off and the particles again are distributed uniformly. (b) Labeling particle with fluorescent (c) The temperature gradient and movement of fluorescent molecules lead to a change in the intensity of fluorescence. (d) The binding constant of the under investigation biological molecule is obtained by fitting the gradual change of ΔF_{norm} with a function of thermophoretic depletion of non-fluorescent ligands in a titration process. Figure reprinted from reference [80], available under a Creative Commons license.

1.3 Hydrodynamics

The size of colloids ranges from 1nm to 1μm, while the size of fluid molecules is a few angstroms. Therefore, a colloid suspended in fluid feels a continuous environment which can be described by Navier-Stokes equations. They are derived from the Newton's second law and basic conservation laws, such as mass and momentum conservation.

The mass conservation principle applied to the continuous fluid expresses the rate of mass variation in a specific fluid volume element where a balance between the rate of mass flow into the volume and the flow out of it is considered. Let us assume a cubic volume element in a fluid at the position x, y, z with side lengths $\delta x, \delta y$ and δz which moves with a certain velocity $\mathbf{v} = \mathbf{v}(x, y, z, t)$. The rate of mass flow passing through one side is $(\rho \mathbf{v})_{x_i}$ and from the opposite side is $(\rho \mathbf{v})_{x_i+\delta x_i}$, where $\rho = \rho(x, y, z, t)$ is the fluid density. Therefore, the mass conservation law:

$$\partial \rho + \nabla \cdot (\rho \mathbf{v}) = s_m \tag{1.16}$$

The equation (1.16) is called the continuity equation and can be applied to other conserved physical quantities by substituting the fluid density ρ with any other conserved physical quantity ϕ.

The Newton's second law for the fluid volume element is represented by:

$$\begin{aligned} \mathbf{F} &= \rho \frac{\mathrm{d}\mathbf{v}(x, y, z, t)}{\mathrm{d}t} \delta x \delta y \delta z \\ &= \rho \left(\partial_t \mathbf{v} + \partial_x \mathbf{v} \partial_t x + \partial_y \mathbf{v} \partial_t y + \partial_z \mathbf{v} \partial_t z \right) \delta x \delta y \delta z \\ &= \rho \left(\partial_t \mathbf{v} + (\mathbf{v} \cdot \nabla) \mathbf{v} \right) \delta x \delta y \delta z \end{aligned} \tag{1.17}$$

where $\mathbf{F}$ is the force acting on the volume element of fluid. This force consists of two parts: the total external force $\mathbf{f}_{ext}$ and a net surface force $\mathbf{f}_{sur}$ which appears due to fluid stresses. The surface force arises from two parts: pressure and shear stress. In x direction, the total force applied to the fluid due to pressure is $(P_x - P_{x+\delta x}) \delta y \delta z$, and due to shear stress $\left((\tau_{xy})_y - (\tau_{xy})_{y+\delta y} \right) \delta x \delta y + \left((\tau_{xz})_z - (\tau_{xz})_{z+\delta z} \right) \delta x \delta z$. By substituting these relations into all directions to equation (1.17) and dividing by the volume element while differential lengths approach zero, we obtain:

$$\rho \left(\partial_t \mathbf{v} + \mathbf{v} \cdot \nabla \mathbf{v} \right) = \mathbf{f}_{ext} - \nabla P + \nabla \cdot \tau \tag{1.18}$$

Furthermore, for a Newtonian fluid (the viscosity is constant), the stress is given by $\tau = \eta \nabla \mathbf{u}$ where η is the dynamic viscosity and it is a tensor that is independent of the velocity or stress state. Stokes added three assumptions to equation (1.18): (*i*) the stress tensor is a linear function of the strain rate tensor $\dot{\gamma}$, (*ii*), the fluid is isotropic which means that η is a scaler and (*iii*) the fluid at rest satisfies $\nabla.\tau = 0$.

The strain rate tensor $\dot{\gamma}$ is the rate of change of deformation of volume element over time. In order to find an expression for the strain rate, the face of volume element in $x-y$ plane has to be considered as it deforms with time δt. The rate of shear strain is $\dot{\gamma}_{xy} = \dot{\theta}_x + \dot{\theta}_y$, and it can be shown that:

$$\dot{\gamma}_{xy} = \partial_x v_y + \partial_y v_x \tag{1.19}$$

Considering equation (1.19) with the Stokes assumptions results in the relationship between stress and velocity as:

$$\tau_{ij} = \eta \left(\frac{\partial v_i}{\partial x_j} + \frac{\partial v_j}{\partial x_i} \right) + \delta_{ij} \lambda \frac{\partial v_k}{\partial x_k} \tag{1.20}$$

where δ_{ij} is the Kronecker delta defined as $\delta_{ij} = 1$ if $i = j$, and zero otherwise and λ is the second coefficient of viscosity or bulk viscosity. Equations 1.18 and 1.20 result in the final expression for the second law of Newton in fluid, which is known as a momentum equation of Navier-Stokes equations:

$$\rho \frac{\mathrm{D}\mathbf{v}}{\mathrm{D}t} = \mathbf{f}_{ext} - \nabla P + \eta \nabla^2 \mathbf{v} + (\lambda + \eta) \nabla (\nabla \cdot \mathbf{v}) \tag{1.21}$$

Incompressible fluid refers to a liquid material whoose density is constant within a fluid element. This condition together with the continuity equation (1.16) lead to:

$$\nabla.\mathbf{v} = 0 \tag{1.22}$$

Therefore, the last term in equation (1.21) is eliminated and:

$$\rho \frac{\mathrm{D}\mathbf{v}}{\mathrm{D}t} = \mathbf{f}_{ext} - \nabla P + \eta \nabla^2 \mathbf{v} \tag{1.23}$$

This equation can be simplified further for different flow regimes using the famous dimensionless number in flow dynamics known as the Reynolds number. The Reynolds number characterizes the flow with the description of the degree of laminar or turbulent flow

Swimmer	Reynolds number	size order(m)
Blue whale	4×10^8	10
Person	4×10^6	1
Colloid particle	10^{-4}	$10^{-9} - 10^{-6}$
Bacteria /cells	10^{-5}	$10^{-3} - 10^{-6}$

Table 1.1 Reynolds number of several swimmers in water. From "https://en.wikipedia.org/wiki/Reynolds_number"

and it is measured by the ratio of inertial forces ρvL to viscous forces η in fluid flow:

$$Re = \frac{\rho vL}{\eta} = \frac{\rho v}{\nu} \tag{1.24}$$

where L is a characteristic length and ν is the kinematic viscosity. Table 1.1 presents Reynolds numbers for several swimmers with different sizes in water. We will focus on colloidal systems. In such systems Reynolds number is small and in the steady state, equation (1.23) reduces to the Stokes equation:

$$\mathbf{f}_{ext} - \nabla P + \eta \nabla^2 \mathbf{v} = 0 \tag{1.25}$$

The Stokes equations (equations 1.22 and 1.25) are simplified versions of the Navier–Stokes equations for the case at zero Reynolds number. In an infinite system, the solution of these equations for a circle in moving in a plane or the flow around the very long cylinder does not exist, which is known as Stokes paradox [81].

1.4 Outline of the thesis

In this thesis, we study a Janus particle in temperature gradient condition with various environment. In this regard, in chapter 2, we introduce a stable integration scheme for simulation of mesoscopic fluid with mass, momentum, and heat transport phenomena with the powerful simulation technique known as dissipative particle dynamics. In chapter 3, this algorithm is verified first in the simulation of fluid in constant temperature with thermodynamical properties such as the energy of the system, radial distribution function and temperature and then with constancy check in a fluid under the temperature gradient. In chapter 4, a heated Janus particle in the simple fluid is investigated and the effect of model parameters and interactions between Janus and fluid on a motion of the Janus particle has been elucidated. Modeling a binary mixture with dissipative particle dynamics and some

important factors such as critical point, surface tension and contact angle in the coexisting of different phases are explored in chapter 5. In chapter 6 we return to the thermophoresis phenomena and a Janus in a binary mixture is simulated for the first time.

Chapter 2

Simulation Methods

In this chapter, first principles of simulation are explained. Then, several simulation methods with energy conservation to model thermal processes are introduced. The final parts of this chapter are techniques to implement the thermal gradient.

2.1 Molecular Dynamics and Mesoscopic Simulation

One of the traditional simulation methods is Molecular dynamics simulation (MD), which is used to simulate classical many body system. The word classical corresponds here to motion of particles which obeys the rules of classical mechanics. Each particle in MD simulation represents one atom or molecule. MD can model a fluid with N particles where each particle with an index i is identified by its mass m_i, position $\mathbf{r}_i$, and velocity $\mathbf{v}_i$. The idea of MD simulation is to solve Newton's equations of motion:

$$\frac{\mathrm{d}\mathbf{r}_i}{\mathrm{d}t} = \mathbf{v}_i, \tag{2.1}$$

$$\frac{\mathrm{d}\mathbf{v}_i}{\mathrm{d}t} = \frac{1}{m}\mathbf{F}_i \tag{2.2}$$

where $\mathbf{F}_i$ is the total force on particle i. Typically, interactions between particles are pairwise and all particles can contribute to the total force on particle i:

$$\mathbf{F}_i = \sum_{j \neq i} \mathbf{F}_{ij} = \sum_{j \neq i} -\frac{\partial U}{\partial r_{ij}} \frac{\mathbf{r}_{ij}}{r_{ij}} \tag{2.3}$$

where U is the potential energy associated with the force. In principle, the range of potential is unlimited such that a huge number of interactions would need to be considered, i.e. in a system with N particles, the number of pairs is $N \times (N-1)/2$. Thus, a system with a N

particles requires simulation time proportional to N^2. Nevertheless, since most potentials can be neglected at large distances, it is common to truncate the force beyond a distance of r_c which is known as the cut-off radius. This trick significantly decreases the calculation cost for inter-particle forces.

The simplest approach to integrate equations (2.1) and (2.2) is called Euler algorithm and is based on the Taylor expansion of equation (2.1):

$$\mathbf{r}_i(t+\Delta t) = \mathbf{r}_i(t) + \mathbf{v}_i(t)\Delta t + \frac{1}{2}\frac{\mathbf{F}_i(t)}{m_i}\Delta t^2 + \mathscr{O}(\Delta t^3) \tag{2.4}$$

$$\mathbf{v}_i(t+\Delta t) = \mathbf{v}_i(t) + \frac{\mathbf{F}_i(t)}{m_i}\Delta t + \mathscr{O}(\Delta t^2) \tag{2.5}$$

where Δt is timestep. If the timestep is small enough, high order terms $\mathscr{O}(\Delta t^2)$ in the equations (2.4) and (2.5) can be neglected and the Euler algorithm is obtained:

$$\mathbf{r}_i(t+\Delta t) = \mathbf{r}_i(t) + \mathbf{v}_i(t)\Delta t$$
$$\mathbf{v}_i(t+\Delta t) = \mathbf{v}_i(t) + \frac{\mathbf{F}_i(t)}{m_i}\Delta t$$

This simple approach has stability problems. An alternative is the Verlet algorithm. In the Verlet algorithm, equations (2.4) and (2.5) are rewritten as follows with negligible terms of terms $\mathscr{O}(\Delta t^3)$ and higher:

$$\mathbf{r}_i(t+\Delta t) = 2\mathbf{r}_i(t) - \mathbf{r}_i(t-\Delta t) + \frac{1}{2}\frac{\mathbf{F}_i(t)}{m_i}\Delta t^2 \tag{2.6}$$

$$\mathbf{v}_i(t+\Delta t) = \frac{\mathbf{r}_i(t+\Delta t) - \mathbf{r}_i(t-\Delta t)}{2\Delta t} \tag{2.7}$$

In order to optimize the memory usage, the velocity Verlet algorithm can be rearanged to integrate velocities and positions at the same time in a way that errors do not become larger. Position updates are done similar to equation (2.6) and velocity is updated as follows:

$$\mathbf{v}_i(t+\Delta t) = \mathbf{v}_i(t) + \frac{\mathbf{F}_i(t) + \mathbf{F}_i(t+\Delta t)}{2m_i}\Delta t \tag{2.8}$$

Note that, instead of assigning excessive memory to keep track of the forces at every timestep, the integration scheme can be divided into two parts for particle i. First part is:

- $\mathbf{v}_i(t+\frac{1}{2}\Delta t) = \mathbf{v}_i(t) + \frac{\mathbf{F}_i(t)}{2m}\Delta t$

- $\mathbf{r}_i(t+\Delta t) = \mathbf{r}_i(t) + \mathbf{v}_i(t+\frac{1}{2}\Delta t)\Delta t$

Then the forces based on new positions are calculated and the velocity is updated as:

- $\mathbf{v}_i(t+\Delta t) = \mathbf{v}_i(t+\frac{1}{2}\Delta t) + \frac{\mathbf{F}_i(t+\Delta t)}{2m}\Delta t$

Positions and velocities of particles are initialized at the beginning of a simulation. Positions are chosen such that the configuration is close to the final expectation and inappropriate overlaps between particles are excluded. Commonly, velocities are initialized from Maxwell-Boltzmann distribution such that the average velocity is zero and the average kinetic energy corresponds to a desired temperature. After a while (relaxation time), the average properties of the system do not change with time anymore and system remains in a steady state. After that, the quantities of interest can be measured.

Based on choices (e.g. potential) for a MD simulation, time and length scales are in the range of 10^{-13} to 10^{-9} seconds and 10^{-13} to 10^{-7} meters respectively [82]. Such small time and length scales make MD unsuitable for a simulation of systems which require long times or a very large number of particles like colloids and polymers. Even with supercomputers, simulation of folding processes (a polypeptide folds into a specific three dimensional structure [83]) of only small and relatively fast folding proteins are currently possible with MD.

In order to access large system sizes and long time scales, coarse-grained models are proposed. In such models, several fluid particles can be represented by one particle and then new interactions between the large or coarse-grained particles are introduced based on some coarse-graining procedure. Mesoscale simulation methods (e.g. Lattice Boltzmann, Multi-particle collision dynamics, and Dissipative particle dynamics) can describe complex fluids at larger length and timescales since they presents coarse-grained systems. These models bridge the gap between microscopic (MD simulation) and macroscopic (continuum regimes [84]) scales. This intermediate range is called mesoscopic scale.

Fluid simulations with Lattice Boltzmann (LB) method solve discrete Boltzmann equations [85, 86]. As the name indicates, this model is based on a lattice scheme. In fact, space is discretized such that particles move between lattice points. LBM simulation consists of two steps: collision and propagation. In the collision step, the number of particles is conserved at each cell, but velocities of particles change. In the propagation step, at least one particle moves from one point of the lattice to a neighboring point. Mass and momentum are conserved in this method [87].

Multi-particle collision dynamics (MPC), whose original version is known as stochastic rotation dynamics (SRD), has been proposed by Malevanets and Kapral [88, 89]. MPC system consists of alternating streaming and collision steps. In the streaming step, positions of particles are updated using their velocities (ballistic motion). In the collision step, the simulation system is divided into cells and interactions between particles inside each cell are modeled, such that velocities of particles within each cell are updated as:

$$\mathbf{v}_i(t+\Delta t) = \mathbf{v}_{cm}(t) + Rot(\theta)\left(\mathbf{v}_i(t) - \mathbf{v}_{cm}(t)\right) \tag{2.9}$$

where $\mathbf{v}_{cm}$ is the center of mass velocity of particles in a cell and $Rot(\theta)$ is rotational matrix having a random rotation axis and a rotating angle θ. Mass, momentum, and energy are conserved locally which makes MPC very useful technique. Nevertheless, MPC fluid represents an ideal gas, which is quite compressible and modeling some physical systems such as a binary mixture is not very straightforward.

Dissipative particle dynamics (DPD) was introduced by Hoogerbrugge and Koelman [90, 91]. Similar to MD, in the DPD method, each point particle is characterized by a position and velocity which are updated every timestep through velocities and forces, respectively. The interaction between particles consists of a conservative force F^C, a dissipative force F^D and a random force F^R. All interactions in DPD are pairwise interactions, providing momentum conservation. This fact allows the system to exhibit correct hydrodynamics behavior from a mesoscopic point of view. The temperature of a system is controlled by dissipative and random forces such that their combination acts as a thermostat in DPD system. In other words, dissipative force cools down, while random force heats up the system. Because of the use of thermostat, energy is not conserved in the standard DPD method, thus it models isothermal systems. DPD was successfully employed for simulations of various systems such as simple or complex fluids [92–95], polymers [96, 97], colloidal suspensions [98, 99], self-assembly of lipids [100], and biological membranes [101].

Each DPD particle can be interpreted as a cluster of molecules or atoms. Therefore, DPD particles can be considered to have large and soft ranges, such that they can even overlap with each other. These features of DPD particles are illustrated in figure 2.1.

Fluid in the DPD method is simulated by N particles which interact in the range of the cut-off radius r_c:

$$\mathbf{F}_i = \sum_{j \neq i} \left(\mathbf{F}_{ij}^C + \mathbf{F}_{ij}^D + \mathbf{F}_{ij}^R \right) \tag{2.10}$$

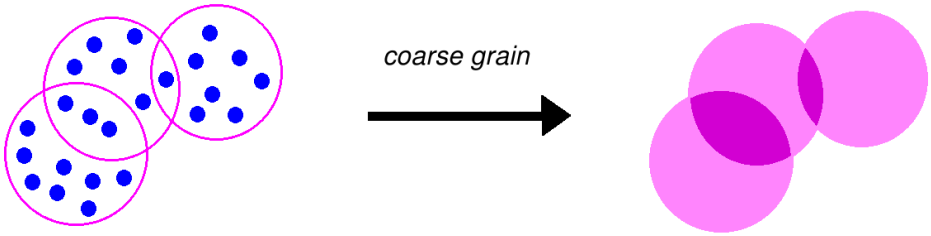

Fig. 2.1 One DPD particle represents several atoms or molecules.

The conservative force $\mathbf{F}^C$ is generally chosen as a soft interaction [102–107], allowing a large timestep:

$$\mathbf{F}_{ij}^C = a_{ij}\omega^C(r_{ij})\hat{\mathbf{r}}_{ij} \tag{2.11}$$

where $\hat{\mathbf{r}}_{ij}$ is a unit vector in a direction of $\mathbf{r}_{ij}$, $\mathbf{r}_{ij}$ is relative position and $\omega^C(r_{ij})$ is a weight function of conservative force commonly given by:

$$\omega^C(r_{ij}) = \begin{cases} 1 - \dfrac{r_{ij}}{r_c} & r_{ij} \leq r_c \\ 0 & r_{ij} > r_c \end{cases} \tag{2.12}$$

The coefficient of conservative force a_{ij} controls fluid compressibility. Compressibility of a fluid β is defined as [102]:

$$\beta^{-1} = \frac{1}{k_B T}\left(\frac{\partial P}{\partial n}\right)_T \tag{2.13}$$

where T is the average temperature of the system, k_B is Boltzmann constant, P is pressure and n is number density. Pressure is obtained by the virial theorem:

$$\begin{aligned} P &= \rho k_B T + \frac{1}{3V}\langle \sum_{j>i} \left(\mathbf{r}_i - \mathbf{r}_j\right) \cdot \mathbf{F}_{ij}^C \rangle \\ &= \rho k_B T + \frac{2\pi}{3}\rho^2 \int_0^1 r f(r) g(r) r^2 \mathrm{d}r \end{aligned} \tag{2.14}$$

where $g(r)$ is the radial distribution function. If we assume that $g(r)$ is equal to 1, we obtain that $\left(P - \rho k_B T\right)/a_{ij}\rho^2$ for $\rho > 2$ is a constant function of density [102]. Therefore:

$$P = \rho k_B T + \alpha_0 a_{ij} \rho^2 \qquad \text{with: } \alpha_0 = 0.101 \pm 0.001 \tag{2.15}$$

plugging equation (2.15) into equation (2.13) gives the compressibility:

$$\beta^{-1} = 1 + \frac{2\alpha_0 a_{ij}\rho}{k_B T} \tag{2.16}$$

The dissipative force $\mathbf{F}^D$ is related to friction and accounts for how the forces depend on relative velocity and position based on Galilean invariance. It is defined as follows:

$$\mathbf{F}^D_{ij} = -\gamma_{ij}\omega^D(r_{ij})(\mathbf{v}_{ij}.\hat{\mathbf{r}}_{ij})\hat{\mathbf{r}}_{ij} \tag{2.17}$$

where $\mathbf{v}_{ij} = \mathbf{v}_i - \mathbf{v}_j$ is the relative velocity, γ_{ij} is the friction amplitude between particles and $\omega^D(r_{ij})$ is a weight function. The friction is related to the viscous interaction and is implemented by $\mathbf{v}_{ij}.\hat{\mathbf{r}}_{ij}$ (if two particles approach (go apart), this term is negative (positive) and they feel a force which slows them down.). A standard choice for weight function is:

$$\omega^D(r_{ij}) = \begin{cases} \left(1 - \dfrac{r_{ij}}{r_c}\right)^{2s} & r_{ij} \leq r_c \\ 0 & r_{ij} > r_c \end{cases} \tag{2.18}$$

where s is the exponent of the weight function that affects the dynamic properties of the system such as the fluid viscosity, since the particle interactions can be stronger or weaker within the same range (see figure 2.2). In the original DPD algorithm, $s = 1.0$ [108].

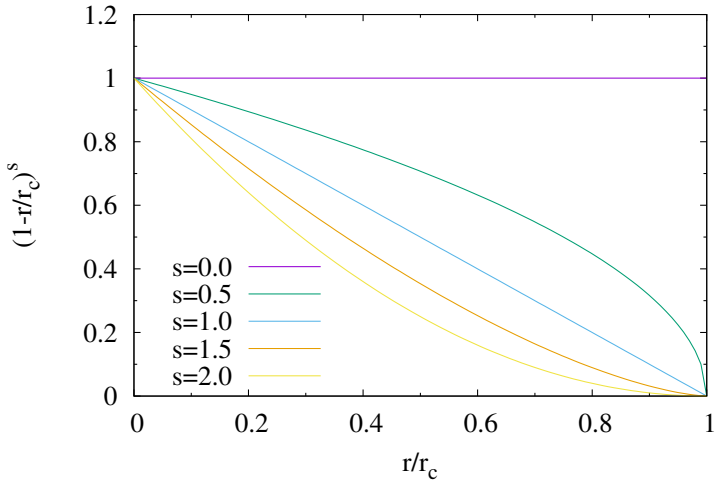

Fig. 2.2 Weight functions for various values of the exponent s.

Random force $\mathbf{F}^R$ is a consequence of Brownian motion and is implemented as a Wiener process:

$$\mathbf{F}^R_{ij} = \sigma_{ij}\omega^R(r_{ij})\xi_{ij}\Delta t^{-1/2}\hat{\mathbf{r}}_{ij} \tag{2.19}$$

where ξ_{ij} is the Gaussian white noise function with zero mean and unit variance. It is symmetric, such that $\xi_{ij} = \xi_{ji}$ and as a consequence: $\mathbf{F}^R_{ij} = -\mathbf{F}^R_{ji}$, so that the momentum is locally conserved. On average the random force is zero and the variance is not a function of the timestep Δt if $\mathbf{F}^R \propto \Delta t^{-1/2}$ [102]. The noise amplitude σ_{ij} is connected to the friction amplitude through the fluctuation-dissipation balance [92]:

$$\sigma^2_{ij} = 2\gamma_{ij}k_B, \omega^R = \sqrt{\omega^D} \tag{2.20}$$

In the standard DPD, σ_{ij} and γ_{ij} are considered to be constants such that for all particles $\sigma_{ij} = \sigma$ and $\gamma_{ij} = \gamma$.

2.2 Energy Conserving Method

For studies of thermal processes in complex fluids, energy conservation is necessary. The micro-canonical ensemble of a thermal system is used in different simulation methods. Some examples of simulations of physical systems include heat transfer, alloying [109], binary mixtures [110], and thermophoretic phenomena [10, 74]. Heat transfer has a wide application in the engineering area starting different kinds of reactors to nano and micro-machines [111, 112].

In fluid simulations with the Lattice Boltzmann (LB) method, energy conservation can be implemented in several different ways [113, 114], such that LB simulations can describe different thermal systems successfully [115–117]. MPC method conserves energy locally in its basic implementation which has been used to describe e.g. thermophoretic phenomena [47, 118, 119]. Classical DPD does not conserve energy, because forces are velocity dependent. This problem has been solved by Español [120] and Avalos and Mackie [121] who derived dissipative particle dynamics with energy conservation DPDe which is discussed in the following section.

2.2.1 Dissipative Particle Dynamics with Energy Conservation

DPDe has been used to simulate problems with thermal gradients such as natural [122] and forced convection [123], temperature dependent properties of fluids [124] and thermophoretic Janus colloids [74].

In order to add energy conservation to the DPD method [120, 121] an internal energy variable ε_i is needed, in addition to position $\mathbf{r}_i$ and velocity $\mathbf{v}_i$ of each particle. Since a particle in the DPD method represents a cluster of microscopic particles (figure 2.1), it can be considered as a thermodynamics system by itself with a well defined internal energy. Temperature and internal energy are connected with each other through the heat capacity at a constant volume c_v:

$$\varepsilon_i = c_v T_i \tag{2.21}$$

where c_v is a constant in a simplest case. Time evolution of the internal energy can be derived through the total energy conservation. The total energy given by:

$$E = \sum_i \varepsilon_i + \frac{1}{2} m v_i^2 + \sum_{i<j} U(r_{ij}) \tag{2.22}$$

Where the mechanical energy is:

$$E_{mec} = \sum_i \frac{1}{2} m v_i^2 + \sum_{i<j} U(r_{ij}) \tag{2.23}$$

Since the total energy should be constant, the variation in the mechanical energy is equal to the variation in internal energy $\mathrm{d}E_{mech} = \mathrm{d}\varepsilon$. If we assume that the total energy is conserved locally:

$$\begin{aligned} &\mathrm{d}\varepsilon_i = \mathrm{d}E_i^{mech} && (a) \\ &\text{or} \\ &\mathrm{d}\varepsilon_i = -\mathrm{d}\left(\frac{1}{2} m v_i^2 + \frac{1}{2}\sum_{j\neq i} U_{ij}\right) && (b) \end{aligned} \tag{2.24}$$

The energy transfer between particles can be calculated explicitly as:

$$\mathrm{d}\varepsilon_i = -\sum_{i\neq j} \mathbf{F}_{ij}^C . \mathrm{d}\mathbf{r}_{ij} + m\mathbf{v}_i . \mathrm{d}\mathbf{v}_i + \frac{1}{2} m \mathrm{d}\mathbf{v}_i . \mathrm{d}\mathbf{v}_i \tag{2.25}$$

by substituting equations (2.2) where the total force is given by equation 2.10 to above equation and neglecting terms of the order dt^2 we obtain:

$$d\varepsilon_i = \sum_j \left(\frac{1}{2}\omega^D(r_{ij}) \left[\gamma_{ij} (\frac{\mathbf{r}_{ij}}{r_{ij}} \cdot \mathbf{v}_{ij})^2 - \frac{\sigma_{ij}^2}{m} \right] - \frac{1}{2}\sigma_{ij}\omega^R(r_{ij}) (\frac{\mathbf{r}_{ij}}{r_{ij}} \cdot \mathbf{v}_{ij}) \Delta t^{-1/2} \xi_{ij} \right) dt \quad (2.26)$$

Equation (2.24) represents work flux q_i^w, while equation (2.26) corresponds to viscous heat flux q^{VH}.

Because of the viscous heat flux, local temperature differences appear in the system and heat conduction has to be considered. Stochastic differential equation for the heat conduction through the discretization of fluctuating Fourier equation of heat conduction is given by:

$$q_i^{HC} = \sum_j \kappa_{ij}(r_{ij})(T_j - T_i)dt + \sum_j \alpha_{ij}(r_{ij})\zeta_{ij} \quad (2.27)$$

Heat conduction consists of a deterministic part proportional to the temperature difference between two particles and a random part with the amplitudes $\kappa_{ij}(r_{ij})$ and $\alpha_{ij}(r_{ij})$, respectively. The random part imposes fluctuations in the heat exchange between particles. In general, the amplitudes depend on positions of particles i and j. Both parts have to be antisymmetric in order to conserve total energy in the system. Therefore, $\kappa_{ij}(r_{ij}) = \kappa_{ji}(r_{ji})$, $\alpha_{ij}(r_{ij}) = \alpha_{ji}(r_{ji})$, and $\zeta_{ij} = -\zeta_{ji}$. ζ_{ij} is selected from a Gaussian distribution with zero mean and unit variance. Here, $\kappa_{ji}(r_{ji})$ and $\alpha_{ji}(r_{ji})$ are functions of r_{ij}, T_i, T_j in the cutoff radius r_c. Similar to the equation (2.20) we define:

$$\kappa_{ij}(r_{ij}) = \kappa_{ij}\omega(r_{ij}) \quad (2.28)$$

$$\alpha_{ij}(r_{ij}) = \alpha_{ij}\sqrt{\omega(r_{ij})} \quad (2.29)$$

where κ_{ij} and α_{ij} are functions of temperature of interacting particles and $\omega(r_{ij})$ is selected as:

$$\omega(r_{ij}) = \begin{cases} 1 - \dfrac{r_{ij}}{r_c} & r_{ij} \leq r_c \\ 0 & r_{ij} > r_c \end{cases} \quad (2.30)$$

The equation for the internal energy is:

$$\frac{d\varepsilon}{dt} = \dot{q}_i \quad (2.31)$$

where q^i is the total heat flux: $q_i = q_i^{HC} + q_i^{VH}$. In DPDe, the governing equations are given by:

$$\mathrm{d}\mathbf{r}_i = \mathbf{v}_i \mathrm{d}t \tag{2.32}$$

$$\mathrm{d}\mathbf{v}_i = \left(\mathbf{F}_i^C + \mathbf{F}_i^D + \mathbf{F}_i^R\right) \mathrm{d}t \tag{2.33}$$

$$\mathrm{d}\varepsilon_i = q_i^{VH} + q_i^{HC} \tag{2.34}$$

The interaction and exchange ranges for conservative force, viscous heating, and heat conduction can be in general selected individually [125].

2.2.2 DPDe Variations

The fluctuation dissipation balance results in:

$$\gamma_{ij} = \frac{\sigma_{ij}^2}{4k_B}\left(\frac{1}{T_i} + \frac{1}{T_j}\right) \tag{2.35}$$

$$\alpha_{ij}^2 = 2\kappa_{ij} T_i T_j \tag{2.36}$$

The simplest choice is $\kappa_{ij} = c_v \kappa_0$, where κ_0 is a mesoscale heat conduction coefficient. The heat conduction term can be written in the form:

$$q^{RE} \equiv q_{ij}^c = \kappa_{ij}\omega_C^2(r_{ij})(T_j - T_i) + \alpha_{ij}\omega_C(r_{ij})\zeta_{ij}\Delta t^{-1/2} \tag{2.37}$$

This expression for the of heat conduction was suggested by Ripoll and Ernst [126].

If we assume that heat exchange due to conduction is inversely proportional to temperature (since by definition $\partial s/\partial \varepsilon = 1/T$) [120, 121], equation (2.27) becomes:

$$q_i^{HC} = \sum_j \kappa_{ij}(r_{ij})\left(\frac{1}{T_i} - \frac{1}{T_j}\right)\mathrm{d}t + \sum_j \alpha_{ij}(r_{ij})\zeta_{ij} \tag{2.38}$$

and the fluctuation dissipation relation of equation (2.36) is changed to:

$$2k_B\kappa_{ij} = \alpha_{ij}^2 \tag{2.39}$$

Based on this equation κ_{ij}, is given by:

$$\kappa_{ij} = \frac{c_v^2 \kappa_0}{4k_B}\left(T_i + T_j\right)^2 \tag{2.40}$$

Therefore, heat conduction is given by:

$$q^E \equiv q^c_{ij} = \frac{\kappa_0 c_v^2}{4k_B T_i T_j}(T_i+T_j)^2 \omega_C^2(r_{ij})\Big(T_j - T_i\Big) + \alpha_{ij}\omega_c(r_{ij})\zeta_{ij}\Delta t^{-1/2} \tag{2.41}$$

Normally, the coefficient of conservative force a_{ij} in equation (2.11) is chosen as a constant. According to the equation (2.16), compressibility in the DPD method is proportional to $a_{ij}/\bar{T}$ and it becomes constant if $a_{ij} = a_0\bar{T}$. We study the effect of different heat conduction terms introduced above and we also investigate the effect of a temperature dependent coefficient ($a^T \equiv a = a_0(T_i+T_j)/2, a_0$ is a constant) versus constant coefficient ($a^c = a_0$). In the next chapter, DPDe is tested for four different approaches denoted as:

1. $a^T q^E$
2. $a^T q^{RE}$
3. $a^c q^E$
4. $a^c q^{RE}$

2.2.3 Integration of DPDe Equations

A good integration scheme, which is simple enough and leads to acceptable computational errors, is borrowed from MD and used in original DPD and DPDe. However, similar to DPD [127] , the integration of DPDe equations has received considerable attention since many integration algorithms do not result in the intended energy conservation accurately. In reference [128], Shardlow like splitting algorithm used for DPDe. Reference [129] employed splitting explicit-Euler (SEM) and splitting with energy reinjection algorithm for DPDe integration. In reference [130], velocity Verlet algorithm (VV) and velocity Verlet Shardlow splitting algorithm (VV-SSA) are applied to DPDe. The results of these studies show that there is an energy drift which can be reduced by choosing a smaller timestep, but it does not completely disappear. In reference [124] energy drift is not reported but energy fluctuations are on order of 10^{-3} which can be too large depending on a problem. Here, we used a simple velocity Verlet algorithm where the viscous heat flux is calculated using equation (2.24). The results show that there is no energy drift and energy fluctuations are on order of machine precision 10^{-14}.

The following velocity Verlet algorithm is used. Velocities and internal energies are updated twice: first for half-step before updating positions and then, at the end of timestep

after updating positions. Positions are updated once every timestep. The scheme consists of two integration parts, where the first part is:

- $\mathbf{v}_i(t+\frac{1}{2}\Delta t) = \mathbf{v}_i(t) + \frac{\mathbf{F}_i(t)}{2m}\Delta t$
- $\varepsilon_i(t+\frac{1}{2}\Delta t) = \varepsilon_i(t) + \frac{1}{2}\Delta t q_i^c - \left(K_i(t+\frac{1}{2}\Delta t) - K_i(t)\right)$
- $\mathbf{r}_i(t+\Delta t) = \mathbf{r}_i(t) + \mathbf{v}_i(t+\frac{1}{2}\Delta t)\Delta t$

and the second one is:

- $\mathbf{v}_i(t+\Delta t) = \mathbf{v}_i(t+\frac{1}{2}\Delta t) + \frac{\mathbf{F}_i(t+\Delta t)}{2m}\Delta t$
- $\varepsilon_i(t+\Delta t) = \varepsilon_i(t+\frac{1}{2}\Delta t) + \frac{1}{2}\Delta t q_i^c - \left(K_i(t+\Delta t) - K_i(t+\frac{1}{2}\Delta t) + U_i(t+\Delta t) - U_i(t)\right)$

where $K_i(t)$ and $U_i(t)$ are kinetic and potential energies of particle i at time t respectively. The total force which is given in equation (2.10) is denoted by $\mathbf{F}_i$. Total heat conduction q_i^c is the summation of heat fluxes (q^E or q^{RE}) between particle i and its neighbors. Evolution of internal energy is governed by the two parts. The first part is due to heat conduction that amounts for heat transfer to/from particle i because of heat fluctuations and local temperature gradients. The second part is equal to the variation in mechanical energy.

2.3 Implementation of a Temperature Gradient

We employ two ways for imposing the temperature gradient, (i) by introducing a heat with a constant rate or (ii) by fixing temperature in two parts of the system at two different values.

In the first method, a temperature gradient is imposed by fixing an amount of heat rate with $\dot{Q}$ that the system receives in a slab while and the exactly same amount of heat rate $\dot{Q}$ is taking out at another slab. These two slabs can be identified as the hot and cold slabs respectively. The heat rate $\dot{Q}$ is distributed uniformly between N particles within the corresponding slab, such that each particle receives $\dot{q}_i = \dot{Q}/N$. The temperature of the particles in the considered slab is then updated as $T_i(t+\mathrm{d}t) = T_i(t) + \dot{q}_i/c_v$. The fluid between these slabs develops a well defined temperature gradient. The average temperature in the system remains constant since the total energy of the system is conserved.

In the second method, the temperature gradient is imposed by fixing temperatures at two walls with a cold temperature T_c, and hot temperature T_h. In this case, the temperature gradient is well controlled while the heat exchange is a result of the system parameters and

the temperature gradient. In DPDe, fluid particles in close vicinity of the wall have the same temperature as the wall. In the MPC method fluid temperature changes linearly close to the wall [118].

In this thesis, both methods to impose a temperature gradient, are used. In chapters 3 and chapter 4, the temperature gradient is implemented by a constant heat flux and fixed temperature, respectively. In chapter 6, we use both of methods.

Chapter 3

Consistency Check of Various Approaches in DPDe

3.1 General Consideration

In this chapter, a detailed investigation of the energy-conserving DPD method is presented. With this aim, fluid with homogeneous and inhomogeneous temperatures is simulated and four models based on different definitions of conservative force and heat exchange introduced in section 2.2.2 are tested. First, we investigate the performance of these models by looking at energy conservation, different definitions of temperature, and radial distribution function. Comparison between different models under a thermal gradient is performed. Details of investigation of energy transfer are also presented. The consistency check and analytical approach for the approximation of conductivity coefficient are outlined. The last part of this chapter is devoted to the comparison to a real fluid.

3.2 Fluid at a Homogeneous Temperature

In order to validate the simulation model, we consider various relevant aspects using a system with a constant homogeneous temperature.

3.2.1 Simulation Setup and Parameters

First, we consider the case of a simple fluid in equilibrium such that periodic boundary conditions are applied at the box boundaries. Box size is $L_z = 20r_c, L_y = L_x = 10r_c$. Number density of fluid is $\rho = 3$, the conservative and random force coefficients are $a_0 = 15$ and $\sigma = 3$, respectively. These parameters are chosen to simulate a common fluid such as water

in DPD. The heat capacity c_v/k_B should be large enough (much larger than one), since this number is a measure of the size of DPD particles [126] and we choose $c_v = 200$. The average temperature of the system is $k_B\bar{T} = 1$, the cutoff radius $r_c = 1$ and, the mass of particles $m = 1$. The time unit in terms of these choices is introduced as $\tau_0 = \sqrt{k_BT/mr_c^2}$.

The heat conductivity coefficient depends on the model employed as we want to compare q^E and q^{RE}. In order to guarantee the same conductivity in the fluid, coefficients in front of $\left(T_j - T_i\right)$ in equations (2.41) and (2.37) should be equal. Therefore we choose:

$$\kappa_0^{RE} = \frac{\kappa_0^E c_v}{4k_B}\left(\frac{(T_i+T_j)^2}{T_iT_j}\right) \tag{3.1}$$

According to equation (3.1), if $\kappa_0^E = 0.001, c_v = 200$, and we approximate $T_i = T_j = 1.0$, then $\kappa_0^{RE} = 0.2$. Other parameters are adjusted for different situations.

3.2.2 Validation of Models

Validation of models is performed with respect to three aspects: (*i*) verification of energy conservation (*ii*) definition of temperature (*iii*) radial distribution function.

Verification of Energy Conservation

DPDe is formulated in the way that it conserves energy. We have tested energy conservation for four models and different timesteps. Maximum error in energy is measured by maximum difference in total energy between two consecutive steps divided by the initial total energy $E_{t=0}$. There is nearly no difference between the results for different timesteps $(0.005, 0.01, 0.02, 0.05)$ and numbers of particles $(6\times10^3, 6\times10^4, 2\times10^5, 6\times10^5)$. Energy drift is not observed and maximum fluctuations of energy are on the order of 10^{-14}.

Note that because the heat flux obeys total energy conservation, energy is conserved on the order of machine precision. References [128, 129] suggest to divide the integration into two parts: first Hamiltonian evolution where conservative force is taken into account and second fluctuation/dissipation part where dissipative and random forces are considered. The internal energy is updated in the second part. The first part is integrated by a standard velocity-Velrlet algorithm and different algorithms are used for the second part. In the Shardlow's splitting algorithm, viscous heat flux obeys energy conservation for every collision. Since the potential is calculated in the Hamiltonian evolution, viscous heat flux is updated by variation of kinetic energy: $\delta\varepsilon_i = -\delta K_i$ and $\delta\varepsilon_j = \delta\varepsilon_i$. In the rest of this work and other papers [124, 130], heat flux is calculated using equation (2.26).

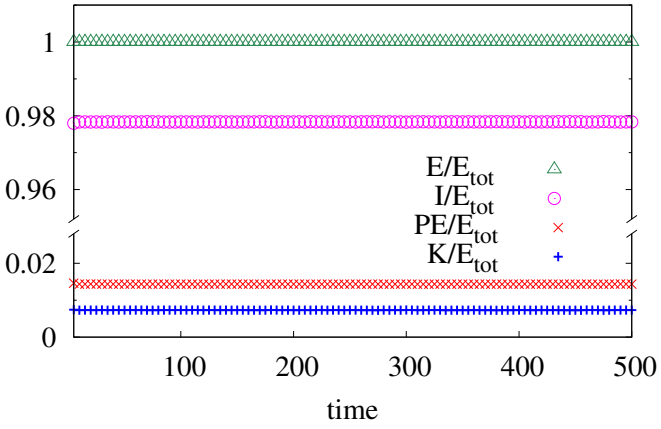

Fig. 3.1 Time evolution of total energy E and its components (internal I, kinetic energy K and, potential energy PE) normalized by initial total energy E_{tot}. The kinetic and potential energies have a small contribution to the total energy. The total energy is conserved up to the order of machine precision. Note that energy axis (y-axis) is broken.

Reference [124] reports the fluctuation of energy on the order of 10^{-3}. References [128] and [129] report energy drifts in their algorithms. In reference [129] for Shardlow's splitting algorithm (SSA) and Splitting with energy reinjection (SER), energy drifts are respectively 2.12×10^{-5} and 9.0×10^{-6} for $\Delta t = 0.006$ and the time period 10.0. In this work for the time period of at least 2.5×10^4 and timestep $\Delta t = 0.01$, relative energy fluctuation is on the order of 10^{-14} and the energy drift is not observed. In the reference [128], in order to remove energy drift, the variation of energy between two consecutive steps is added uniformly to all particles.

Figure 3.1 shows the total energy of the system and its components. The internal energy constitutes the largest contribution to the total energy. The ratios of the internal energy and kinetic energy to the total energy are 0.978 and 0.0073 respectively. The ratio of the internal energy to the kinetic energy is 133.86 which is close to a semi-analytical approximation (see subsection of radial distribution function). The potential energy is also very small and with our parameters it is twice the kinetic energy. In addition to consistency of the total energy, internal, kinetic and potential energies also exhibit no drift.

Measuring Temperature

The normal way of calculating temperature is averaging over the kinetic energy:

$$k_B T = \langle \frac{1}{3} m \|\mathbf{v}\|^2 \rangle \tag{3.2}$$

Here, it will be called kinetic temperature. In contrast to kinetic temperature, another temperature is introduced in section 2.2.1 that is called internal temperature. The internal temperature is calculated by averaging over particle's internal energy divided by heat capacity at constant volume: $\langle \varepsilon_i / c_v \rangle$. Comparison of kinetic temperature T_K and internal temperature T_I for $a^T q^E$ model is shown in figure 3.2. All models have same behavior. For the largest integration timestep $\Delta t = 0.05$ employed, different average values for T_K and T_I are obtained. Non-equal values mean that the model presents an artifact for these large values of timestep Δt. Definition of temperature in this situation is ambiguous. It means that these models are not valid for such large timesteps $\Delta t = 0.05$. In fact, energy flows from the internal part to kinetic part at the beginning of the simulation.

In general, kinetic and internal temperatures obey different distribution functions which explains the different variations in figure 3.2 even for the case of a smaller integration timestep, where no artifacts are encountered. The kinetic temperature is determined by particle velocities, and the distribution function of velocities in the microcanonical ensemble with a large number of particles is the Boltzmann distribution function $\Psi_B(v)$ [131]. The average of the kinetic temperature according to equation (3.2) is given by:

$$\bar{T}_K = \frac{1}{3} \int_0^{N k_B \bar{T}} v^2 \Psi_B(v) \mathrm{d}v \tag{3.3}$$

where N is the number of particles in the system.

Distribution function of internal energy [125] in the microcanonical ensemble (see appendix A) is:

$$\psi(\varepsilon) = \frac{1}{M} \frac{1}{I} \left(\frac{\varepsilon}{I} \right)^{\alpha} \left(1 - \frac{\varepsilon}{I} \right)^{(N-1)(\alpha+1)-1} \tag{3.4}$$

where I is the total internal energy and M is normalization factor which is given by:

$$\frac{1}{M} = \frac{\Gamma(N(\alpha+1))}{\Gamma(\alpha+1)\Gamma((N-1)(\alpha+1))} \tag{3.5}$$

According to equation (2.21) the average of internal temperature is:

$$\bar{T}_I = \frac{1}{c_v} \int_0^I \varepsilon \psi(\varepsilon) \mathrm{d}\varepsilon \tag{3.6}$$

So, the variances of the internal and kinetic temperatures are:

$$\begin{aligned} \sigma^2_{var}(T_K) &= \frac{1}{9} \sigma^2_{var}(v^2) = \frac{1}{9} (\langle v^4 \rangle - \langle v^2 \rangle^2) \\ \sigma^2_{var}(T_I) &= \frac{1}{c_v^2} \sigma^2_{var}(\varepsilon) = \frac{1}{c_v^2} (\langle \varepsilon^2 \rangle - \langle \varepsilon \rangle^2) \end{aligned} \tag{3.7}$$

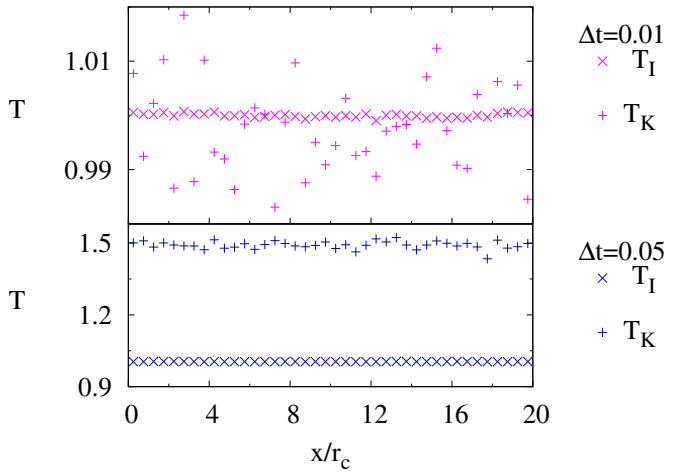

Fig. 3.2 Kinetic temperature T_K and internal temperature T_I along the box length with periodic boundary conditions for two different timesteps. Kinetic and internal temperatures are calculated through the kinetic and internal energies respectively. $\Delta t = 0.05$ leads to artifacts such that $T_I \neq T_K$.

We obtain $\sigma^2_{var}(T_I) = 3/c_v = 0.015$ and $\sigma^2_{var}(T_K) \approx 0.67$. Remarkably, the variance of internal temperature is smaller than the variance of kinetic temperature.

According to figure 3.1, the ratio of the internal energy to the kinetic energy is 133.86 which can be explained by the equality of the two different temperatures $T_K = T_I$, where $T_K = 2/3K$ and $T_I = I/c_v$ so that $I/K = 2c_v/3 = 133.3$.

Radial Distribution Function

Radial distribution function (RDF) describes how the density changes as a function of distance from a reference particle. It represents microscopic details which can be connected to the macroscopic properties of the system e.g. compressibility and pressure. RDF for four models introduced here exhibits the same behavior. Note that, since the temperature is homogeneous, we do not expect any difference between a^T and a^c or q^E and q^{RE}. Figure 3.3 shows RDF for $a^T q^E$ model with various values of the timestep. There is a slight difference when Δt is changed from 0.02 to 0.05. Therefore, timestep should be smaller than $dt < 0.05$.

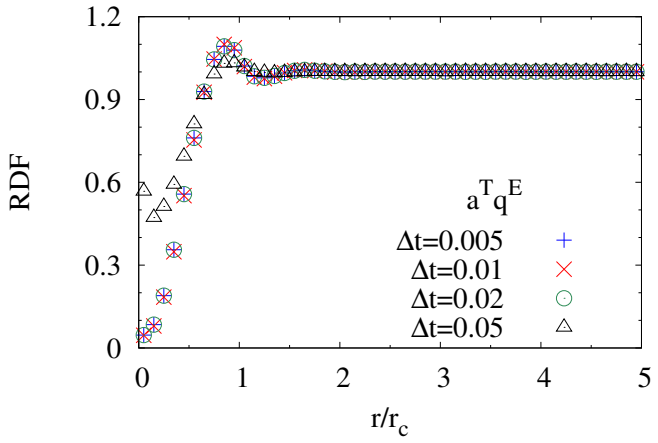

Fig. 3.3 Radial distribution function of $a^T q^E$ model for different timesteps. All models have the same RDF.

3.3 Fluid Under an Inhomogeneous Temperature

3.3.1 Implementation of a Thermal Gradient

In order to test the method in the presence of temperature inhomogeneities, we study the behavior of a DPD fluid in a linear temperature gradient. The simulation box is $10r_c \times 10r_c \times 20r_c$ and periodic boundary conditions are applied in all directions. The average fluid density and temperature are $\rho = 3$ and $\bar{T} = 1$ respectively. There are different strategies to impose a thermal gradient with respect to periodic boundary conditions. One of them is the velocity exchange algorithm that was introduced for binary Lennard-Jones liquids by Reith and Müller-Plathe [132] and also used in MPC simulation by Lüserbrink and Ripoll [118]. In this chapter, the hot and cold layers are as indicated in figure 3.4. The system in the hot layer ($10.0 < z < 10.5$) receives heat that is equal to $\dot{Q}$ and in the cold layer ($0.0 < z < 0.5$), the system loses $\dot{Q}$. Therefore, the total energy of the system remains constant. In the cold (hot) layer, the heat flux $\dot{Q}$ is divided by the number of particles currently located in the layer and is equally subtracted from (added to) the internal energy of each particle in that layer. Periodic boundary conditions applied to the system result in imposition of a thermal gradient over half of the box. This transfer of energy in localized bands mimics the connection of the system with thermal baths. The system physically adopts the temperature profile between the thermalizing bands, where the measurements are performed.

Density profiles for various models reveal that there exist a difference between a^T, a^c models under the temperature gradient (see figure 3.5). Up triangles refer to q^E and down

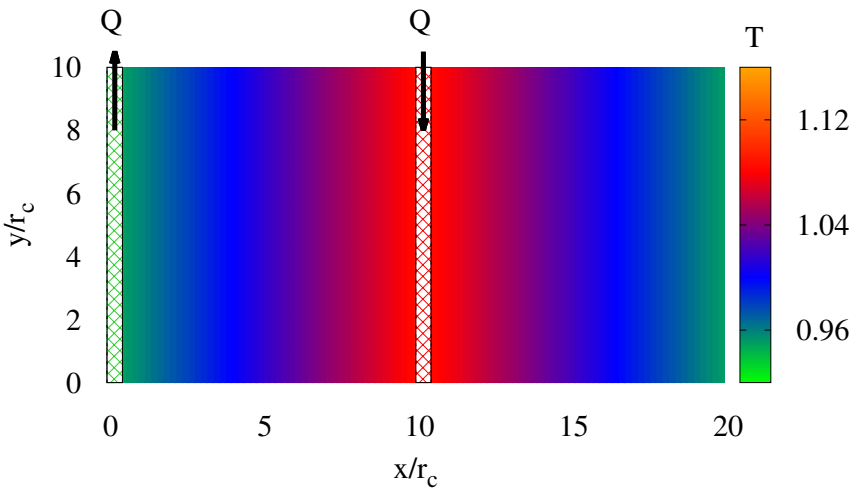

Fig. 3.4 Temperature profile at the steady state under a thermal gradient. The thermal gradient is imposed by adding/removing heat Q in the marked areas. Periodic boundary conditions are applied.

Table 3.1 Temperature profile data for different models. Presented values are valid for both q^E and q^{RE} models.

Model	T(x)	$\dot{Q}$	T_{max}	T_{min}
$a=0$	$0.0180x+0.907$	280	1.074	0.930
a^T	$0.0181x+0.906$	270	1.073	0.928
a^c	$0.0182x+0.903$	275	1.072	0.926

ones correspond to q^{RE}. In order to investigate the contribution of the conservative force, ideal fluid is considered. Blue symbols correspond to $a=0$ so $\mathbf{F}_{ij}^C=0$, representing an ideal fluid. Pink and green symbols refer to a^T and a^c models respectively. Temperature gradients are nearly same. There is no appreciable difference between q^E and q^{RE} models. The a^T model closer to the ideal fluid. In order to obtain the same temperature gradient, individual $\dot{Q}$ is used in each system. Table 3.1 presents the temperature gradient and $\dot{Q}$ for each model.

3.3.2 Characterization of Heat Transfer

The law of heat conduction or Fourier's law in one dimension represents a linear relation between the heat rate and the temperature gradient in an isotropic medium:

$$\frac{\mathrm{d}Q}{\mathrm{d}t}=\kappa A\frac{\mathrm{d}T}{\mathrm{d}z} \tag{3.8}$$

where κ is the thermal conductivity and A is the energy interchange area. If DPDe models have a constant thermal conductivity κ, the rate of heat over the temperature gradient should

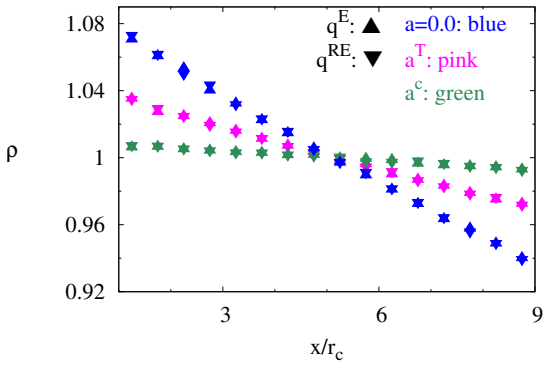

Fig. 3.5 Steady-state density profiles for the same thermal gradients of different models. Up and down triangles refer to q^E and q^{RE} models respectively. Blue symbols correspond to an ideal fluid. Pink symbols represent a^T and green symbols display a^c model. Here, different models have nearly same temperature gradient imposed by different $\dot{Q}$. There is no difference between q^E and q^{RE}. In comparison with a^c, a^T behaves closer to ideal fluid.

be constant for different heat rates. Figure 3.6a shows three temperature profiles for different $\dot{Q}$ using the $a^T q^E$ model. It is clear that by applying a large $\dot{Q}$, the system attains a large temperature gradient. Figure 3.6b shows fitting errors for two situations: the small heat rate $\dot{Q} = 50$ and the large one $\dot{Q} = 1000$. The circles show deviation from the expected linear fits. Since fluid temperature and density change locally due to the thermal gradient, the heat conduction coefficient might be locally different for the case of high $\dot{Q}$ (green circles), resulting in larger errors for the linear fit. Nevertheless, the errors are small (on the order of 0.5%). Heat conduction coefficient as a function of temperature and density is shown in figure 3.7a for the $a^T q^E$ model while other models show a similar behavior. Thus, the conductivity coefficient κ is a function of temperature T and density ρ. This dependence can be fitted well by a quadratic function $\kappa = 0.36 c_v k_B T^2 + 0.21 n^2 c_v^2 \kappa_0$. In section 3.3.4 the dependence of κ on temperature and density is discussed in more details. Dependence of thermal conductivity on temperature and density is a well known behavior of fluids which was investigated experimentally and theoretically [133–136].

Figure 3.7b shows heat conduction coefficient κ versus heat rate. Since κ is a function of temperature and density, it is estimated by fitting near the middle of the temperature gradient $(z_{T_{max}} + z_{T_{min}})/2$ where the density and temperature are close to average values. There is no substantial difference between various models and κ is nearly a constant for the whole range of investigated heat rates.

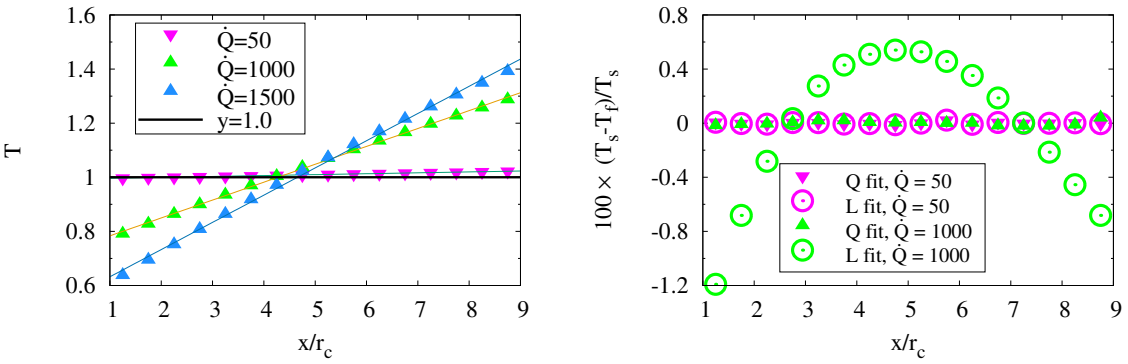

(a) (b)

Fig. 3.6 (a) Temperature profiles of $a^T q^E$ model for three $\dot{Q}$. The larger $\dot{Q}$ leads to the larger temperature gradient. (b) Percentage error of linear and quadratic fit to the temperature gradient for small and large $\dot{Q}$. In the case of small $\dot{Q}$, both fits lead to small errors, indicating a linear temperature profile. In case of the large $\dot{Q}$, the temperature profile is a quadratic function.

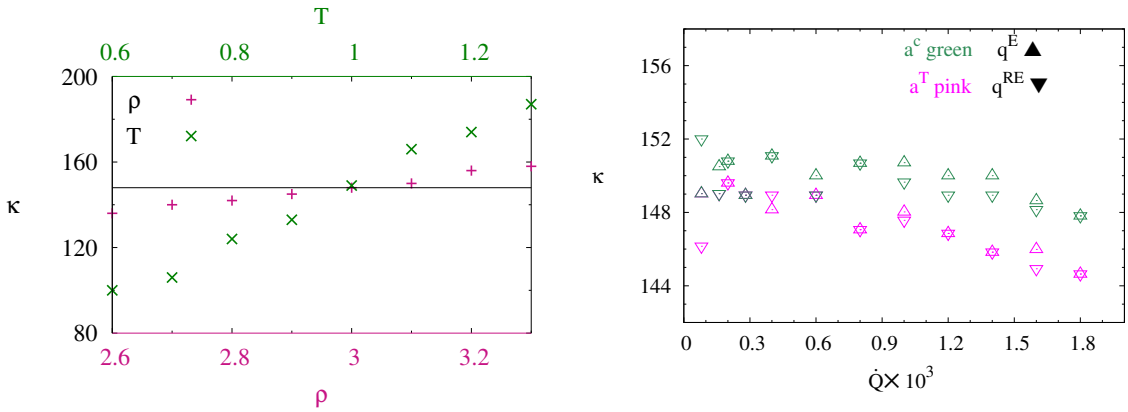

(a) (b)

Fig. 3.7 (a) Heat conduction coefficient as a function of temperature and density for weak thermal gradients. The average density (temperature) of the system is $\rho = 3$ ($\bar{T} = 1$), where κ is measured as a function of temperature (density). (b) Heat conduction coefficient κ versus heat flux $\dot{Q}$. Different models are specified by colors and symbols: up and down triangles refer to q^E and q^{RE}, respectively and the green symbols correspond to a constant conservative force coefficient a^c and the pink symbols refer to a^T.

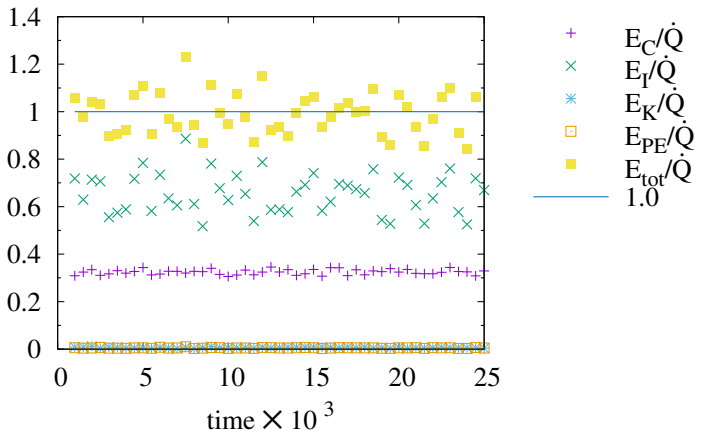

Fig. 3.8 Ratio of energy transfer through a measuring plane at $x = 8r_c$ by different ways. Due to particle diffusion, energy (kinetic energy E_K, internal energy E_I and potential energy E_{PE}) is transfered between the two sides of the plane. Besides, energies transfered by conduction. Kinetic and potential energies do not play a significant role in heat transfer. This graph is illustrated for $\dot{Q} = 600$. Total heat transfer is equal to $\dot{Q}$ within the statistical accuracy.

3.3.3 Heat Transfer

Until now, κ has been calculated with the assumption of total energy conservation. In the other words, the amount of transferred heat through an imaginary plane has to be equal to $\dot{Q}$. In order to test this and to clarify mechanisms of heat transfer, we focus on heat transfer through a plane. Figure 3.8 shows the energy transferred across the measuring plane at $x = 8r_c$, for different contributions. The first type of energy transfer is heat flux due to conduction between particles at the two sides of the plane. Note that within the cutoff radius r_c, heat is transfered by conduction E_C, since average temperatures at the two sides are different. The density profile does not change with time and thus, the mass flux is zero. However, particles can cross the plane due to their random motion. At the short times, particles can cross the plane due to diffusion and they have different internal and kinetic energies at the two sides due to the thermal gradient. Therefore, energy also flows through particle diffusion by transferring kinetic energy E_K and internal energy E_I through the plane. Flux of potential energy E_{PE} does not significantly contribute to energy transfer, as it has a negligible ratio to the total energy shown in figure 3.1.

The largest contributions to the energy transfer are E_C and E_I. The density and temperature gradients change the ratios of E_C and E_I to the total energy transfer, depending on the position of the measuring plane. Figure 3.9a shows E_C and E_I contributions versus heat

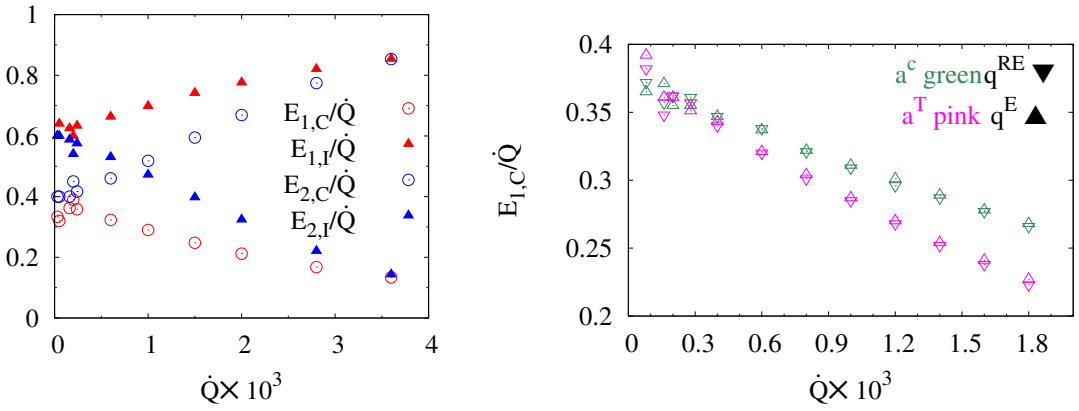

(a) (b)

Fig. 3.9 (a) Conduction and internal energy contribution to the energy transfer at two measuring planes. 1 and 2 refer to the planes at $z/r_c = 8$ and $z/r_c = 2$ respectively. (b) Energy transfer by q^{HC} at $z/r_c = 8$ for different models. At small $\dot{Q}$, fluctuation is high. If $\dot{Q}$ is large enough, different models behave the same way.

rate at two planes for $a^T q^E$ model. Red and blue symbols refer to the plane at $z/r_c = 2$ and $z/r_c = 8$ respectively. As we go from the hot (cold) reservoir, to the other side of temperature gradient E_C rises (decreases), while E_I decreases (rises). Note that at the point with a lower temperature, the density is higher and E_C is larger (a higher density leads to a higher heat exchange). Furthermore, the lower temperature results in lower diffusion and E_I is weaker. On the other hand, at the point with a higher temperature and lower density, E_I is larger due to a more effective diffusion. At high $\dot{Q}$, the temperature gradient is stronger and temperature (density) at $z/r_c = 8$ ($z/r_c = 2$) is larger resulting in a stronger diffusion (conduction).

Figure 3.9b shows energy transfer by conduction at $z/r_c = 8$ versus $\dot{Q}$ for different models. By increasing $\dot{Q}$, conduction $E_{1,C}$ has less contribution to total energy transfer for all models, even though the absolute value of $E_{1,C}$ is larger than for small $\dot{Q}$. At the higher density and lower temperature ($z/r_c = 2$), the main way of energy transfer is conduction. Different models exhibit same behavior. The small shift between a^T and a^c represents the different response of the system to the thermal gradient that is mentioned in table 3.1.

3.3.4 Analytical Approach to Energy Transfer

In this section, we will find expressions for different components of energy transfer, which will allow us to obtain analytical expression for the heat conduction coefficient κ.

Heat conduction between two particles at two sides of the measuring plane is calculated by equation (2.41) or (2.37). These two equations correspond to different models, although

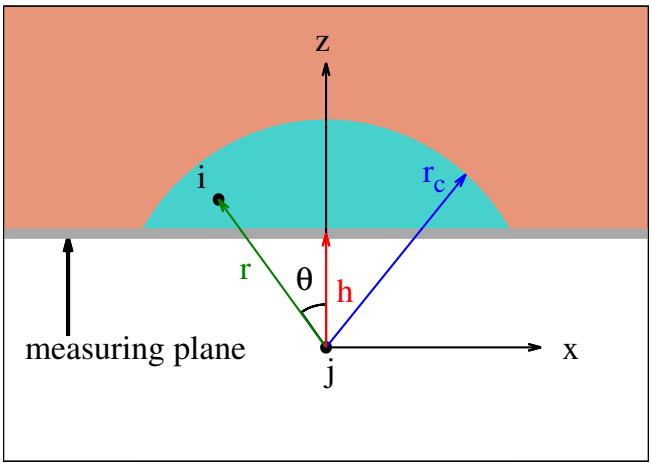

Fig. 3.10 Integration domain for the heat conduction.

the underling physics is the same in both cases. Thus, we will focus on equation (2.41) and there is the same derivation for equation (2.37). The random part on average will be zero and we assume $T_i \approx T_j \approx T_0$ where T_0 is the temperature at the position of the plane. Therefore, heat conduction between two particles at the two sides can be calculated as:

$$Q^c_{i,j} = c_v^2 \kappa_0 (T_j - T_i) \omega^2_{HC} \tag{3.9}$$

According to the temperature profile of the system, $T_j - T_i = \nabla T \Delta z = \nabla T r_{ij} \cos(\theta)$ where r_{ij} is the distance between two particles and θ is the angle between r_{ij} and $z-$ axis, see figure 3.10. The total heat conduction between particle j and its neighbor on the other side of the plane is:

$$Q_j = n \int_0^{2\pi} \mathrm{d}\phi \int_0^{\arccos(h/r_c)} \mathrm{d}\theta \int_h^{r_c} \mathrm{d}r_{ij} r_{ij}^2 \sin(\theta) Q^c_{i,j} g(r_{ij}) \tag{3.10}$$

where n is number density, h is the distance between the particle j and the measuring plane, and $g(r_{ij})$ is the radial distribution function. In the case of ideal fluid $g(r_{ij}) = 1.0$, but the non-ideal fluid has a not constant RDF and the integration should be performed numerically. Total heat transfer by conduction is calculated by integrating over all neighbors of j particle at the opposite side of the measuring plane:

$$E_C = nA \int_0^{r_c} Q_j(h) \mathrm{d}h = \pi n^2 c_v^2 \kappa_0 A \nabla T H(r_c) \tag{3.11}$$

where:

$$H(r_c) = \int_0^{r_c} \mathrm{d}h \left(1 - \frac{h^2}{r_c^2}\right) \int_h^{r_c} \mathrm{d}r g(r) \omega^2_{HC} r^3 \tag{3.12}$$

Table 3.2 Comparison of analytical approach and simulation data for heat conduction.

Plane	Simulation data	Analytical approach	Error
2.0	277	302	8%
5.0	230	266	14%
8.0	195	232	16%

where A is the area of the measuring plane. $H(r_c)$ is computed numerically and for our input parameters $H(r_c) = 0.0587$. Table 3.2 shows the comparison of analytical approach and simulation data for heat conduction. The errors here are less than 16%.

Heat transfer by diffusion can be calculated by considering a plane in the perpendicular direction to the temperature gradient ($z =$ constant). If $\mathrm{d}T/\mathrm{d}z > 0$, particles which are coming from the hot part have higher kinetic and internal energies than particles which are crossing the plane from the cold part. Therefore, a net flux of energy comes from the hot part and internal energy transfer is:

$$\begin{aligned} \Delta\varepsilon &= \bar{\varepsilon}(z+\lambda_{MFP}) - \bar{\varepsilon}(z-\lambda_{MFP}) \\ &= 2\lambda_{MFP}\frac{\partial\bar{\varepsilon}}{\partial z} \\ &= 2\lambda_{MFP}\frac{\partial\bar{\varepsilon}}{\partial T}\frac{\mathrm{d}T}{\mathrm{d}z} \\ &= 2\lambda_{MFP}c_v\frac{\mathrm{d}T}{\mathrm{d}z} \end{aligned} \tag{3.13}$$

where λ_{MFP} is the mean free path. Mean free path represents an average distance for particles which crossed the plane at $z =$ constant, since their last collision there.

The mean free path is calculated as $\lambda_{MFP} = \tau_c\bar{v}_z$ where τ_c is the collision time and $\bar{v}_z$ is the average velocity of particles crossing the plane in one direction. Collision time, also known as relaxation time, is the mean time between two consecutive collisions. Due to collisions, the velocity of particles changes and the velocity of a particle as time passes will be independent of the initial velocity. Thus, the collision time is the mean lifetime of the velocity autocorrelation function. In order to find an expression for collision time, we consider the second law of motion (equation (2.2)). The total DPD force has three parts (see equation (2.10)). The effect of conservative force is taken into account by the radial distribution function. The dissipative force can be divided into two parts, The first one is proportional to the velocity of the reference particle and the second one is related to the velocity of its neighbors and their relative positions which in homogeneous media are zero

on average. Therefore:

$$\frac{\mathrm{d}\mathbf{v}_i}{\mathrm{d}t} + \frac{\mathbf{v}_i}{\tau_c} = \frac{\mathbf{F}_i^R}{m} \tag{3.14}$$

where:

$$\tau_c^{-1} = \frac{4\pi\gamma n}{3m} \int_0^{r_c} \mathrm{d}r g(r) r^2 \omega^D(r) \tag{3.15}$$

The random force on average is zero and:

$$\begin{aligned} \langle \mathbf{F}^R(t_i).\mathbf{F}^R(t_j) \rangle = 2\gamma k_B T \left(4\pi \int_0^{r_c} \mathrm{d}r g(r) r^2 (\omega^R(r))^2 \right) \\ \times \delta(t_i - t_j) \end{aligned} \tag{3.16}$$

Consequently, equation (3.14) represents the Langevin equation whoose solution is:

$$\mathbf{v}_i(t) = \mathrm{e}^{-t/\tau_c} \mathbf{v}_i(0) \tag{3.17}$$

We solve the equation (3.15) numerically with the predefined parameters and radial distribution function in figure 3.3:

$$\tau_c = 0.42 \frac{mT}{n} \tag{3.18}$$

The validity of the approximations considered here is tested against simulation results shown in figure 3.11. The line in this figure corresponds to the analytical approach and points present simulation data. Simulation data show collision times based on the velocity autocorrelation function for the system in equilibrium at different temperatures and densities. There is a good agreement between them.

The average velocity of particles which cross the plane is:

$$\bar{v}_z = \frac{\int_0^\infty \mathrm{d}v_z v_z f(v_z)}{\int_0^\infty \mathrm{d}v_z f(v_z)} = \sqrt{\frac{\pi k_B T}{2m}} \tag{3.19}$$

Note that the denominator in equation (3.19) is the new normalization factor due to the limits of integral in the numerator.

The total heat transfer by the internal energy is $E_I = \dot{N}\Delta\varepsilon$ where $\dot{N}$ is the flow rate of particles crossing the plane from hot or cold part. We assume that the mean free path is small such that the temperature is almost constant and the Maxwell Boltzmann distribution function $\psi_B(v)$ is valid. Therefore the flow rate from the cold (hot) part includes particles

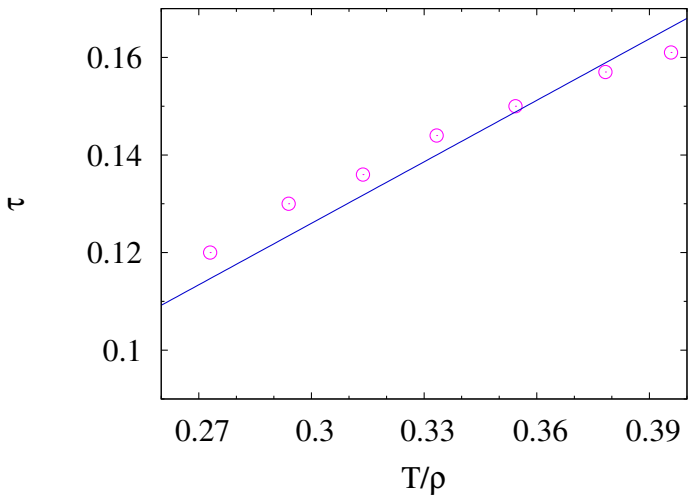

Fig. 3.11 Collision time versus temperature over density. The line represents analytical approach and points show simulation results.

with positive (negative) velocities and:

$$\begin{aligned}\dot{N} &= nA\int_0^\infty \psi_B(v_z)v_z \mathrm{d}v_z \\ &= nA\sqrt{\frac{k_BT}{2\pi m}}\end{aligned} \tag{3.20}$$

Hence, energy transfer by internal energy is:

$$E_I = 0.42Ac_v k_B T^2 \nabla T \tag{3.21}$$

Table 3.3 shows the comparison of the analytical approach and simulation data for heat transfer by internal energy. There is a good agreement between them within the statistical accuracy.

Kinetic energy and potential energy have a much smaller contribution to the energy transfer such that we do not consider them here. Therefore, the total energy transfer is:

$$\dot{Q} = \left(0.42c_v k_B T^2 + 0.18n^2 c_v^2 \kappa_0\right) A\nabla T \tag{3.22}$$

which means that $\kappa = 0.42c_v k_B T^2 + 0.18n^2 c_v^2 \kappa_0$ and with the parameters selected here $\kappa = 149$, in a good agreement with figure 3.7b. According to figure 3.7a, κ is a function of number density and temperature as $\kappa = 0.36c_v k_B T^2 + 0.21n^2 c_v^2 \kappa_0$. A difference in percents between the analytical values and the simulation values (fitting parameters) is less than 16%.

Table 3.3 Comparison of analytical approach and simulation data for heat transfer by internal energy.

Plane	Simulation data	Analytical approach	Error
2.0	300	260	16%
5.0	367	340	8%
8.0	399	427	7%

3.4 Energy Stability

The presented models are unstable when the input of energy per time $\dot{Q}$ is too large. By applying $\dot{Q}$ larger than a limit $\dot{Q}_{max}$, in some parts of the system particles may obtain a negative internal energy which is clearly not correct. At the same time, kinetic temperature may increase which means a continuous transfer of internal energy to the kinetic energy leading to system instability in spite of the fact that the total energy is conserved. A negative internal temperature is an artifact of the method and is a consequence of the negative internal energy (see equation (2.21)) which only occurs in this unstable case.

The maximum heat rate $\dot{Q}_{max}$ depends on the system parameters and very strongly on κ_0. In fact, by decreasing κ_0 maximum heat that can be transfered decreases strongly in spite of conductivity of the system which does not change so much. For $\kappa_0 = 10^{-3}, 10^{-7}, 0.0$, maximum energy transfers are about $\dot{Q} = 3600, 400, 20$ in $a^T q^E$ and conductivity coefficients from equation (3.22) are $\kappa = 149, 72.0, 72.0$ respectively. While the conductivity coefficient κ with $\kappa_0 = 10^{-3}$ is half of that with $\kappa_0 = 10^{-7}$, the maximum heat rate $\dot{Q}_{max}$ changes almost by a factor 10. It can be explained by the Brownian motion of DPD particles. The energy transfer by internal energy E_I refers to the random motion, so that it is slow and needs some time. On the other hand, when κ_0 is small (i.e. E_C is small), random motion does not have enough time to transfer heat and particles in the cold slab lose energy continuously in time such that at some point they reach a negative internal energy.

3.5 Calculation of the Relevant Dimensionless Numbers

With an aim to compare our results with those for real fluids, we consider two dimensionless numbers: Prandtl number Pr and Schmidt number Sc which can be calculated both in simulations and in experiments.

Prandtl number is defined as the ratio of momentum diffusivity to thermal diffusivity and is given by:

$$\mathrm{Pr} = \frac{\eta C_P}{\kappa} \tag{3.23}$$

where η and C_P are dynamic viscosity and specific heat capacity of constant pressure respectively. For most liquids this number is within 1-10 which means that the transport of energy is smaller than the transport of momentum.

In order to provide an estimation for the Prandtl number in our simulation model, we analyze the values of C_P and η. The relation between C_P and the specific heat capacity at constant volume C_V is given by:

$$\frac{C_P}{C_V} = \left(\frac{\partial V}{\partial P}\right)_S \Big/ \left(\frac{\partial V}{\partial P}\right)_T \tag{3.24}$$

According to the first law of thermodynamics, the internal energy and heat variation are related by:

$$\mathrm{d}E_I = \mathrm{d}Q - \mathrm{d}w \tag{3.25}$$

where dw is the variation of work done by the system on its surroundings. For an isolated system or isoentropic process, entropy S is constant and there is no heat flux such that $\mathrm{d}E_I = -\mathrm{d}w$. For a small amount of work on the system, since c_v is large and $\mathrm{d}E_I = \sum_N c_v \mathrm{d}T_i/N = c_v \mathrm{d}T$, we can assume d$T$ is negligible (error is less than 1/200 or 0.005) and T is a constant such that isothermal and isoentropic cases are similar. Therefore, $(\partial V/\partial P)_S \approx (\partial V/\partial P)_T$, so that $C_P \approx C_V$.

On the other hand, $C_V = c_v$ since the total heat is distributed equally between particles $Q = \sum_i Q_i = \sum_i c_v \mathrm{d}T_i$ resulting in:

$$Q = NC_V \Delta T$$

where $\Delta T = \sum_i \frac{1}{N} \mathrm{d}T_i$.

Dynamic viscosity η can be measured from simulations of a reverse-Poiseuille flow in a rectangular channel with a size of $20r_c \times 40r_c \times 20r_c$ and periodic boundary conditions at all boundaries. Here, the flow is implemented using a body force in opposite directions but of the same magnitude in the upper and lower halves of a box in x-direction. This method guaranties that the average velocity is zero at the boundaries (without walls, eliminating problems with density fluctuations close to the wall). Figure 3.12 shows the velocity profile which forms in the x-direction. The Stokes equation for half of the box gives:

$$\frac{\mathrm{d}^2 v_x}{\mathrm{d}y^2} = -\frac{1}{\eta} \nabla P \tag{3.26}$$

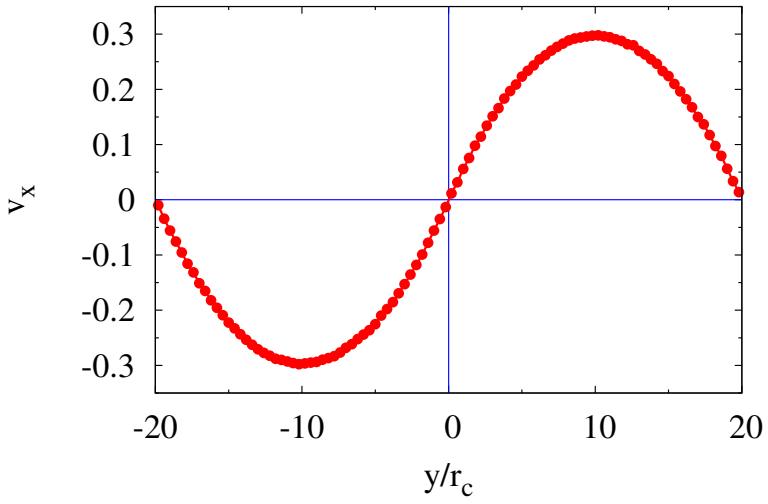

Fig. 3.12 Velocity profile for the reverse-Poiseuille flow

where $\nabla P = \Delta P/\Delta x = fn$ and f is the body force. The boundary conditions are:

$$\frac{\partial v_x}{\partial y}|_{y=\pm 5} = 0, \qquad v_x(0) = v_x(y = \pm 20) = 0, \tag{3.27}$$

and therefore:

$$v_x = -\frac{fn}{2\eta}\left(y^2 - 5y\right) \tag{3.28}$$

By fitting the data with equation (3.28), we obtain a value for η shown in figure 3.12.

Using equation (3.23) together with a value of κ from figure 3.7b, the Prandtl number in our system is 2.0. For example, the Prandtl number of water at room temperature is around $6-7$.

The Schmidt number Sc provides a comparison between the transport of momentum and mass. Sc is defined by the ratio of dynamic viscosity η and mass diffusivity ρD:

$$\mathrm{Sc} = \frac{\eta}{\rho D} \tag{3.29}$$

where D is the translational diffusion coefficient which in simulations of a three dimensional system can be measured through the mean squared displacement of fluid particles as $\langle x^2(t) - x(0)\rangle = 6Dt$.

Table 3.4 Schmidt and Prandtl numbers of some liquids [1–3]

Liquid	$\rho \times 10^{-3}$	$\eta \times 10^{3}$	$D \times 10^{9}$	$C_P \times 10^{-3}$	κ	Pr	Sc $\times 10^{-3}$
Methanol	0.786	0.553	4.44	2.53	0.202	9.84	0.158
Carbon tetachloride	1.584	0.903	4.33	0.850	0.099	13.6	0.132
Benzene	0.874	0.602	4.62	1.74	0.1411	10.78	0.149
Nitrobenzene	1.198	1.840	1.9	1.4	0.16	10.48	0.808
Water	0.997	0.894	2.23	4.18	0.606	6.877	0.402

Table 3.4 presents Sc and Pr numbers of several liquids. Liquids have larger Sc and Pr in comparison with gases. According to data of references [1, 137–139], Sc and Pr numbers in gases (noble gas or others) are around one at atmospheric pressure and room temperature.

The Prandtl and Schmidt numbers are different functions of model parameters and therefore, they can be set to different values independently. The transport properties of the DPD fluid have been investigated in several studies [102, 140] and here, we have formulated heat conductivity of the system. We summarize these equation as:

$$\begin{aligned} \kappa &= 0.18\rho^2 c_v^2 \kappa_0 + \frac{3.78}{\sigma^2} c_v \left(k_B T^2\right)^2 \\ \eta &= 0.0154 \frac{\sigma^2 \rho^2}{k_B T} \\ D &= \frac{3.78 T}{\rho} \end{aligned} \tag{3.30}$$

and therefore:

$$\begin{aligned} \mathrm{Pr} &\propto \frac{\sigma^2 \rho^4}{0.18\sigma^2\rho^2 c_v \kappa_0 T + 3.78 k_B T^3} \\ \mathrm{Sc} &\propto 0.0154 \frac{\sigma^2 \rho^2}{k_B T^2} \end{aligned} \tag{3.31}$$

For instance, if $\sigma = 10.0$ and $c_v = 1000$, then the Schmidt number is 427 and the Prandtl number is 7.00 which is similar to those of water. Furthermore, if the average temperature decreases to 0.4, Prandtl and Schmidt numbers are 6.43 and 21.71 respectively. In the case of a large noise amplitude $\sigma = 10.0$ or equivalently the friction coefficient, the viscosity is large and finding the average values would generally require more statics making the simulation more expensive. Also, a low average temperature $\bar{T} = 0.4$ may significantly limit the strength of temperature gradient implemented in the system since the minimum temperature can be close to zero and some particles may freeze. With the parameters introduced at the beginning of the chapter, the behavior of a simulated fluid is similar to a real fluid even though the dimensionless numbers may not be exactly the same.

Table 3.5 Transport coefficients in SI units for some relevant liquids at room condition together with the corresponding Prandtl and Schmidt numbers.

model	η	D	Sc	Pr
$a^T q^E$	1.51	0.06	8.67	2.02
$a^T q^{RE}$	1.52	0.06	8.79	2.05
$a^c q^E$	1.51	0.06	8.58	2.02
$a^c q^{RE}$	1.53	0.06	8.64	2.05
$a = 0, q^E$	1.26	0.07	6.39	1.68
$a = 0, q^{RE}$	1.25	0.06	7.23	1.68

Table 3.5 presents Pr and Sc numbers of different DPD models discussed here. Since the order of magnitude of dimensionless numbers is important, all of the presented models behave in a similar way.

3.6 Summary

In this chapter, heat transfer in DPDe using simple velocity-Verlet algorithm was studied. Energy is conserved on the order of machine precision. The model was validated by testing the consistency of all parts of energy (internal, potential and kinetic), by verifying the equality of two temperatures ($T_K = T_I$), and by RDF.

A thermal gradient was imposed by adding/removing a fixed amount of heat within two layers using periodic boundary conditions. The temperature gradient affects particle density such that at the highest temperature, the density has the lowest value.

Using Fourier's law for thermal conduction, the thermal conduction coefficient at different heat fluxes has been quantified and verified to be nearly a constant. Furthermore, κ shows to be a cubic function of temperature and density.

According to equation (3.1), κ_0^E and κ_0^{RE} values can be set such that these models are comparable (note that κ_0^E and κ_0^{RE} appear just in the conduction term). There is almost no difference between q^E and q^{RE} models except that q^E is more stable such that it can sustain a higher heat rate and q^{RE} has a simpler formulation which reduces the computational time.

In the case when the conservative force is a function of temperature, the system is more compressible and is closer to an ideal fluid. The system with a^T model in comparison to a^c model can have a larger maximum heat rate.

Chapter 4

Thermophoretic Janus Colloid

The study of thermophoretic self-propelled colloids has received a great attention in the last several years [39, 43, 44]. In spite of this, the number of interesting questions regarding the behavior of thermophoretic particles remain unanswered in general and the best approach to perform simulations is still to be determined [38, 45, 47].

Here a 2D Janus colloid is simulated by a multi-beads model, where all interactions are represented by dissipative particle dynamics with energy conservation. First we study thermodynamics properties of a Janus colloid in section 4.2. We find that the temperature profile around the colloid generates an unbalanced pressure and repulsive force which propel the particle. Other properties of the system, such as temperature and density profiles, are also considered. In section 4.3, we investigate the influence of boundary conditions (slip and no-slip) at the interface colloid-fluids on the propulsive velocity for two cases of ideal and non-ideal fluid. Also, we consider the effect of conservative force on propulsion. Thermophoretic quantities (thermal diffusion factor and Soret coefficient) are discussed in section 4.6. In the last section, we discuss different possibilities to vary the Peclet number. In particular, a new conservative interaction is introduced such that the Peclet number can be increased up to 50 times in comparison to the original model.

4.1 Simulation of Janus Colloid

As explained in chapter 3, all considered implementations of the DPDe model ($a^T q^E, a^T q^{RE}, a^c q^E$ and $a^c q^{RE}$) show similar results. Since, q^E appears to be more stable than q^{RE} and a^c represents a non-ideal fluid better, we use $a^c q^E$ further. We simulate a 2D Janus particle in a simple fluid modeled with $N_c = 400$ particles at the perimeter of a circle with a radius $R = 4.0$ (see figure 4.1). Density of fluid is $\rho = 5.0$. The box size is $25.0 r_c \times 25.0 r_c$ where $r_c = 1$ is the cutoff radius of fluid-fluid interaction. The average temperature of fluid is $\bar{T} = 0.64$.

In chapter 3, temperature gradient is implemented with a heat flux but here it is done by fixing the temperature, such that the Janus particle consists of two parts: one half at the temperature $T_c = 0.45$ and the other one maintains at the temperature $T_h = 0.83$. Inside of the Janus particle there is a fluid with the same average properties as the outside fluid, in order to keep pressure balance on the two sides of the colloid. All of the interaction coefficients between inside and outside fluids are set to zero since the colloid shields them from each other. Periodic boundary conditions are used at the box boundaries and bounce-back or specular reflection at the fluid particles at the colloid surface is implemented. Whenever the boundary conditions at the colloid are set directly to bounce back or specular, dissipative and random coefficients between fluid and colloid particles are set to zero $\sigma_{ij} = \gamma_{ij} = 0.0$, and otherwise they are adjusted to other system parameters according to appendix B. Other parameters for interactions are set as follows: conservative force $a_{ff} = 39.0 k_B T / r_c$ where ff denotes fluid-fluid interaction, random force coefficient $\sigma_{ff} = 3.0$. Heat conduction coefficient for all interactions is $\kappa_0^{ff,fc,cc} = 0.001$. The heat capacity at the constant volume is $c_v = 200.0$.

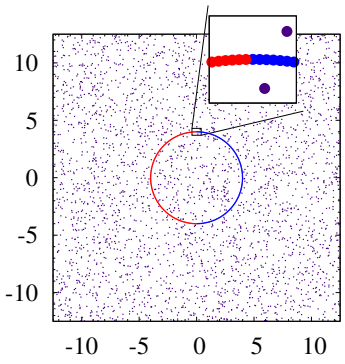

Fig. 4.1 Schematic diagram of the immersed Janus particle in simple fluid. Inside of the colloid there are fluid particles in order to keep pressure balance between inside and outside of Janus particle. After reaching a hydrostatic balance, inside particles are fixed. Janus colloid is shown by two colors. Colloid particles with same color are kept at the same temperature.

The colloid and fluid particles interact within the cutoff radius $r_c = 1.0$ applied, for dissipative, random forces and heat conduction. On the other hand, close to the wall within the range of the conservative interaction between fluid and colloid, there are might be only a few fluid particles and then, the heat exchange and dissipation in this region would be negligible. Therefore, a smaller cutoff radius for the conservative force of colloid-fluid is used, such that $r_c^{'} = 0.25$.

4.2 Thermodynamic Properties

Figure 4.2a presents the temperature profile with streamlines in lab frame (colloid is fixed). It reveals that fluid particles near the colloid have same temperature as the colloid. The largest temperature gradients are therefore at the poles. The temperature profile shows a plane symmetry at $y = 0$. Far from the colloid surface, the flow velocity (in colloid frame) is constant and equal to the propulsive velocity that a free colloid (lab frame) would then have in the opposite direction.

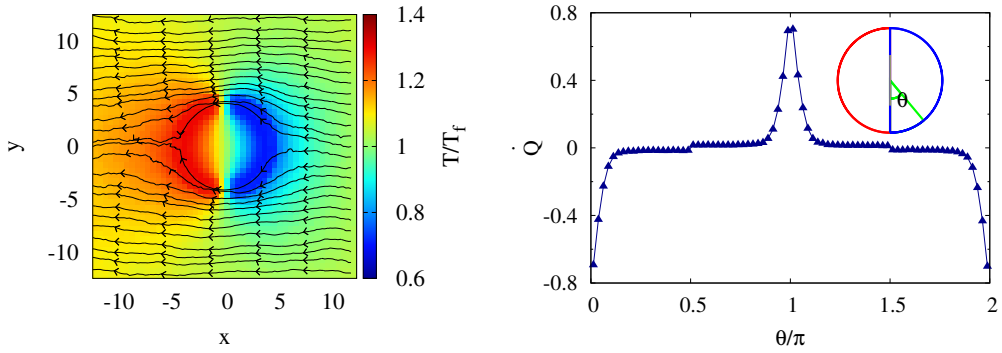

(a) (b)

Fig. 4.2 (a) Streamlines of the flow and temperature profile for the steady state with a fixed temperature at the hot $T_{hot}/\bar{T} = 1.3$ and cold caps $T_{cold}/\bar{T} = 0.7$. (b) The heat exchange around the colloid. The largest and smallest heat exchange happen at the poles since the largest temperature gradient is there. The cold (hot) cap is represented by θ from 0 to π (π to 2π).

Experimentally, one half of the colloid is heated while cooling is done by fluid far from the colloid surface; however, the largest temperature gradient still appears at the poles [10, 43]. Here, cooling and heating are done at the colloid surface such that the average temperature of the system is constant. Figure 4.2b presents the heat exchange rate around the colloid with a polar representation. Points at $x = 0.0, y = -4.0$ and $x = 0.0, y = 4.0$ correspond to $\theta = 0$ and $\theta = \pi$, respectively. Similar to figure 4.2b, the amount of heat rate that fluid receives at the hot cap is equal to the heat rate that fluid particles give away at the cold part. As a consequence, the average temperature of the system does not change significantly. The largest heat exchange occurs at the poles because of the largest temperature gradient, there.

Figure 4.3 shows the temperature profile of fluid around the colloid at different distances for two cases: (a) $\kappa_0^{ff} = 0.001$ and (b) $\kappa_0^{ff} = 0.1$. Conduction coefficient between fluid particles κ_0^{ff} controls the amount of heat transfer thorough the fluid. In the case of the smallest heat conduction, the temperature profile becomes nearly constant at a distance larger

than the particle radius which does not occur for the case with larger heat conduction. This means that the larger heat conduction within the fluid produces a smoother temperature profile in the vicinity of colloid. On the other hand, the temperature of fluid with a larger heat conduction in the vicinity of the colloid is not same as that of colloid, such that temperature in the vicinity of hot (cold) caps is smaller (larger) than the temperature at the colloid. Thus, it implements a smaller temperature gradient within the fluid.

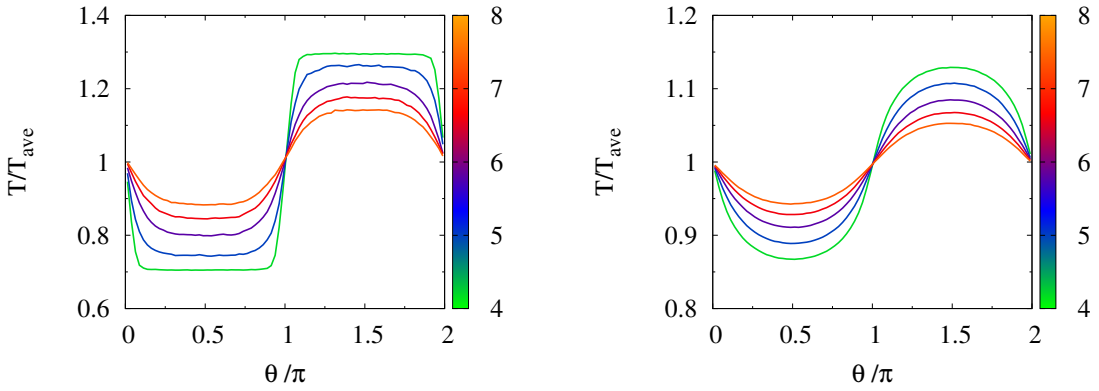

Fig. 4.3 The temperature profile as a function of the angle and distance for the cases (a) $\kappa_0^{ff} = 0.001$ and (b) $\kappa_0^{ff} = 0.1$.

Figure 4.4 shows fluid temperature distribution along an axis perpendicular to the colloid surface and starting from the middle points of the hot and cold cap as a function of distance from the colloid surface. The temperature in the cold part (hot) increases (decreases) smoothly without any local extremum and reach the average fluid temperature which is similar to that in experiments [43].

Fluid pressure is measured through the trace of the local Virial stress τ:

$$P = -\frac{1}{d}\mathrm{tr}(\tau) \tag{4.1}$$

where d is represents the dimension of the system and the local Virial stress is given by:

$$\tau_{ij} = \frac{1}{A}\sum_{k\in A}\left(m^{(k)}(v_i^{(k)} - \bar{v}_i)(v_j^{(k)} - \bar{v}_j) + \sum_{l\in A}\frac{1}{2}(x_i^{(k)} - x_i^{(l)})f_j^{(lk)}\right) \tag{4.2}$$

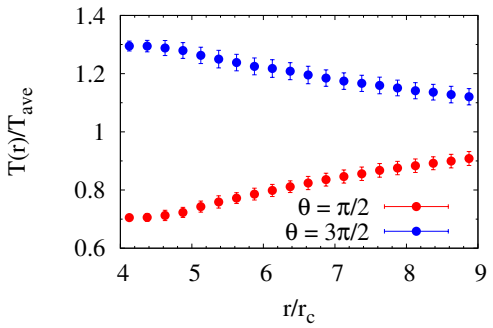

Fig. 4.4 The normalized temperature as a function of the radial distance for axes with angles $\pi/2$ and $3\pi/2$. The temperature linearly increases (decreases) at the cold (hot) sides.

where k and l are particles in the domain with area A, $m^{(k)}$ is the mass of particle k, i refers to the $i-$th component, v and x represent the velocity and position of particle, respectively. $\bar{v}_i$ is the $i-$th component of the average velocity of particles in the area A, and $f_i^{(kl)}$ is the $i-$th component of the force applied on particle k by particle l. The density and pressure profiles as a function of the angle around the colloid (within the area between two concentric circles which are centered at the center of colloid with radii $4.5r_c$ and $5r_c$) are presented in figure 4.5. At the cold and hot parts, pressure and density are constant but at the poles there are large gradients. The thermophoretic effect (propulsive velocity) can be quantified by a pressure gradient, which can only appear in the relation to an external gradient, as is the case at the colloid poles.

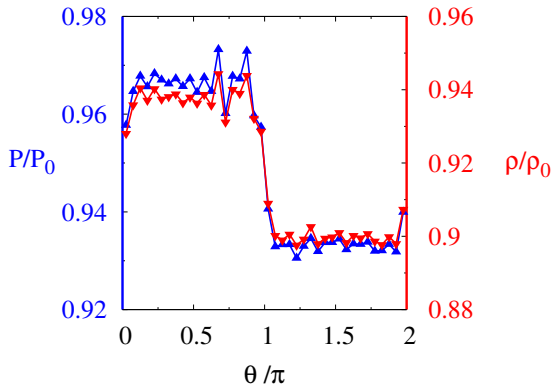

Fig. 4.5 Pressure and density profiles around the colloid. Density at the cold part is larger and consequently the pressure is larger. Density and pressure at cold and hot part are almost constant. Pressure gradient is strongest at the poles.

Figure 4.6a shows density fluctuations as a function of distance from the center of colloid. At places far from the colloid fluid, density is equal to the average density. The largest density and pressure gradient are in the range of $4.0r_c - 5.0r_c$. As a consequence, stress and pressure profiles (see figure 4.6) also show a layering structure close to the colloid surface. Layering structure in the vicinity of the wall is usual behavior in DPD and it is similar to hard-core particles near a hard wall in molecular dynamics simulations [141].

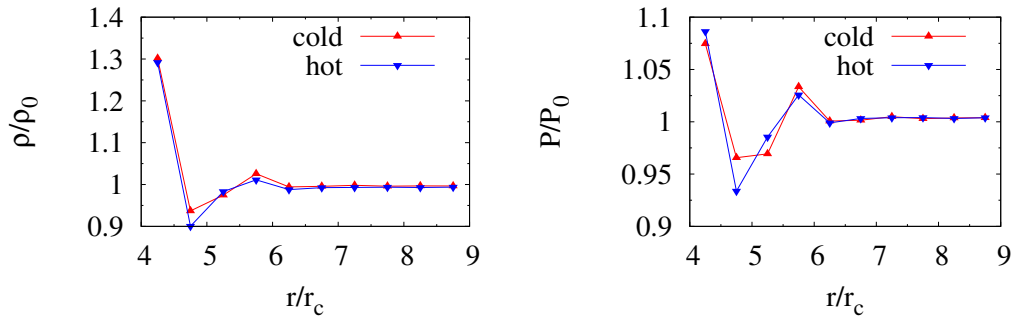

(a) (b)

Fig. 4.6 (a) Density and (b) pressure profiles. Near the colloid surface pressure and density are larger at cold part than at the hot part and far from the colloid they reach a constant value.

Normal stresses are measured the lab frame using equation (4.2) and are shown in figures 4.7a and 4.7b. Similar to pressure and density profiles, they show a layering behavior. Also, there are gradients at the poles (comparison between blue and red) and a stronger variation close to the colloid surface ($r/r_c < 6$). Far from the colloid surface, τ_{xx} and τ_{yy} reach the same constant bulk value but in the vicinity of the colloid, they have different values. Figure 4.8 shows a schematic structure of a system with fluid and a flat wall. Close to the wall along the x axis, there are no particles due to the strong conservative repulsion and symmetry of the system in y direction is broken, causing the gap between two components of stress τ_{xx} and τ_{yy} close to the colloid surface.

Shear stress at different distances as a function of θ is shown in figure 4.9. Shear stress fluctuates around zero except at the poles next to the colloid which shows a larger peak. Peaks at the poles have the same magnitude and opposite sign which means that the total shear stress is zero in every layer. Here, peaks reveal a correlation between the two directions.

4.3 Propulsive Velocity

As already mentioned, propulsive velocity of a free Janus colloid has same magnitude as the flow produced by a fixed Janus colloid far from its surface ($r > 2R$) but in the opposite

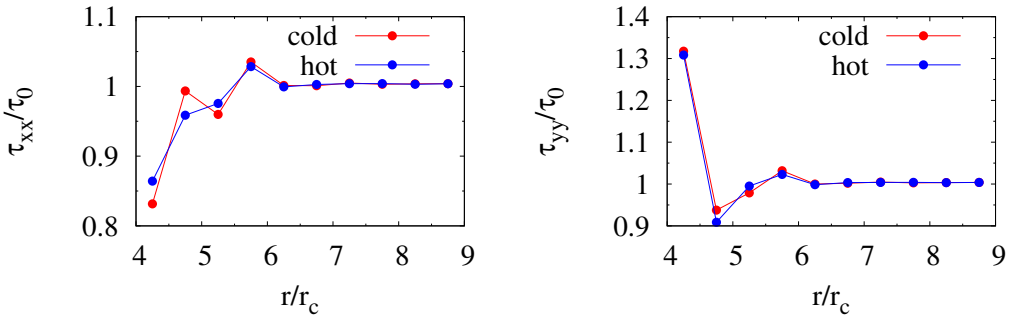

(a) (b)

Fig. 4.7 Normal shear stress profiles at $\pi/2$ and $3\pi/2$ (a) τ_{xx} and (b) τ_{yy}. Close to the colloid surface τ_{xx} and τ_{yy}, have different values but far from it they are equal.

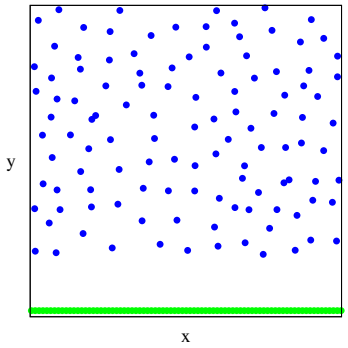

Fig. 4.8 Schematic drawing of the fluid particles (blue) close to the wall (green particles).

direction in the lab frame (colloid is fixed). Figure 4.10 shows propulsive velocity as a function of the strength of the conservative force coefficient between fluid particles and the colloid for two cases: (a) non-ideal fluid $a_{ff} = 39.0 k_B T/r_c$ and (b) ideal fluid $a_{ff} = 0.0$ for bounce back and specular reflection. In the case of non-ideal fluid by increasing the strength of conservative force between fluid and colloid particle from zero to $a_{fc}/k_B T = 39.0$, propulsive velocity increases. This is because the pressure gradient increases due to a larger strength of conservative interaction between colloid and fluid. In fact, the first term (kinetic term) in equation (4.2) does not play a role in thermophoretic pressure gradient since at the hot part, thermal velocity is larger, but there are fewer particles. On the other hand, in the cold part the second term (virial term) is larger, since there are more particles and a pressure gradient appears at the poles. Therefore, by increasing the strength of the conservative force a_{fc}, the pressure gradient becomes larger. For $a_{fc}/k_B T$ larger than 40.0, the average distance between fluid particles and colloid surface is larger than in the previous cases, such that the pressure gradient is not affected significantly by a_{fc}.

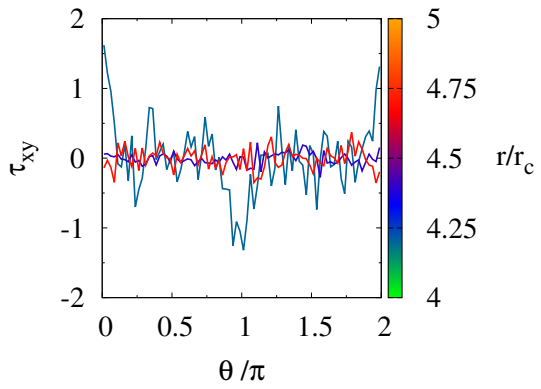

Fig. 4.9 Shear stress as a function of angle at various distances from the center of colloid. Close to the colloid at poles, there are peaks but they disappear at larger distances.

At low conservative forces, specular reflection shows a stronger propulsive velocity. Specular reflection does not affect tangential velocity near the colloid surface while bounce-back reflection retards tangential velocity at the surface. Thus, propulsive velocity is affected by a slip velocity near the colloid surface (the bounce-back reflection implements additional friction on colloid [142]). At high conservative force coefficients for fluid-colloid interaction, there is no difference between bounce-back and specular reflections since at strong conservative forces, fluid particles cannot reach the colloid surface and particle reflection is almost absent. If a_{fc}/k_BT is larger than 40.0 as in the case of non-ideal fluid, the propulsive velocity saturates.

Ideal fluid shows a more sophisticated behavior. If the conservative force coefficient between colloid and fluid particles is $a_{fc} = 0.0$, the second term in equation (4.2) is zero and there is no limitation on the density gradient. It implies a pressure balance between the cold and hot parts. On the other hand, due to particle reflections, there is an unbalanced force between the hot and cold parts of the colloid. According to the third law of motion, fluid feels the force and flow develops. When a_{fc} is non-zero but small, there is a limitation on the density gradient (colloid and fluid particles cannot be very close to each other due to repulsion). The virial part of pressure is negligible but of the hot part, the first term of pressure is stronger, so that there is an unbalanced pressure. Unbalance of pressure and force are acting against each other, so the direction of flow changes. By increasing a_{fc}, reflection vanishes and at the cold part density is larger, so that the virial part plays a decisive role and the sign of the pressure gradient changes. According to new balance the direction of flow changes again. Bounce-back and specular reflections show similar trends. In addition, at large a_{fc}, they have same saturation value, since the rate of reflection is zero. For $a_{fc} < 20$, the bounce back reflection provides a stronger repulsive velocity for a reason that is not clear

to us. In the presence of fluid-fluid conservative interactions, the colloid propels faster and for $a_{fc} > 50k_BT/r_c$, the propulsive velocity is larger by a factor close to 10.

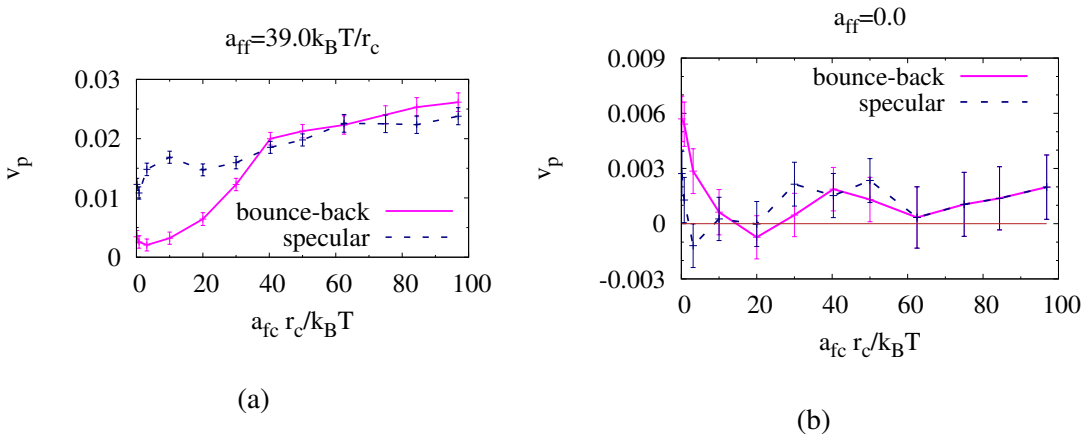

Fig. 4.10 Propulsive velocity for different interactions between colloid and fluid for two cases: (a) non-ideal fluid and (b) ideal fluid.

The fluid particles inside the colloid have fixed positions after an initial equilibration in which this fluid has reached a steady state. When the positions are fixed, inside fluid and colloid surface move together as a rigid body. In this case, the slip or no-slip boundary conditions are removed and the Lennard-Jones interaction (12-6 potential) replaces particle reflection (specular or bounce-back) in order to exclude penetration of the colloid by fluid particles:

$$U_{LJ}(r) = 4\varepsilon_{LJ}\left(\left(\frac{\sigma_{LJ}}{r_{ij}}\right)^{12} - \left(\frac{\sigma_{LJ}}{r_{ij}}\right)^{6}\right) + C_{LJ} \tag{4.3}$$

where the depth of the potential well is $\varepsilon_{LJ} = 5 \times 10^{-3}$ and the interaction length parameter is $\sigma_{LJ} = r_c^{'}/2^{1/6}$. The cut off radius of Lennard-Jones potential is $r_c^{'} = 0.25$ and only the repulsive part of Lenard-Jones is exerted. C_{LJ} is a shift equal to $4\varepsilon_{LJ}$ to avoid discontinuities in the energy at $r_c^{'}$. This form of Lenard-Jones is called Weeks–Chandler–Andersen potential.

In this case, the propulsive velocity as a function of conservative DPD interaction for two cases of ideal and non-ideal fluids is shown in figure 4.11, where the fluid interacts via Lenard-Jones potential with the colloid surface. The propulsive velocity is nearly constant as a function of the conservative force coefficient. Ostensibly, Lennard-Jones potential is much stronger than the normal DPD conservative interaction between colloid and fluid and therefore, the Lenard-Jones potential eliminates the effect of DPD conservative force (Lennard-Jones potential pushes fluid particles far enough from the colloid surface). The propulsive velocity in the case of non-ideal fluid is again much larger than for ideal fluid

since the interaction between fluid particles takes part in the pressure gradient through density gradient with the virial term in equation (4.2).

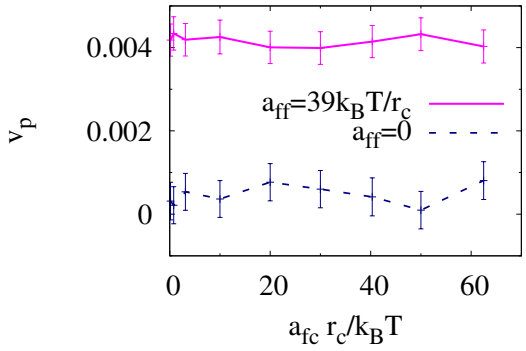

Fig. 4.11 Propulsive velocity as a function of DPD conservative interaction between colloid and fluid when colloid impenetrability is enforced by Lennard-Jones potential.

Now, in order to compare the velocity from the previous measurements for a fixed colloid, we perform simulations with a moving Janus colloid. In the case of non-ideal fluid ($a_{ff} = 39k_BT/r_c$), the velocity of free colloid as a function of time is presented in figure 4.12. The velocity is measured using instantaneous displacements and it fluctuates strongly with time (as expected from a diffusive motion), showing even a change in direction. The average value of the velocity still nicely agrees up to the statistical errors with the far field velocity for fixed colloid (see figure 4.11). Note that the lab frame and colloid frame are identified by xy and $x'y'$ respectively.

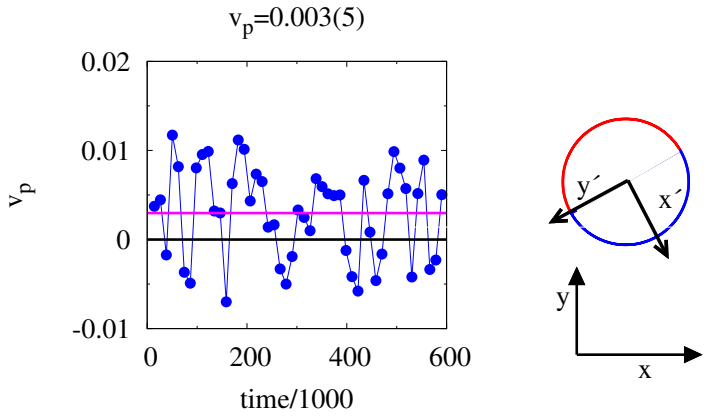

Fig. 4.12 Instantaneous velocity free colloid. The positive velocity shows that the colloid moves in the direction of polar axis. The Janus particle is a thermophobic particle.

Variation of the propulsive velocity with an applied temperature gradient is an important question. From the theory of thermophoresis [61], we know that the thermophoretic drift velocity of a colloid increases linearly with the magnitude of external temperature gradient, such that it is reasonable to approximate:

$$v_p = -D_T \nabla T \tag{4.4}$$

where D_T is the thermo-diffusion coefficient. The validity of above equation is illustrated in figure 4.13 where it is shown to be valid in a very large interval of applied ∇T (colloid size is fixed and ΔT changes), and only deviates at the very large $\Delta T = 0.2$. In the other words, D_T is constant as a function of temperature gradient in the system with $R = 4r_c$, when $\Delta T < 0.2$.

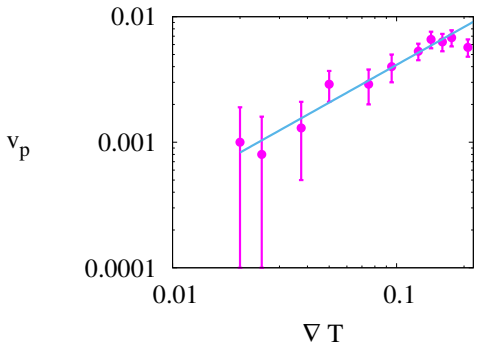

Fig. 4.13 Dependence of the propulsive velocity on the temperature gradient when $\bar{T} = 0.64$. The line corresponds to linear fit. A linear relation between the propulsive velocity and temperature gradient shows the range of validity of the applied model.

Note that the thermophoretic Janus particle with Lennard-Jones potential shows much smaller saturation of propulsive velocity in comparison to a colloid with the slip or no-slip boundary conditions at its surface due to a larger friction between colloid and fluid (non-zero dissipative or random force coefficients).

4.4 Rotational Dynamics

Investigation of the rotational diffusive behavior of the Janus colloid in the absence of a temperature gradient will serve as verification for the correctness of the DPDe modeled colloid, and will also be used later to characterize the time scale and activity of a Janus particle using the dimensionless Peclet number. The autocorrelation function of the orientation vector

decays exponentially with time according to theory [143]:

$$\langle \mathbf{u}(t).\mathbf{u}(0)\rangle = \exp(-2D_r t). \tag{4.5}$$

A unit vector $\mathbf{u}$ is the body-fixed vector (see inset in figure 4.14) and D_r is the rotational diffusion. A nice agreement with this decay reinsures the method and permits us to quantify the actual value of D_r.

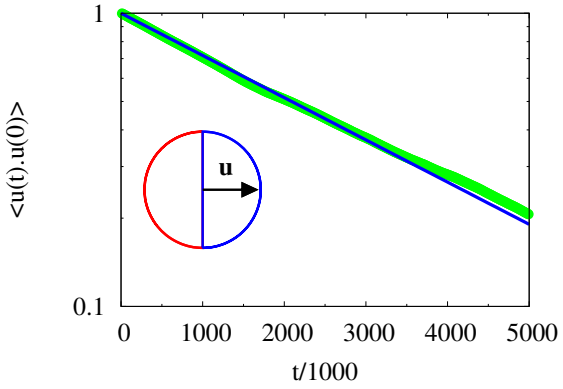

Fig. 4.14 Auto correlation function of the orientation vector. The green line represents simulation results and the black line refers to fit from equation 4.5. Inset shows orientation vector as the body-fixed vector.

4.4.1 Einstein Relation for Rotational diffusion in 2D

In order to find analytical expression for rotational diffusion, we consider a ring in the xy-plane of radius R that slowly rotates with a constant angular velocity Ω around z axis. The flow field in two dimensions is:

$$\vec{v} = [v_r, v_\theta] = [0, v_\theta(r)] \tag{4.6}$$

and due to the symmetry of the flow around z axis, the pressure will be of the form $P = P(\rho)$. Also, we consider a case with no external force $f_{ext} = 0$, and Stokes equation (equation 1.25) can be written as:

$$[\nabla^2 v]_\theta = 0 \tag{4.7}$$

This expression in cylindrical coordinates becomes:

$$r^2 v_\theta'' + r v_\theta' - v_\theta = 0 \tag{4.8}$$

where $v'_\theta = \frac{\mathrm{d}v_\theta}{\mathrm{d}r}$. By substituting a trial solution $v_\theta = r^b$ into above equation, we obtain that $b = \pm 1$ is a possible solution. Therefore, the flow field can be expressed as:

$$v_\theta(r) = C_1 r + \frac{C_2}{r}. \tag{4.9}$$

Boundary conditions determine C_1 and C_2. At infinity velocity is zero and in the vicinity of the ring, fluid rotates with the same velocity as the ring (no-slip boundary conditions):

$$\begin{aligned} r \to \infty \quad &: v_\theta \to 0 \\ r \to R \quad &: v_\theta \to R\Omega \end{aligned}$$

The final expression for the flow field produced by a rotating ring in the ring plane is:

$$v_\theta(\rho) = \frac{R^2\Omega}{r}. \tag{4.10}$$

This expression for the velocity allows us to calculate the relevant component of stress as:

$$\begin{aligned} \tau_{r\theta} &= -\eta r \frac{\partial}{\partial r}\left(\frac{v_\theta}{r}\right) \\ &= 2\eta \frac{R^2\Omega}{r^2} \end{aligned}$$

The tangential force on a ring element is equal to $\mathrm{d}F_\theta = \tau_{r\theta} R \mathrm{d}\theta$ and the torque on it is $\mathrm{d}F_\theta R$. The total torque on the ring is:

$$M_z = \int_0^{2\pi} 2\eta\Omega R^2 \mathrm{d}\theta = 4\pi\eta R^2\Omega \tag{4.11}$$

The rotational friction factor is defined by $M_z = f_r\Omega$ and the rotational diffusion coefficient can be calculated as $k_B T / f_r$. Therefore:

$$D_r = \frac{k_B T}{4\pi\eta R^2} \tag{4.12}$$

Figure 4.15 presents rotational diffusion for colloid rings of different sizes. Rotational diffusion strongly decreases with size. Equation (4.12) shows that rotational diffusion is proportional to R^{-2}. Fitting leads to $D_r = 0.006R^{-2}$ and the theoretical approach yields $D_r = 0.007R^{-2}$, such that the error is less than 13%. The error arises from the assumption of stick boundary conditions in theory, in contrast to the simulation where partial slip at the

colloid surface exists due to Lennard-Jones interaction.

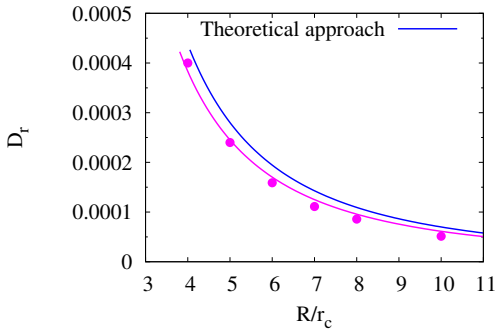

Fig. 4.15 Rotational diffusion of different size colloids. By increasing the size of colloid, D_r decreases.

The effect of temperature on the dynamic viscosity and rotational diffusion has been studied and is illustrated in figure 4.16. Note that, the dynamic viscosity is measured as outlined in section 3.5. Dynamic viscosity decays dramatically as a function of temperature and since rotational diffusion is proportional to the inverse of viscosity, D_r will increase.

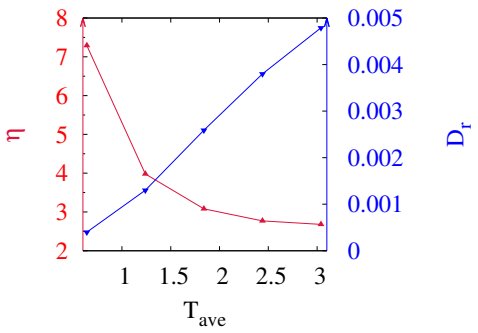

Fig. 4.16 Dynamic viscosity and rotational diffusion as a function of average temperature. Dynamic viscosity decays strongly as a function of temperature. Rotational diffusion is proportional to the temperature over viscosity, and therefore it increases.

4.5 Force Field in the Fluid and Total Force on Colloid

The force field in the direction of x' axis around the colloid is presented in figure 4.17a. Force has an opposite direction of the cold part and at the hot part, since the conservative force is repulsive. Figure 4.17b shows force in the propulsive direction (along x' axis) as a function

of distance for middle points of the hot and cold parts. Near the colloid surface, the force gradient is strong and changes from positive to negative values and vise versa. Far from the colloid surface, force decays to zero. The force field in the normal direction is shown in figure 4.17c and in order to illustrate it better, the force for middle points of hot and cold parts as functions of distance are shown in figure 4.17d. Since forces acting on the fluid are central, total force at every point next to the colloid is always in the polar direction at that point. Hence, forces along x' and y' directions are functions of $\sin\theta$ and $\cos\theta$ and when one of them is maximum, the other one is zero (see figures 4.17a and 4.17c). Similar to force in x' direction, force in y' direction reaches zero at points far from the colloid surface.

The fact that the positions of peaks in force fields (figure 4.17d, 4.17b) are different from peaks of the density profile (figure 4.6a), speculates that the force field behavior may not reflect density layering. It is remarkable that force field of a charged colloid in the electrolyte solution has exactly the same behavior [144].

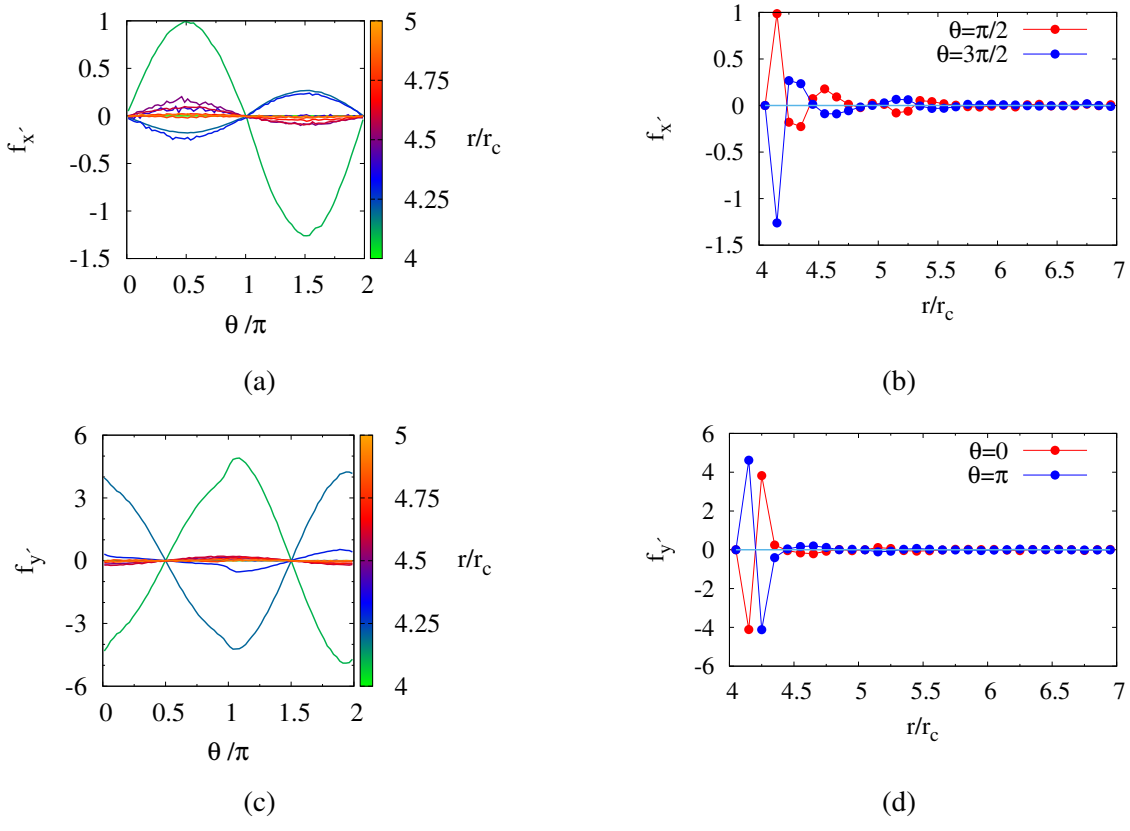

Fig. 4.17 Force profiles in the colloid frame $x' - y'$ as a function of the angle and distance (a and c) and as a function of the distance at $\theta = \pi/2$ and $\theta = 3\pi/2$ (b), and for two directions at $\theta = 0$ and $\theta = \pi$ (d).

4.6 Measuring Friction Factor and Thermal Diffusion Factor

In this section, we measure the friction factor γ_f of a colloid in a laminar external flow and the thermal diffusion factor. Simulation results show that total forces in two directions of x' and y' have fluctuations but on average they are zero. On the other hand, when the colloid moves with a constant velocity, it experiences two forces, thermophoretic force f_T and drag force f_D which are given by:

$$f_T = -\alpha_T k_B \nabla T \tag{4.13}$$

where α_T is thermal diffusion factor and:

$$f_D = \gamma_f v_p \tag{4.14}$$

where γ_f is the frictional coefficient from fluid. These two forces balance each other such that the total force on the colloid is zero $f_{tot} = 0$. This allows us to relate α_T and v_p as:

$$\alpha_T = \frac{\gamma_f v_p}{k_B \nabla T} \tag{4.15}$$

The friction factor γ_f is measured in isothermal simulations by exposing the colloid to an external uniform flow (see figure 4.18) from equation (4.14). Note that, the velocity field is similar to the case of thermophoretic Janus particle in section 4.3. The drag force is calculated by summing up all individual forces between the colloid particles and fluid particles.

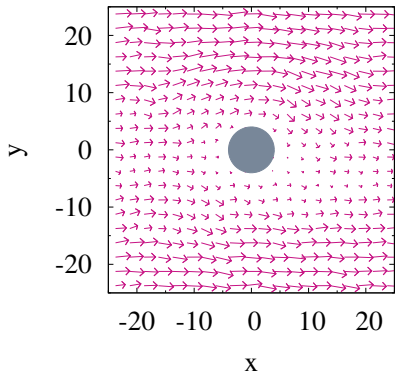

Fig. 4.18 Uniform flow around a fixed colloid for measuring the friction factor γ_f.

We assume that drag force (viscous force) on the colloid is proportional to the velocity far from the colloid surface v_0 through the friction coefficient $F_d = \gamma_f v_0$. The friction

coefficient is measured through the far field velocity, which is similar to the measurement of the propulsive velocity for thermophoretic colloid.

Figure 4.19 presents dependence of the thermal diffusion factor α_T and friction coefficient γ_f on different relevant parameters. In order to investigate the effect of smoothness or number of particles representing colloid N_c, all interaction coefficients are adjusted to the same values when the number of particles at the perimeter of colloid changes e.g. $N_c \kappa_0^{fc} = N_c' \kappa_0^{'fc}$. Note that here a colloid is assumed as a regular polygon where N_c is the number of edges or sides and the larger N_c represents a smoother shape. The number of particles representing the colloid does not have an effect on α_T and γ_f (figure 4.19a). Note that a larger number of particles on colloid N_c provides smoother surface of the colloid. As a matter of fact, the mass of the colloid is changed by the number of particles on its surface (particles employed to built the colloid). However, the mass of the fluid particles does not change either α_T or γ_f within the provided error bars (figure 4.19b). According to Navier–Stokes equations, the mass of fluid particle does not affect hydrodynamics in non inertial regime which means γ_f is constant.

The mesoscale heat conduction coefficient κ_0^{ff} controls the conductivity of the fluid directly. By increasing κ_0^{ff} the conductivity of the fluid increases. Nevertheless, figure 4.19c shows that α_T and γ_f are nearly constant as a function of κ_0^{ff} taking into account statistical errors.

The size of the colloid in the range of $4 < R/r_c < 8$ has a small effect on α_T and γ_f. In $3D$ for the spherical colloid, the friction coefficient from the Stokes' law is given by:

$$\gamma_f = 6\pi\eta R \tag{4.16}$$

Nevertheless, for a disk which moves in a plane, there is not a non-trivial steady-state solution of the Stokes equations around a disk which is known as Stokes' paradox and therefore, there is no an identified relation for the friction coefficient. Simulations show that, there is no clear relation between size and γ_f or α_T (see figure 4.19d) which may be due to the small range of sizes used or large error bars.

Figure 4.16 shows that dynamic viscosity decays dramatically as a function of temperature. Viscosity and friction force define resistive forces between layers of fluid. Therefore, the friction coefficient γ_f has a similar behavior (figure 4.19e). The thermal diffusion factor shows a strong decay as a function of temperature.

The viscosity of the fluid is controlled by the dissipative force coefficient γ or equivalently by the random force coefficient σ. The friction coefficient and viscosity are related [125], and therefore it's expected that γ_f will increase linearly with σ. The thermal diffusion factor does not show a monotonous behavior (see figure 4.19f).

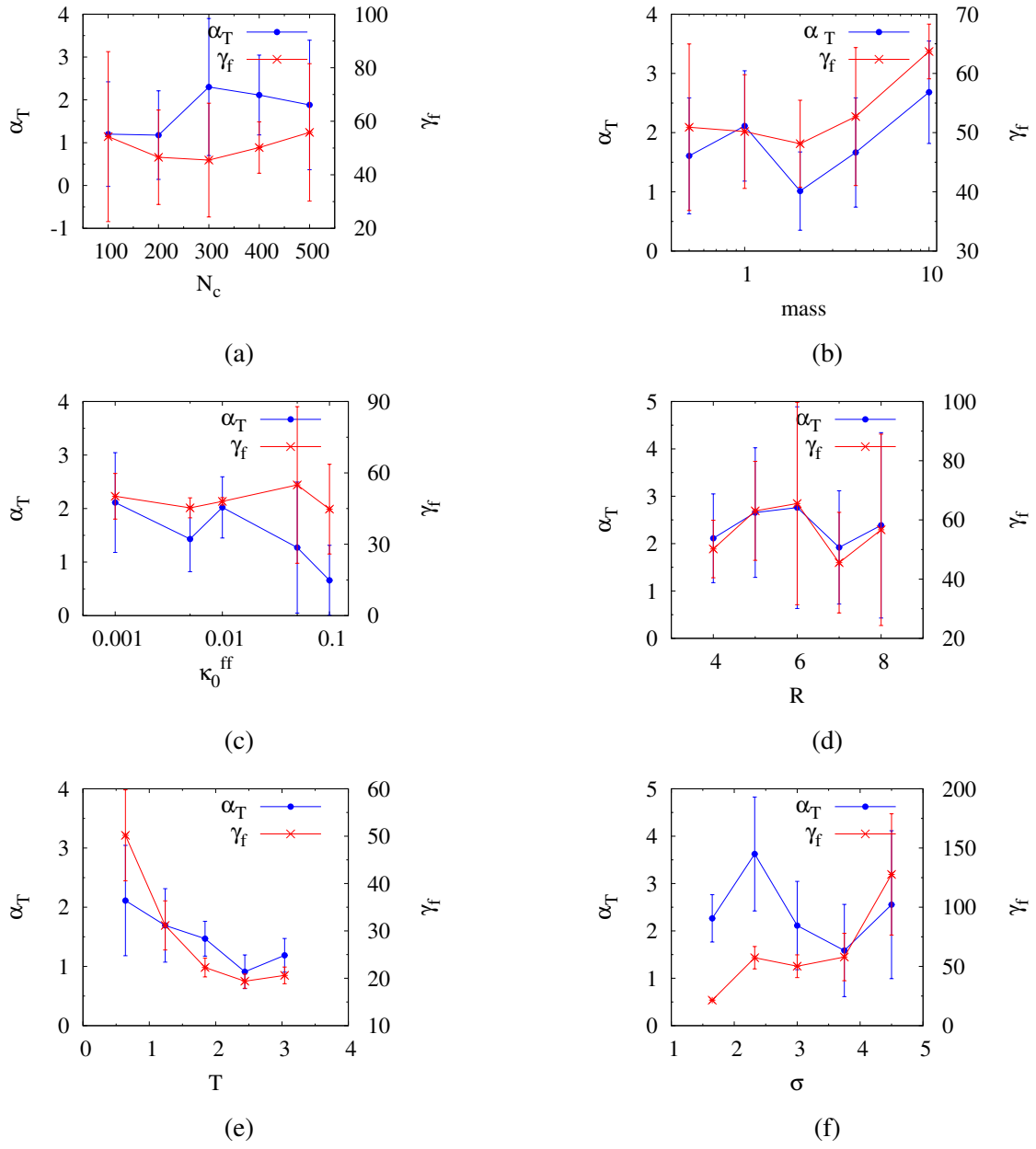

Fig. 4.19 Dependence of the thermal diffusion factor α_T and friction coefficient γ_f on (a) number of colloid particles at the colloid surface, (b) mass of the fluid particles, (c) conductivity coefficient of fluid, (d) colloid radius, (e) average temperature, (f) random force coefficient.

4.6.1 Soret Coefficient

Here, we calculate S_T using the thermal diffusion factor (α_T):

$$S_T = \alpha_T / T \tag{4.17}$$

where T is the temperature in real units. The thermal diffusion factor is $\alpha_T = 2.1$ in our reference system. Here, we have $S_T = 0.007$ at the room temperature. Experimental works report Soret coefficients on the order of $0.0001 - 100$ [43, 145–147].

The Soret coefficient has same behavior as α_T except when temperature changes. The Soret coefficient as a function of temperature is illustrated in figure 4.20 where it decreases strongly. Experimental results show that the dependence of Soret coefficient on temperature for different particle sizes and aqueous solutions can be different [60]. MPC simulations have reported same dependence of the Soret coefficient on temperature [148].

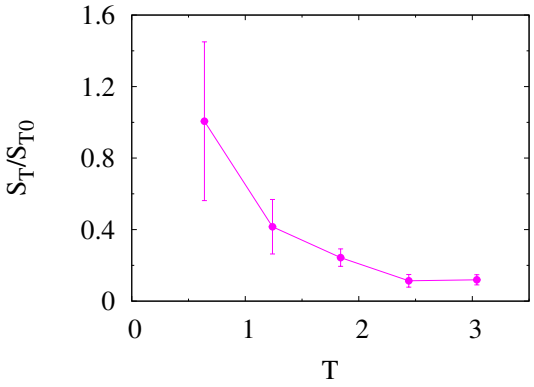

Fig. 4.20 Dependence of the Soret coefficient on temperature. Soret coefficient is calculated as $S_T = \alpha_T / T$ and $S_{T_0} = \alpha_{T_0} / T_0$ where $T_0 = 300K$ is equivalent to $T = 0.64$ in the simulation. Simulation results for dilute colloidal suspensions using MPC have reported the same behavior of the Soret coefficient as a function of temperature [148].

4.7 Effect of Simulation Parameters on the Peclet Number

In order to explore whenever the DPDe model leads to a swimmer with a Peclet number similar to those of the experimental systems, we study the Peclet number as a function of different parameters. Peclet number is defined as:

$$\mathrm{Pe} = \frac{v_p}{R D_r} \tag{4.18}$$

Effects of simulation parameters on Peclet number are presented in following tables.

Table 4.1 shows v_p and Peclet number as a function of the exponent s in the weight function, which affects fluid viscosity. A larger s results in a fluid with a smaller viscosity. However, the Peclet number is not affected by s, since rotational diffusion (see equation (4.12)) and propulsive velocity are inversely proportional to viscosity.

Table 4.1 Effect of s exponent on Peclet number.

s	η	γ	D_r	v_p	Pe
0.25	7.29	0.885	0.00038	0.004(1)	2.5(0.6)
0.5	3.74	0.844	0.00064	0.009(2)	3.5(0.8)
0.75	2.77	1.03	0.0012	0.009(2)	1.9(0.4)

Viscosity η is proportional to γ (σ) coefficient in dissipative force (random) directly. On the other hand, random force coefficient σ changes conductivity of the fluid. The total conductivity of the fluid consists of two parts and in a two dimensional system similar to the three dimensional system (see section 3.3.4) is given by:

$$\kappa = c_0 c_v \frac{k_B^2 T^2}{\sigma^2} + c_1 n^2 c_v^2 \kappa_0^{ff} \tag{4.19}$$

with:

$$c_1 = \pi \int_0^{r_c} \mathrm{d}h \left(\sqrt{1 - \frac{h^2}{r_c^2}} \right) \int_h^{r_c} \mathrm{d}r g(r) \omega_{HC}^2 r^2 \tag{4.20}$$

$$c_0 = \left(\pi \int_0^{r_c} \mathrm{d}r g(r) r^2 \omega^D(r) \right)^{-1} \tag{4.21}$$

where $g(r)$ is the radial distribution function. Since the temperature $\bar{T} = 0.64$ is low and density $\rho = 5$ is high, the first term can be neglected such that conductivity is almost constant. Therefore, the largest temperature gradient at poles does not change. Velocity and rotational diffusion coefficient are proportional to η^{-1} (see equations (4.15) and (4.12)) and therefore, the Peclet number is independent of viscosity (see table 4.2).

Table 4.2 Relation between σ and Peclect number.

σ	η	γ	D_r	v_p	Pe
4.5	15.7	1.93	0.00019	0.0019(4)	2.5(1.2)
3.0	7.29	0.885	0.00038	0.004(1)	2.5(0.6)
1.65	2.56	0.316	0.001	0.010(2)	2.5(0.2)

Conduction coefficients control the amount of heat transfer to (κ_0^{fc}) or through (κ_0^{ff}) the fluid. We vary the heat conduction within the fluid κ_0^{ff} by a factor 100, which leads to a smoother temperature profile and a weaker temperature gradient within the fluid in the vicinity of the colloid (a smaller temperature at hot part and a larger temperature at the cold part. See figure 4.3). In other words, high conductivity results in a weaker effective temperature gradient at the poles which decreases the propulsive velocity according to equation (4.4). On the other hand, the rotational diffusion is almost constant, so that the Peclet number decreases (see table 4.3).

Table 4.3 Fluid conductivity and Peclet number.

κ_0^{ff}	η	ΔT	$\dot{Q}$	D_r	v_p	Pe
0.001	7.29	0.077	1.00	0.00038	0.004(1)	2.5(0.6)
0.01	7.17	0.063	2.26	0.00038	0.0036(9)	2.4(0.6)
0.1	7.14	0.015	6.36	0.00035	0.0014(8)	1.00(0.6)

The role of the fluid-colloid conduction coefficient κ_0^{fc} is different, because a larger conductivity between fluid and colloid increases the temperature gradient, and therefore, propulsive velocity increases such that the Peclet number increases weakly (table 4.3).

Table 4.4 Effect of heat conduction at the interface of colloid on Peclet number.

κ_0^{fc}	η	ΔT	$\dot{Q}$	D_r	v_p	Pe
0.001	7.29	0.077	1.00	0.00038	0.004(1)	2.5(0.6)
0.01	7.29	0.080	7.85	0.00036	0.004(1)	2.8(0.7)
0.1	7.29	0.081	76.0	0.00034	0.005(1)	3.7(0.9)

The range of interactions within the fluid r_c^{ff} changes conductivity, viscosity and temperature gradient such that rotational diffusion and propulsive velocity decreases, while the Peclet number shows a weak enhancement (table 4.5).

Table 4.5 Cutoff radius of fluid interaction affects weakly the Peclet number

r_c^{ff}	η	γ	D_r	v_p	Pe
0.25	1.40	0.173	0.0025	0.009(1)	0.9(0.1)
0.50	1.01	0.125	0.0024	0.009(3)	0.9(0.1)
1.00	7.29	0.885	0.00038	0.004(1)	2.5(0.6)
1.50	34.9	4.31	0.00006	0.0008(7)	3.3(2.9)

By rescaling all of the length scales in the system, viscosity and conductivity do not change. If the temperature gradient is kept constant, the propulsive velocity according to the equation (4.4) is constant. Rotational diffusion decreases as the colloid size squared in 2D

which results in an increase of Peclet number. In case if rescaling number is larger than 1.5, the propulsive velocity is reduced. It seems that if ΔT is large the effect on the propulsive velocity might be reversed (table 4.6).

Table 4.6 The system size is scaled and the Peclet number increases

scale	η	γ	D_r	v_p	Pe
1.00	7.29	0.89	0.00038	0.004(1)	2.5(0.7)
1.25	7.47	0.92	0.00023	0.004(1)	3.5(0.9)
1.50	7.65	0.94	0.00015	0.004(1)	4.4(1.1)
1.75	7.93	0.98	0.000091	0.002(1)	3.1(1.3)
2.00	8.13	1.00	0.000086	0.001(2)	1.5(2.9)

A small interaction range between colloid and fluid particles r_c^{fc} decreases the heat gradient in the fluid, since fluid in the vicinity of the colloid can not attain the same temperature as the colloid. Note that, the cutoff radius of conservative force remains same as before $r_c^{'} = 0.25$. If cut-off radius is large enough ($r_c > 1.0$), the temperature of the fluid particles is close to the colloid temperature and ∇T increases leading to the propulsive velocity rising weakly. On the other hand, rotational diffusion within the statistical accuracy is constant (table 4.7). Therefore, the Peclet number becomes larger slowly, but computational cost increases.

Table 4.7 Cut off radius for the colloid and fluid interaction and Peclet number

r_c^{ff}	γ	D_r	v_p	Pe
0.25	57.4	0.00038	0.002(1)	1.2(0.7)
0.50	7.17	0.00033	0.001(1)	0.8(0.8)
1.00	0.88	0.00038	0.004(1)	2.5(0.7)
1.50	0.27	0.00042	0.005(1)	3.0(0.6)
2.00	0.17	0.00027	0.004(1)	3.7(0.9)

Peclet number as a function of the density of particles for the colloid representation N_c is constant within the statistical errors. Coefficients for the interactions ($\sigma_{LJ}, a_{fc}$and, κ_0^{fc}) are scaled according to the density of particles representing the colloid (table 4.8). In the other words, the smoothness of colloid in considered range does not affect on the Peclet number.

The mass of particles does not change the propulsive velocity and rotational diffusion, since physical properties of the system are not functions of the mass (see table 4.9).

Table 4.8 Density of particles representing the colloid does not change Peclet number

N_c	γ	D_r	v_p	Pe
100	3.54	0.00038	0.002(1)	1.2(0.7)
200	1.76	0.00038	0.002(1)	1.2(0.7)
300	1.17	0.00038	0.004(1)	2.5(0.7)
400	0.88	0.00038	0.004(1)	2.5(0.7)
500	0.704	0.00038	0.004(1)	2.5(0.7)

Table 4.9 Particle mass does not affect the Peclet number

mass	η	D_r	v_p	Pe
0.5	7.18	0.00037	0.003(1)	2.0(0.7)
1.0	7.29	0.00038	0.005(1)	3.3(0.7)
2.0	7.58	0.00042	0.002(1)	1.2(0.6)
4.0	7.91	0.00033	0.003(1)	2.3(0.8)
10.0	8.44	0.00035	0.004(1)	2.5(0.7)

In order to investigate the effect of colloid size more accurately, the propulsive velocity, rotational diffusion and Peclet number are rewritten as follows:

$$v_p = \frac{\alpha_T \Delta T}{R\gamma_f} \tag{4.22a}$$

$$D_r = \frac{k_B T}{4\pi\eta R^2} \tag{4.22b}$$

$$Pe = 4\pi\eta R \frac{\Delta k_B T}{k_B T} \frac{\alpha_T}{\gamma_f} \tag{4.22c}$$

A larger colloid under the same temperature gradient has same propulsive velocity which means that α_T/γ_f is constant as a function of size. Furthermore, figure 4.19d shows that α_T and γ_f as functions of size approximately are constant. Conclusively, the Peclet number should rise linearly with size. Figure 4.21 presents Peclet number as a function of colloid radius (see equation 4.22c). In the case of same temperature difference ($\Delta T = const$,), the Peclet number is nearly constant as a function of size. Larger particles require a larger ΔT and similar to figure 4.13, at large temperature differences, propulsive velocity may decreases which here corresponds to the case with $R > 8r_c$.

In pursuance for a higher Peclet number, we also investigate the effect of the average temperature $\bar{T}$ of system. We will do this following to conceptual approaches. One is by fixing the temperature gradient, and varying only $\bar{T}$, while in the other approach we fix the ratio $\Delta T/\bar{T}$.

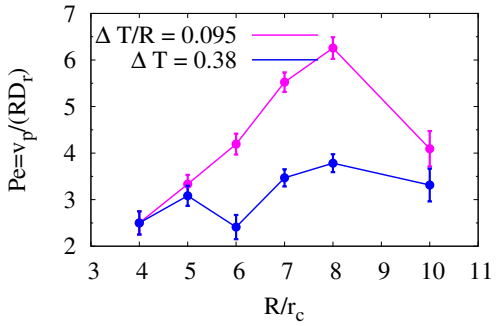

Fig. 4.21 Peclet number of the Janus particle as a function of the size of colloid for the same temperature gradient $\nabla T = \text{const}$ and same temperature difference $\Delta T = \text{const}$. In order to yield the same temperature gradient, the larger colloid requires larger ΔT. If ΔT is constant, the Peclet number increases with the size of colloid.

The same temperature gradient at different average temperatures results in same propulsive velocity as shown in figure 4.22a. This is consistent with the results shown in figure 4.19e, where both α_T and γ_f showed similar dependence on $\bar{T}$, such that they almost cancel each other. On the other hand, since rotational diffusion grows significantly (see figure 4.16), Peclet number decreases as a function of temperature. The results are shown in figure 4.22a.

The dependence of the Peclet number on average temperature with $\Delta T/\bar{T} = 0.6$ is shown in figure 4.22b. The propulsive velocity increases. On the other hand, it is weaker than the decay of rotational diffusion, and therefore, the Peclet number decreases.

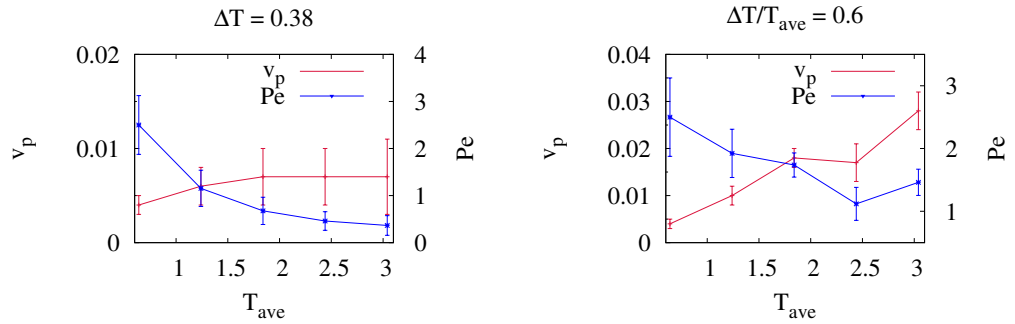

(a) (b)

Fig. 4.22 Propulsive velocity and Peclet number as a function of temperature when (a) $\Delta T = \text{const}$. and (b) $\Delta T/\bar{T} = \text{const}$..

4.8 Effect of Attraction Interaction between Colloid and Fluid

For all simulation results so far, we have used a purely repulsive interaction for the conservative force leading to thermophobic behavior. In contrast, even though most of the experiments report a thermophobic behavior, depending on the nature of colloid-solvent interaction, thermophilic phenomenon is also observed [145, 149]. Employing MPC, a different mesoscopic simulation approach [61] results in the variation of colloid-fluid attraction from purely repulsive to attractive, changing the behavior of colloid from thermophilic to thermophobic.

The question now is whether a different approach could be used in our DPDe model in order to obtain both thermophobic and thermophilic behavior, as well as an enhanced propulsive velocity. A direct solution for this problem is to include a longer range attraction and shorter repulsion interaction. Likewise the repulsive interaction, the attractive part should also be soft to retain the advantages of the DPD method. On the other hand, at short particle separations, the repulsive interaction should be strong enough, relative to the attractive one, to prevent the particle density from becoming too high. We use a cubic spline function as the weight function for conservative force:

$$\omega(r,r_c)=\begin{cases}1-\frac{3}{2}\left(\frac{2r}{r_c}\right)^2+\frac{3}{4}\left(\frac{2r}{r_c}\right)^3, & 0\leq\frac{2r}{r_c}<1\\ \frac{1}{4}\left[1-\left(\frac{2r}{r_c}\right)\right]^3, & 1\leq\frac{2r}{r_c}<2\\ 0, & 2\leq\frac{2r}{r_c}\end{cases} \tag{4.23}$$

In fact, a combination of two cubic functions is used for the conservative potential whose relative weight is controlled by A_0 and B_0 which are prefactors of the repulsive and attractive parts of the conservative potential, respectively [150, 151]:

$$U(r)=a_{ij}\left(A_0\omega_1(r,r_{c_1})-B_0\omega_2(r,r_{c_2})\right) \tag{4.24}$$

where a_{ij} regulates the overall strength of the potential and corresponding conservative force is given by equation (2.3). Figure 4.23 presents a comparison of the potential and force for two cutoff radii of the repulsive part of the interaction r_{c_1}. By decreasing r_{c_1}, maximum (minimum) of force increases (decreases) and the attraction part becomes stronger.

Here, we choose $A_0=2, B_0=1.05$ and $a_{fc}=6$. Note that, since the interaction at the long ranges is attractive, fluid particles are found in the vicinity of the wall and the cutoff

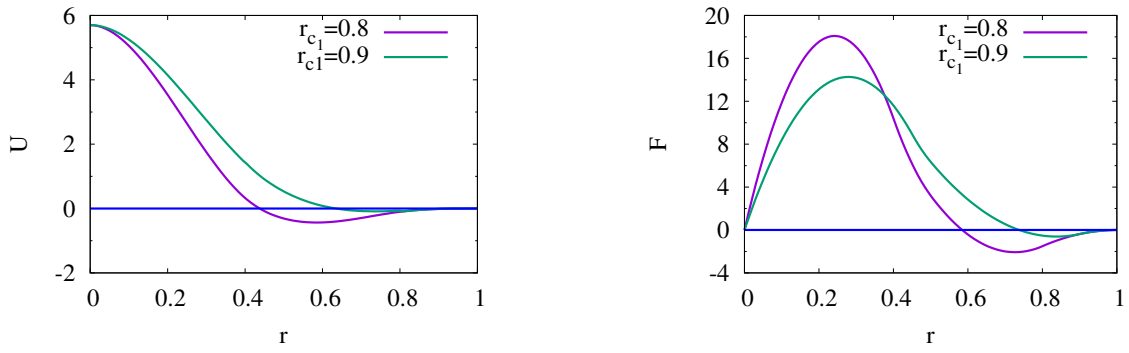

(a) (b)

Fig. 4.23 Potential (a) and conservative force (b) with cubic spline weight function in equation (4.24) where $A = 2, B = 1.05$ and $a_{ij} = 6$.

radius of conservative force and dissipative, random and heat conduction can be the same. Therefore, we introduce one cutoff radius $r_c = 1$ for all interactions. We use the weight function described in the equation (4.23) for fluid-colloid interaction and define r_{c_1} as a constant number for two different average temperatures. This case corresponds to thermophobic colloid with Pe $= 4$ where:

$$r_{c_1} = \begin{cases} 0.8r_c & \text{if fluid particles interact with } \textbf{cold} \text{ part of Janus colloid} \\ r_c & \text{if fluid particles interact with } \textbf{hot} \text{ part of Janus colloid} \end{cases}$$

while if:

$$r_{c_1} = \begin{cases} 0.8r_c & \text{if fluid particles interact with } \textbf{hot} \text{ part of Janus colloid} \\ r_c & \text{if fluid particles interact with } \textbf{cold} \text{ part of Janus colloid} \end{cases}$$

we observe thermophilic colloid with Pe $= 4$.

On the other hand, Peclet number for thermophoretic Janus particle in simple water is reported on order of 100 [43, 152] but the largest Peclet number we obtained is reported 6.5 for $R = 8r_c$ in the last section. We search, therefore, for a further modification of the previous scheme that results in much higher propelling velocities. The weight function is introduced according to the equation (4.23) for fluid-colloid interaction, where r_{c_1} is a

function of average temperature of two particles T_{ij}:

$$r_{c_1}(T_{ij}) = \begin{cases} 0.8r_c & T_{ij} < T_{min}, \\ \left[1 - \dfrac{0.2}{\Delta T}\left(T_{max} - T_{ij}\right)\right] r_c & T_{min} < T_{ij} < T_{max}, \\ r_c & T_{max} < T_{ij} \end{cases} \tag{4.25}$$

Here, $\Delta T = T_{max} - T_{min}$ with $T_{max} = T_h$ and $T_{min} = T_c$. Note that, the function within the range $T_{min} < T_{ij} < T_{max}$ is chosen such that the function of $r_{ij}(T_{ij})$ is continuous. The cutoff radius of the repulsive part is a function of temperature in a way that at lower (larger) temperature leads to a weaker (stronger repulsion). Here, we observed thermophobic behavior with large Peclet number Pe $= 100$ for $R = 8r_c$. If the cutoff radius for smaller (larger) temperature is weaker (stronger), fluid particles are attracted more to the hot part and we observe a thermophilic behavior:

$$r_{c_1}(T_{ij}) = \begin{cases} r_c & T_{ij} < T_{min}, \\ \left(\dfrac{-0.2}{\Delta T} T_{ij} + 1 - \dfrac{0.2}{\Delta T} 0.83\right) r_c & T_{min} < T_{ij} < T_{max}, \\ 0.8r_c & T_{max} < T_{ij} \end{cases} \tag{4.26}$$

In this case Peclet number is also on the order of 100.

In the other words, repulsion-attraction interaction between fluid and colloid provides thermophobic or thermophilic behavior and conservative force gradient (as a result of temperature gradient) propels the particle faster than the constant one. Note that, if the strength of attraction is chosen stronger ($B_0 > 1.05, A_0 = 2$ or $B_0 = 1.05, A_0 < 2$) or the cutoff radius of the repulsion part becomes larger $r_{c_1} > 0.8$, we observe small clusters of fluid particles which is similar to those in references [150, 151].

4.9 Summary

In this chapter, we have discussed the simulation of a 2D Janus particle represented by beads model. In the first part, we have considered a fixed colloid with bounce-back or specular reflection of fluid particles at its boundary. If the strength of the conservative force is weak in case of non-ideal fluids bounce-back reflection shows a weaker propulsive velocity, because it decreases the slip velocity at the colloid surface which is the main reason for propulsion. In other words, an additional friction is imposed by the fluid due to no-slip boundary conditions.

Ideal fluid shows a more complicated behavior since there is a competition between different contributions to the pressure. Slip and no-slip boundary conditions have the same trend but no-slip (bounce-back) in the case of weak interaction between fluid and colloid shows a larger propulsive velocity and the reason was not identified. If the interaction is strong enough, particle reflection is almost absent and both types of reflection lead to the same propulsive velocity within the statistical accuracy. We found that there is layering of density and pressure in the vicinity of colloid surface, which is similar to hard-core particles near a hard wall [141], hence, it is related to the conservative force. Note that the force field around a charged colloid in electrolyte solution is similar. In contrast to density, pressure and force field, the temperature does not show a local extremum and decreases at the hot part and increases at the cold part. This behavior of temperature profile is confirmed in experiments [43]. This is important, since the pressure and density layering is known to be a defect at the DPD method but it does not appear in temperature profile.

Tables of section 4.7 and figure 4.21 present thermophobic behavior for different method parameters with a final saturation value for Peclet number of 6.5 in the case of purely repulsive interaction. Attraction-repulsion interactions result in both the thermophobic and thermophilic behavior. Furthermore, if the conservative force gradient adds to this interaction, Janus particle propels with a large Peclet number $\mathrm{Pe} = 100$ which is the case in experiments.

Note that, in order to investigate the effect of size, we increase the size of simulation box to two times larger and we observe same thermodynamic profiles and same rotational dynamics.

Chapter 5

Binary Mixture

Thermophoresis of colloids has been subject of investigation in several studies. For example, the flow pattern around a spherical Janus particle in self-generated temperature field depending on surface properties of Janus has been investigated theoretically by Bickel et al. [153]. Besides spherical Janus particles, other shapes such as cylindrical and dumbbell shapes were investigated experimentally [154, 155] and with simulations [47, 119]. Propulsion of various types of thermophoretic dimers and the self-assembly of dimers were explored in simulation by Wagner and Ripoll [47].

A particularly interesting case is when a Janus colloid immersed in binary mixture near a critical point. Binary mixture is a type of chemical combination of two species A and B, which may exhibit interesting features. For instance, the phase behavior of binary mixtures is much more complex than that of a simple fluid. Here, we are considering two phases: mixed and demixed states. Figure 5.1 shows the phase diagram for water–2,6-lutidine as an example of a binary mixture. Insets in figure 5.1 show the binary mixture under a microscope in the (i) mixed and (ii) demixed phases but close to the critical concentration and temperature.

If a hot Janus colloid is immersed in binary mixture whose temperature is below the critical temperature but close to it, the temperature of the hot cap and fluid near it can reach a temperature above the critical point. Therefore, fluid in the vicinity of the hot cap is demixed (see figure 5.2). In this situation, the Janus colloid might propel faster than it does in a simple fluid [42, 156] due to the presence of the two fluids at different sides of the colloid, together with the corresponding interface. This system has been investigated theoretically [62, 157] but so far no simulations are available due to several difficulties. These include the simulation of large particles in long times, the ability to represent phase separation of a binary mixture and imposing temperature gradients at the same time. In particular, the application

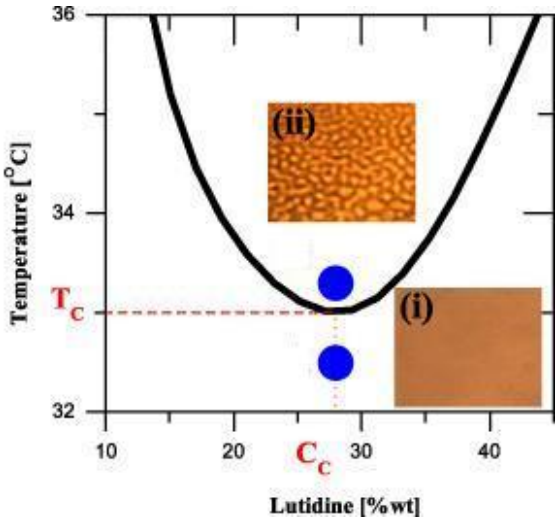

Fig. 5.1 A schematic phase diagram for water–2,6-lutidine. The insets are pictures of mixed (i) and the demixed (ii) phases at the critical concentration. Figure from reference [42] ©IOP Publishing. Reproduced with permission. All rights reserved.

of temperature gradients requires energy conservation in the system. Dissipative particle dynamics with energy conservation is therefore an ideal method to study this problem.

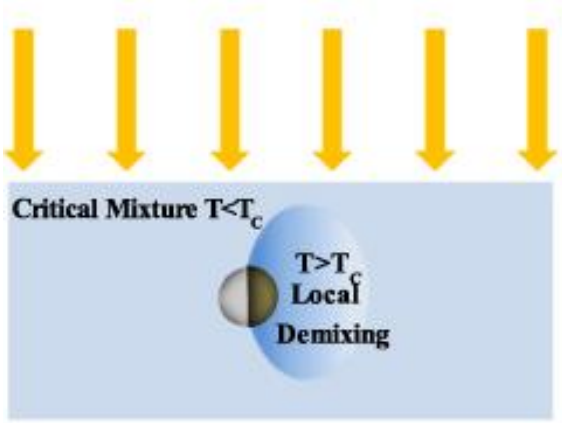

Fig. 5.2 An active Brownian micro-swimmers in a critical binary mixture. Figure from reference [42] ©IOP Publishing. Reproduced with permission. All rights reserved.

In this chapter, properties of a binary mixture near critical point, surface tension and the stability of a drop in flow and at a wall are studied. These enable us to investigate the behavior of a Janus colloid immersed in a binary mixture in the following chapter.

5.1 Model Implementation

One of the mechanisms which can be employed to model a binary fluid with mixed and demixed phases is to consider a difference in the interaction potentials between particles of the same fluid type and unlike ones. In this work, we consider a symmetric binary mixture modeled by DPDe such that the same size and interaction are assumed between similar species, but different interactions are imposed for unlike ones, i.e:

$$U_{\mathrm{AA}} = U_{\mathrm{BB}} \neq U_{\mathrm{AB}} \tag{5.1}$$

where U_{XY} corresponds to a potential between species X and Y. First, we consider the conservative force $\mathbf{F}^C$ with a weight function in equation (2.12). In order to implement equation (5.1), conservative force coefficients a_{ij} are chosen as $a_{\mathrm{AA}} = a_{\mathrm{BB}} \neq a_{\mathrm{AB}}$. Other coefficients remain the same. In this chapter, all simulations are two dimensional and employ total density $\rho_{tot} = 5.0$. The conservative force coefficient for similar species $a_{\mathrm{AA}} = a_{\mathrm{BB}} = 25.0$ in the original DPD.

5.2 Critical Point

The stronger the repulsive interaction between unlike particles, in comparison to the interaction between similar particles, the more probable is to obtain a demixed phase or immiscible mixture. In this section, we present the simulation results of mixed and demixed phases by changing repulsive interactions between different species in comparison to the similar ones.

Note that, the parameter a_{ij} from equation (2.11), controls the repulsion between particles. By increasing a_{ij} of dissimilar species step-by-step, a demixed phase appears at different a_{ij} values for various temperatures.

Equivalent to concentration in figure 5.1, we introduce number fraction φ of each spices where $\varphi_A = N_A/(N_A + N_B)$ and $\varphi_B = N_B/(N_A + N_B)$ and N_A and N_B are number of particles of type A and B respectively.

5.2.1 Analysis of Phase Transition

First we consider an equimolar case $\varphi_A = \varphi_B$. In order to quantify the phase transition, we use the probability distribution of local density of one species (for instance A) to determine the mixed and demixed phases. Such a histogram is obtained by dividing the simulation box into small bins in which the density is calculates. In the mixed phase (homogeneous phase. See figures 5.3b.), the histogram corresponds to a very sharp Gaussian distribution function

(see figure 5.3a):

$$\psi(x|\sigma_{var},\bar{x}^2) = \frac{1}{2\pi\sigma_{var}^2}\exp^{-\frac{(x-\bar{x})^2}{2\sigma_{var}^2}} \tag{5.2}$$

where $\bar{x}$ is the mean or expectation of the distribution, σ_{var} is the standard deviation (or σ_{var}^2 is the variance).

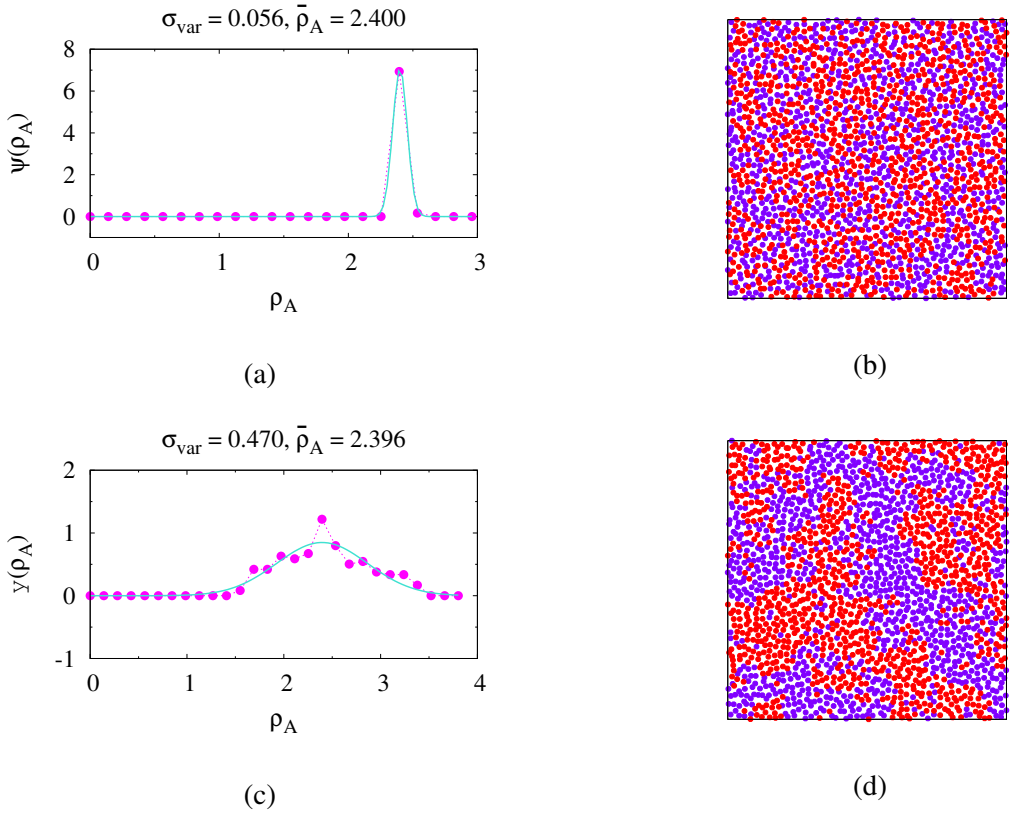

Fig. 5.3 (a) Gaussian distribution function fitted to the measured density distribution and (b) Snapshots of the system for $a_{AB} = 25.0$. (c) Gaussian distribution function fitted to the measured density distribution and (d) Snapshots of the system for $a_{AB} = 26.2$. The average temperature $\bar{T} = 0.45$ and number fraction $\varphi_A = \varphi_B$.

Similar to the demixed phase, in the case of clearly demixed phase with the sharp boundary between two species, two peaks appear: one peak appears at zero density (in the bins without selected type A) and the other one at the average density (in the bins occupied with A particles). Between these two states (completely mixed and demixed with the sharp boundary), spinodal structure forms in the system (see figure 5.3d). The corresponding Gaussian distribution changes from a symmetric bimodal distribution to the normal distribution with a

larger standard deviation σ_{var} than that for the mixed and demixed states (see figure 5.3c).

In case of $\varphi_A < \varphi_B$, the phase transition can be discerned better by the mean value of the Gaussian distribution function since it changes in larger range than variance σ_{var}. At the mixed phase, the mean value is $\bar{\rho}_A = \varphi_A/(\varphi_A + \varphi_B)\bar{\rho}$. For $\varphi_A < \varphi_B$ at the demixed phase, most of the bins do not contain type A and the peak appears at $\rho = 0.0$. Figure 5.4 presents the case with $\varphi_A = 0.25\varphi_B$. Figures 5.4a and 5.4b show the demixed phase with $\bar{\rho_A} = 0.2, \bar{\rho} = 1.0$. Similar to the previous case $\varphi_A = \varphi_B$, at the demixed phase, the histogram for $\varphi_A < \varphi_B$ is a symmetric bimodal distribution, but the second peak at $\rho = \bar{\rho}$ is much smaller than the peak at $\rho = 0$ and so it is not detectable in the figure.

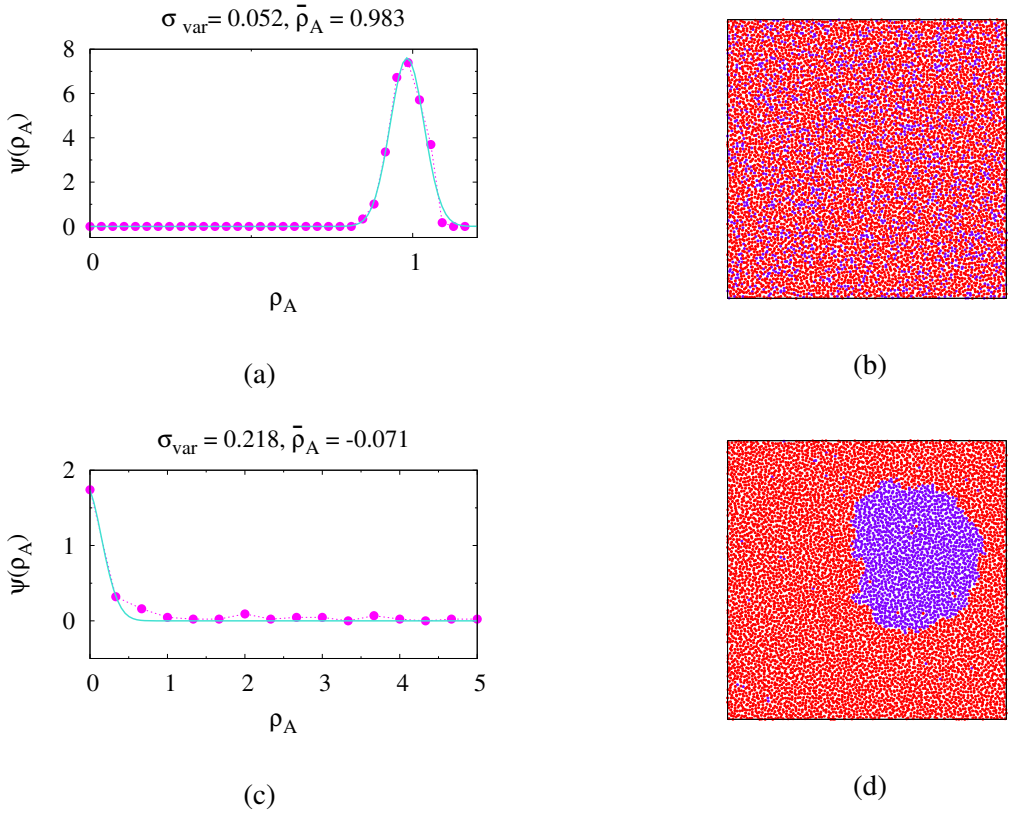

Fig. 5.4 Gaussian distribution function fitted to the measured density distribution for (a) $a_{\mathrm{AB}} = 25.0$ and (c) $a_{\mathrm{AB}} = 26.2$ at $\bar{T} = 0.45$ and $\varphi_A = 0.25\varphi_B$. Snapshots of the system are shown in (b) and (d) for $a_{\mathrm{AB}} = 25$ and $a_{\mathrm{AB}} = 26.2$, respectively.

The critical conservative force coefficient a_{AB} for three different temperatures and the two cases $\varphi_{\mathrm{A}} = \varphi_{\mathrm{B}}$ and $\varphi_{\mathrm{A}} = 0.25\varphi_{\mathrm{B}}$ are shown in figures 5.5a and 5.5b, respectively. The phase transition is a function of number fraction φ and temperature. For instance, a critical

temperature of $T_c = 0.45$, such that the binary mixture is phase separated below it and mixed above it, is achieved at $a_{AB} = 26.2$ for $\varphi_A = \varphi_B$ while $a_{AB} = 27$ for $\varphi_A = 0.25\varphi_B$.

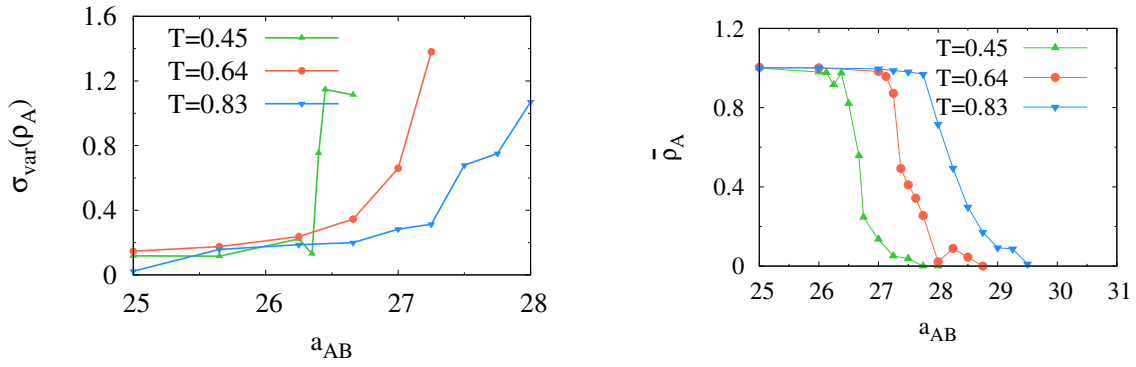

(a) (b)

Fig. 5.5 Variance σ_{var} and mean values of the density distribution function $\bar{\rho}_A$ as a function of a_{AB} for number fraction (a) $\varphi_A = \varphi_B$ and (b) $\varphi_A = 0.25\varphi_B$ at three values of the temperature.

5.3 Surface Tension

A molecule in the bulk of fluid feels attractive forces due to interactions with other molecules. Since it is surrounded isotropically, the total force fluctuates but it is zero on average. Nevertheless, a fluid particle at a surface feels an unbalanced force which affects the shape of a fluid surface and leads to surface tension [158]. Surface tension is generally defined in terms of energy or force. In terms of force, surface tension α is the force per length, which is required to keep the shape of the surface constant. In terms of energy, the surface tension is defined through the variation of energy of the system when the fluid area changes form A_1 to A_2 corresponding to a change ΔA. The variation of energy is equal to the work is done by the total force from particles in the bulk minus the work by particles at surface Δw, so that:

$$\alpha = \frac{\Delta w}{\Delta A} \tag{5.3}$$

5.3.1 Young–Laplace Equation in 2D

In the simulated system where phase separation is obtained, we can measure surface tension using the Young–Laplace equation in 2D. Let us consider a drop of one fluid type in the pool of the other fluid, as also shown in figure 5.4d. The pressure inside the drop is P_{in} and in the

bulk fluid is P_{out}. In order to increase the size of a drop from having a radius R to $R+\mathrm{d}R$, the work needed to be done is equal to:

$$\mathrm{d}w = \alpha \mathrm{d}A - \Delta P \mathrm{d}V \tag{5.4}$$

where dA and dV are area and volume variation corresponding to the variation of radius dR which in two dimensional system are given by $\mathrm{d}A = 2\pi \mathrm{d}R$ and $\mathrm{d}V = 2\pi R \mathrm{d}R$. In the thermodynamic equilibrium, $\mathrm{d}w = 0.0$ and for and therefore, in 2D surface tension α is given by:

$$\alpha = R\Delta P. \tag{5.5}$$

Figure 5.6 shows pressure and density in the presence of a drop as a function of distance from the center of the drop in the system for $\bar{T} = 0.45$ and $a_{AB} = 1.2a_{AA}$. The radius of the drop is measured by density profile as a function of the center of drop i.e. in side the drop density is constant and outside of it is zero (see figure 5.6a). Besides the difference in total pressure between inside and outside is measured (see figure 5.6b) and therefore the surface tension is calculated and in this case $\alpha = 2.53$. For $a_{AB} = 1.08a_{AA}$, surface tension is very low and due to large errors, it is very difficult to obtain the value. However, we would like to work with a system close to the critical point with some temperature variations, so we target $a_{AB} = 1.08a_{AA}$.

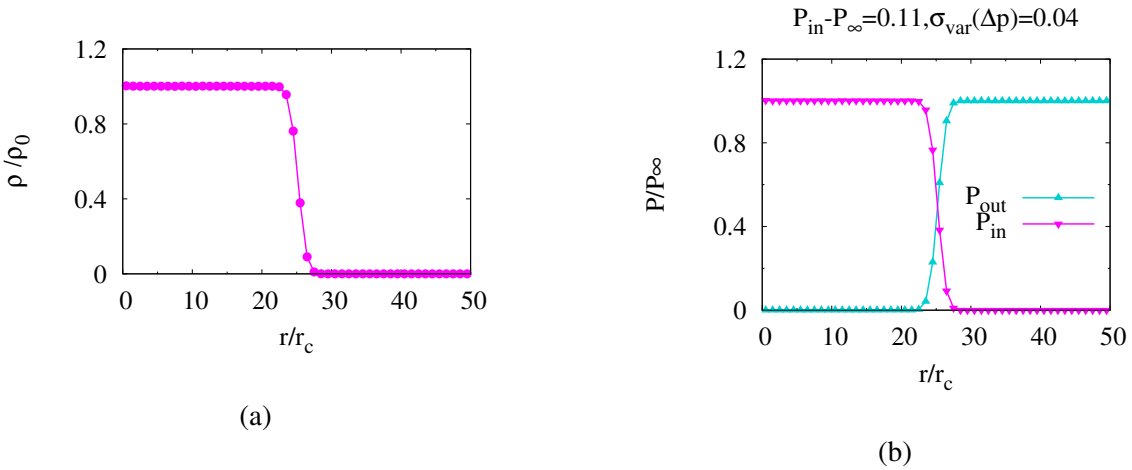

Fig. 5.6 (a) Density and (b) pressure profiles as a function of distance from the center of the drop

The stability of a drop

We test the stability of a drop in channel flow for a binary mixture with a temperature lower than the critical temperature (in order to form a drop in the channel). Thus, in the simulation box, there are two species at the temperature lower than the critical temperature $T < T_C$. Periodic boundary conditions are assumed along x-axis while in the y-direction two walls at $y = 50r_c$ and $y = -50r_c$ are placed. At the beginning the walls do not move, such that a drop is allowed to be formed in the middle of the channel as illustrated in figure 5.7a. Afterwards, the upper wall at $y = 50$ moves to the right with a velocity $v = 0.1$ and lower wall moves to the left with $v = -0.1$. Since the surface tension is very small, the drop breaks into many small drops (see figure 5.7b). Note that wall velocity is a desirable propulsive velocity of a Janus particle in a binary mixture to reach high Peclet number in experiments.

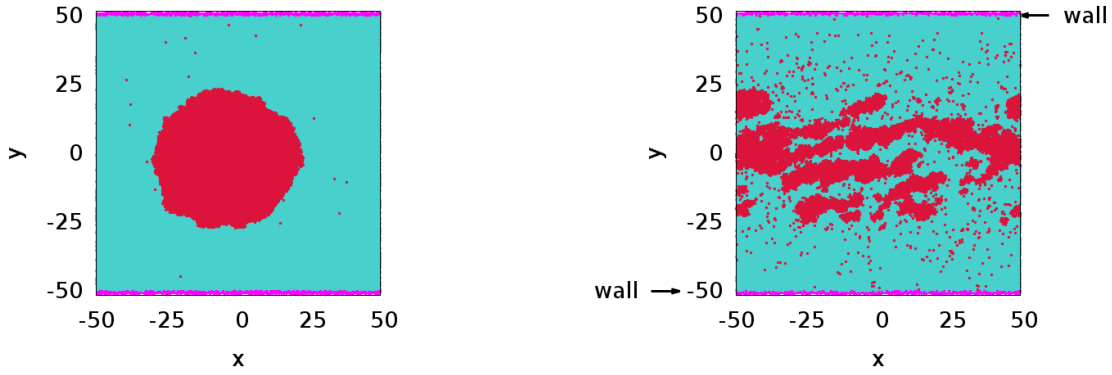

(a) (b)

Fig. 5.7 Steady drop profile in the periodic channel in the x direction (a) when there is no flow and (b) under shear flow.

5.3.2 Effect of Attraction Interaction of Fluid-Fluid

In order to have a more stable drop with a larger surface tension, the weight function for interactions is modified according to equation (4.23). The cubic spline function is useful to simulate a more realistic behavior of a drop and coexistence of two phases [150, 151]. This type of weight function allows us to control easily the magnitude of repulsion or attraction. At the same time, the location of the transition point from repulsion to attraction is simply adjustable. Here binary mixture is modeled by a different transition point for two spices in comparison to the same types (instead of the strength of interactions a_{ij}).

Simulations of a binary mixture with this weight function assume the total cutoff of $r_c = 1.0$, the force strength between all species $a_{\mathrm{AA}} = a_{\mathrm{BB}} = a_{\mathrm{AB}} = 6.0$, and the strength of repulsion and attraction $A_0 = 2$ and $B_0 = 1.05$, respectively. Cutoff for the repulsion part which also defines the range of attraction, is a piecewise-defined function of temperature $r_{ij}(T_{ij})$ that is continuous:
for particles of same type:

$$r_{c_1}(T_{ij}) = \begin{cases} 0.8r_c & T_{ij} < T_{min} \\ \left[1 - 0.2\left(\dfrac{T_{ij} - \bar{T}}{T_{min} - \bar{T}}\right)\right] r_c & T_{min} < T_{ij} < \bar{T}, \\ \left[1 + 0.2\left(\dfrac{T_{ij} - \bar{T}}{\bar{T} - T_{max}}\right)\right] r_c & \bar{T} < T_{ij} < T_{max}, \\ r_c & T_{max} < T_{ij} \end{cases} \tag{5.6}$$

while for particles of different type:

$$r_{c_1}(T_{ij}) = \begin{cases} r_c & T_{ij} < T_{min}, \\ \left[1 - 0.2\left(\dfrac{T_{ij} - \bar{T}}{T_{min} - \bar{T}}\right)\right] r_c & T_{min} < T_{ij} < \bar{T}, \\ 0.8r_c & \bar{T} < T_{ij} \end{cases} \tag{5.7}$$

where we use $T_{max} = 0.83, T_{min} = 0.45$ and $\bar{T} = 0.5\,(T_{max} + T_{main})$. This implementation of interactions provides a similar phase diagram as in figure 5.1, so that at the temperature higher than the average temperature $\bar{T}$, binary mixture is demixed and mixed otherwise. For this model, the surface tension is much larger than that is in previous case. The surface tension can be changed by the strength of interaction between different fluid types a_{AB} without changing the critical point significantly. Note that in this case, the critical point is defined mainly by the value of r_{c1}. Figure 5.8 shows that surface tension for $a_{\mathrm{AB}} < 4$, increases fast with a_{AB}, while for $a_{\mathrm{AB}} > 4$, the surface tension increases much slower than in the range $a_{\mathrm{AB}} < 4$. Note that, surface tension is measured by equation 5.5.

Note that, as it is shown in figure 5.9, by increasing the number fraction of binary mixture the droplet size increases while surface tension is constant.

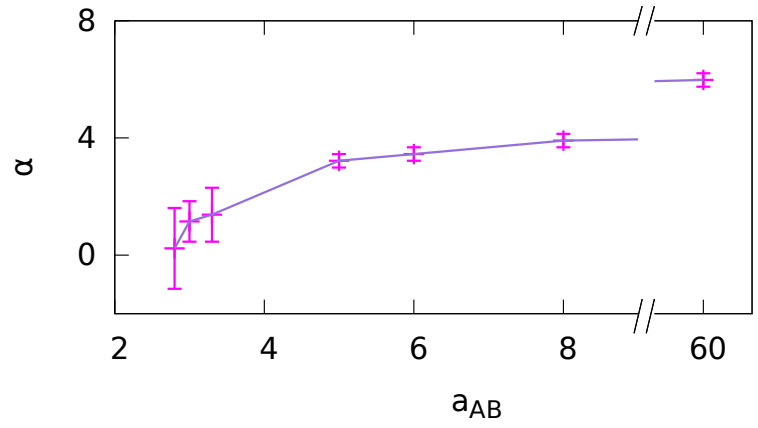

Fig. 5.8 Surface tension as a function of the strength of interaction force.

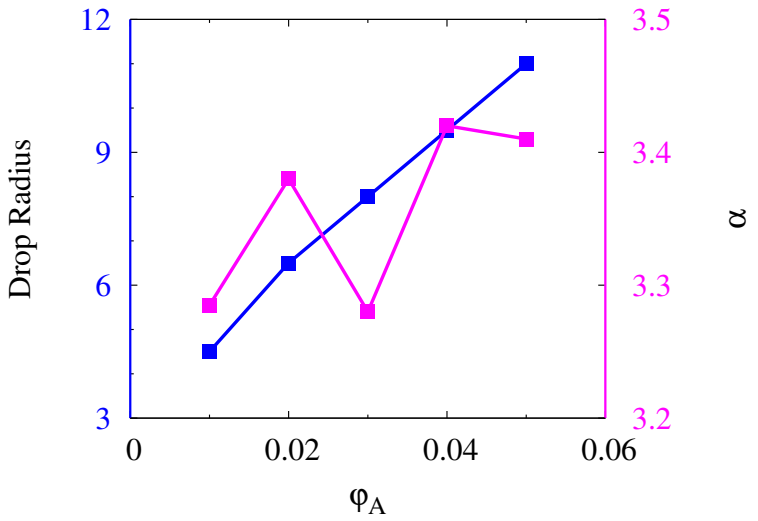

Fig. 5.9 The droplet size and surface tension as a function of number fraction φ_A.

The stability of a drop

As a result of large surface tension, the drop in flow is stable and deforms into an ellipsoidal shape (see figure 5.10). Similar to an issue for simple fluid in chapter 3, if the strength of attraction becomes large enough ($B_0 > 1.05$ for $A_0 = 2$ or $B_0 = 1.05$ for $A_0 < 2$) or the cutoff radius of the repulsion part becomes smaller $r_{c_1} < 0.8$, we observe whole system consists of many small drops similar to those in references [150, 151].

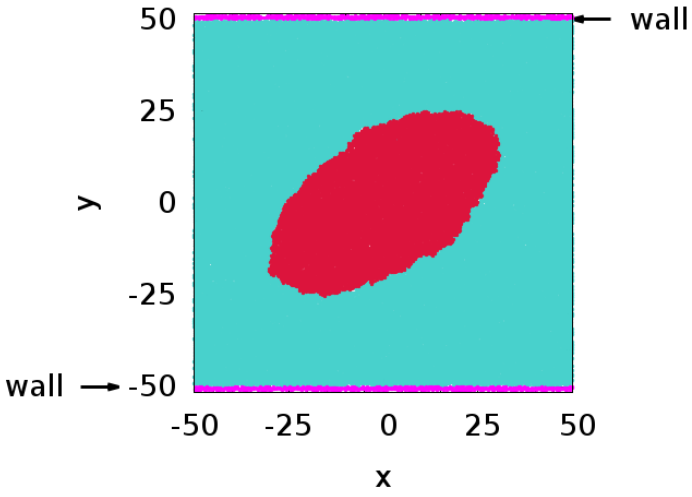

Fig. 5.10 Performance of a steady drop in shear flow.

5.4 Contact Angle

So far, we have considered the interface only between two fluid phases. However, the interaction of a drop with a Janus colloid needs to be taken into account to investigate its behavior in binary mixtures. So, we need to consider contact between the fluid and a solid surface, which leads to a wetting phenomenon. For example, the fluid that interacts with the walls in figure 5.7b completely wets the surfaces. Wetting of a liquid at a solid surface can affect the phase behavior of fluid i.e. the critical point changes. Furthermore, it can change the concentration of the drop and therefore, the related heat transfer [159]. Surface wetting is characterized by a contact angle θ_C which is defined in figure 5.11 and determines the shape of a drop.

The equilibrium contact angle θ_C is determined by the Young equation:

$$\cos(\theta_C) = \frac{\Gamma_{BS} - \Gamma_{AS}}{\Gamma_{AB}} \tag{5.8}$$

where Γ_{AB} is the interfacial energy related to the surface tension, Γ_{AS} and Γ_{BS} are the interfacial energies for type A-wall and type B-wall interactions respectively. By changing the interaction force coefficients, the interfacial energies are altered and the contact angle can adjusted from 0 to 180°. A wall is created from DPDe particles distributed uniformly with a line density $N_c = 400/(8\pi)$ (similar to the model of Janus colloid in the previous chapter). The strength of conservative forces is set to $a_{AS} = a_{BS} = 6$. The strength of attraction and repulsion are the same as for fluid-fluid interaction $A_0 = 1.05, B_0 = 2.0$. Conservative

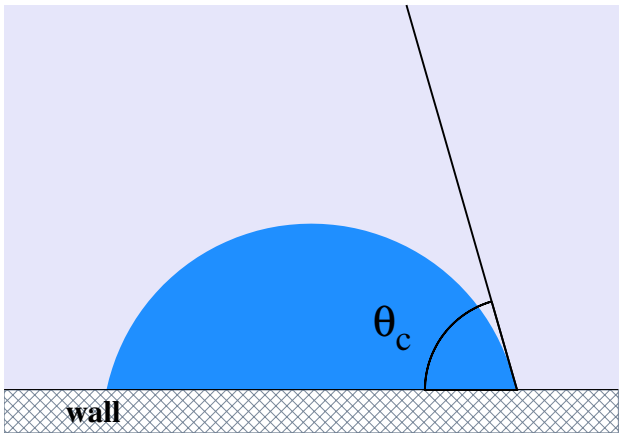

Fig. 5.11 Schematic of a drop and definition of contact angle

interactions between fluid and wall particles consist of a short-range repulsion and long-range attraction with the weight function from equation (4.23) where the cutoff radius of repulsion part is given by:

$$r_{c_1}(T_{ij}) = \begin{cases} a_0^{type-wall} r_c & T_{ij} < T_{min} \\ \left(b_0^{type-wall} \dfrac{T_{ij} - T_{min}}{T_{max} - T_{min}} + a_0^{type-wall} \dfrac{T_{max} - T_{ij}}{T_{max} - T_{min}} \right) r_c & T_{min} < T_{ij} < T_{max}, \\ b_0^{type-wall} r_c & T_{max} < T_{ij} \end{cases} \tag{5.9}$$

where *type* can be *A* or *B*, and a_0 and b_0 are define the contact angle. The difference between A-wall and B-wall interactions is implemented by b_0. Note that $a_0^{A-wall} = a_0^{B-wall} = 0.8$. The contact angle is measured for a set of cutoffs:

$$\left(b_0^{A-wall}, b_0^{B-wall} \right) \in \{(0.85,1),(0.9,1),(0.95,1),(1,1),(1,0.95),(1,0.9)\} \tag{5.10}$$

Additionally we consider a weak purely repulsive Lennard-Jones interaction with $\varepsilon_{LJ} = 0.005, r_c^{LJ} = 0.25$ and $\sigma_{LJ} = r_c/2^{1/6}$ to prevent fluid penetration thorough the wall.

For measurement of the contact angle between the drop and wall, we ignore a thin layer in the vicinity of the wall, because of density fluctuations in this layer. A circle is fitted to the interface between the two fluids. Then the contact angle is calculated through the center and radius of the circle similar to the method suggested in references [159–161]. If the contact angle is larger than 90°, as in figure 5.12a, it is given by $\theta_C = \arcsin(h/r) + 90°$. In the case of $\theta_C < 90°$, the contact angle is $\theta_C = 90° - \arcsin(h/r)$, as it illustrated in figure 5.12b.

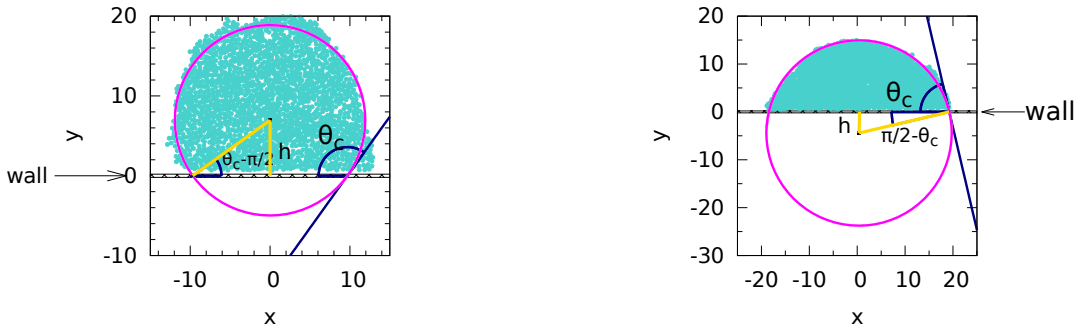

Fig. 5.12 Measurement of contact angle in the case of (a) $\theta_c > 90^\circ$ (a) $\theta_c < 90^\circ$.

The contact angle as a function of the potential coefficients for different number fractions is shown in figure 5.13. As expected from equation (5.8), since the energy of different interfacial areas is proportional to the number fraction in 2D, the number fraction does not have an effect on the contact angle. The contact angle changes from 30° to 110°, by increasing the repulsion between the drop and wall $\left(b_0^{A-wall}, b_0^{B-wall}\right) \in \{(0.85,1),(0.9,1),(0.95,1)\}$ or by decreasing the repulsion between the wall and the fluid B $\left(b_0^{A-wall}, b_0^{B-wall}\right) \in \{(1,0.95),(1,0.9)\}$.

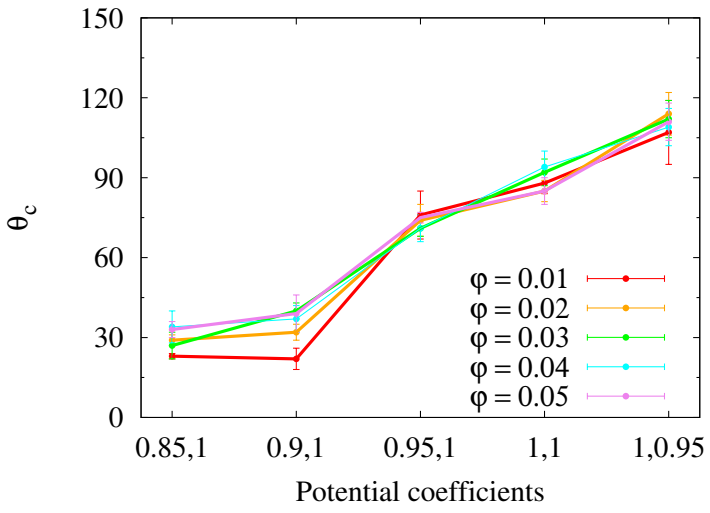

Fig. 5.13 Contact angle as a function of the potential coefficient for different number fractions.

Figure 5.8 shows that the surface tension or equivalently interfacial energy Γ_{AB} decreases if a_{AB} reduced. By decreasing Γ_{AB}, the drop tends to spread over the wall, and therefore interfacial energy between the drop and wall Γ_{AS} increases, whereas interfacial energy between the B fluid and wall Γ_{BS} decreases. The competition between the difference in

$\Gamma_{BS} - \Gamma_{AS}$ and Γ_{AB} defines how the contact angle changes. Figure 5.14 shows a change in θ_C for different surface tensions. For a small wetting angle, decreasing surface tension increases the contact angle or decreases the wetting. On the other hand at the large wetting angle, the surface tension, does not seem to affect the contact angle within the errors.

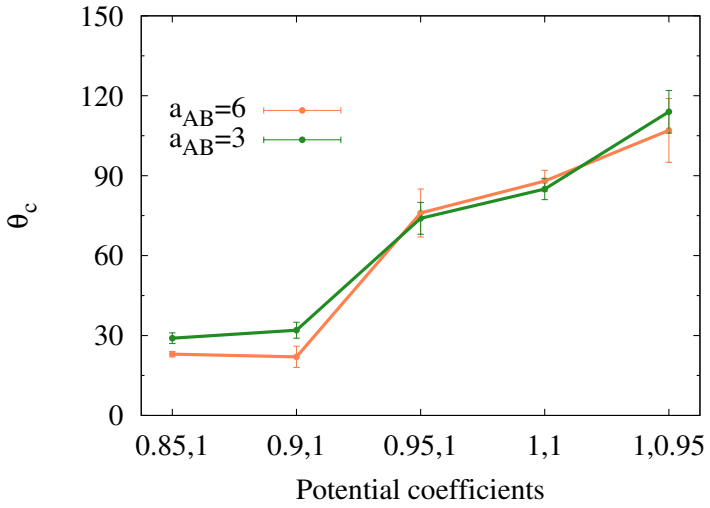

Fig. 5.14 Contact angle as a function of the potential coefficient between the wall and fluid for two different surface tensions.

5.5 Summary

In this chapter, simulations of a binary mixture in the homogeneous temperature condition were discussed for various boundary conditions in DPDe. The standard DPD conservative force results in a drop with low surface tension that even in the small shear flow, the drop is not formed. Additionally, the phase diagram is not similar to the real mixture. The long-range attraction and short-range repulsion conservative force allows us to model a drop in the fluid more accurately, such that we can control surface tension and also, the contact angle in the presence of a wall. Surface tension first increases strongly with conservative force coefficient between different species and then it increases but much slower. The contact angle as a function of potential coefficients changes from 30° to 110°. On the other hand, it models a binary fluid which shows phase behavior same as the real case.

Chapter 6

Heated Janus Colloid in a Binary Mixture

In the previous chapter, the behavior of a binary mixture modeled with DPDe has been explored. Here, we simulate a 2D Janus particle immersed in a binary mixture close to the critical point. The temperature in the vicinity of the hot cap is above the critical point and a drop forms there. First, we discuss three methods for applying a temperature gradient. Then the effects of number fraction, wetting, temperature gradient and surface tension on the drop shape and propulsive velocity of the Janus colloid are investigated.

6.1 Simulation Setup

6.1.1 Method

A binary mixture is modeled as described in section 5.3.2. Conservative interaction between fluid and colloid is modeled by equation (4.24) i.e. the weight function and repulsion cutoff radius are given by equations (4.23) and (5.9) respectively. In addition, a repulsive Lennard-Jones potential is added between fluid and colloid particles to prevent wall penetration.

In the vicinity of the hot cap, the temperature is above the critical temperature and a droplet forms here. Note that the critical temperature is $T_C = 0.64$. The size of colloid in the binary mixture is selected to be $R = 8r_c$ which is larger than Janus particle in the simple fluid (see section 4.1) in order to generate a small size droplet with a reasonable number of particles. Besides, the box size $100r_c \times 100r_c$ is sufficiently large to avoid significant finite-size effects.

6.1.2 Implementation of Temperature Gradient

The simplest way to implement a temperature gradient on the colloid is to fix the temperatures at the two caps: hot at a gold cap and cold at a non-metallic cap. In the experiments, half of the Janus particle coated by gold absorbs heat from a source and surrounding fluid cools down such that the temperature gradient is kept steady [42, 156] which would correspond to a fixed temperature at the hot metal side and a fixed average temperature in the system. Thus, we explore three types of implementing temperature gradient: (*i*) fixed temperature on the two halves of the colloid as it is mentioned above (*ii*) not fixing the temperature, but imposing a certain energy flux such that heating on one half of Janus particle and cooling at the other half and (*iii*) heating at one half of the Janus particle and cooling the fluid far away from the colloid surface. Note that in the last two cases, heating and cooling are done with the same magnitude of heat rate $|\dot{Q}_c| = |\dot{Q}_h|$ otherwise the average temperature of system is not constant.The third method of controlling temperature matches best the experiments and the fluid is cooled down in a thin slice at all boundaries of the periodic box within a thickness of cutoff radius r_c.

In order to compare the methods of implementation of the temperature gradient, heat rate is chosen such that the maximum temperature at the hot cap is always $T_{max} = 0.83$. Note that the critical temperature is $T_c = 0.64$. The heat rate in case of cooling on colloid is $\dot{Q} = 6.6 \times 10^4$ and in the case of cooling at the boundaries of the simulation box is $\dot{Q} = 3.3 \times 10^4$. Figure 6.1 shows temperature profiles around a colloid for different temperature conditions. The blue line shows a fixed temperature on both capes. The green line corresponds to heating and cooling at the colloid. The magenta line shows results of cooling in the fluid far from the colloid. In the later case, the variation of temperature around the colloid ΔT is about 32% of the maximum variation in the other two cases.

Corresponding steady state temperature profiles in the fluid are shown in figure 6.2. The largest and the smallest temperature gradients in the fluid correspond to the fixed temperature at the colloid (figure 6.2a) and cooling in the fluid with heating half of the Janus particle (figure 6.2c), respectively.

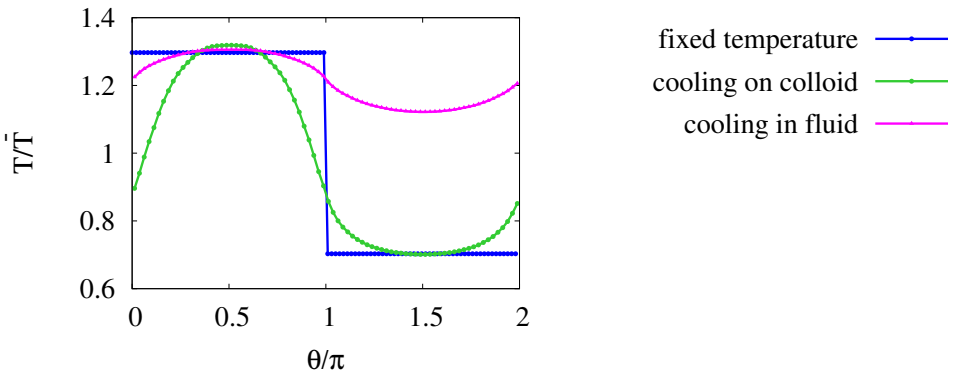

Fig. 6.1 Temperature profile around a heated colloid in a critical binary mixture for the three different ways of implementing temperature gradient: (*i*) temperature fixed at two caps (blue), (*ii*) heat rate fixed at two caps (green) and (*iii*) heating on the colloid while cooling is performed in whole fluid (magenta). The maximum temperature is fixed to $T_h = 0.83$ for all cases.

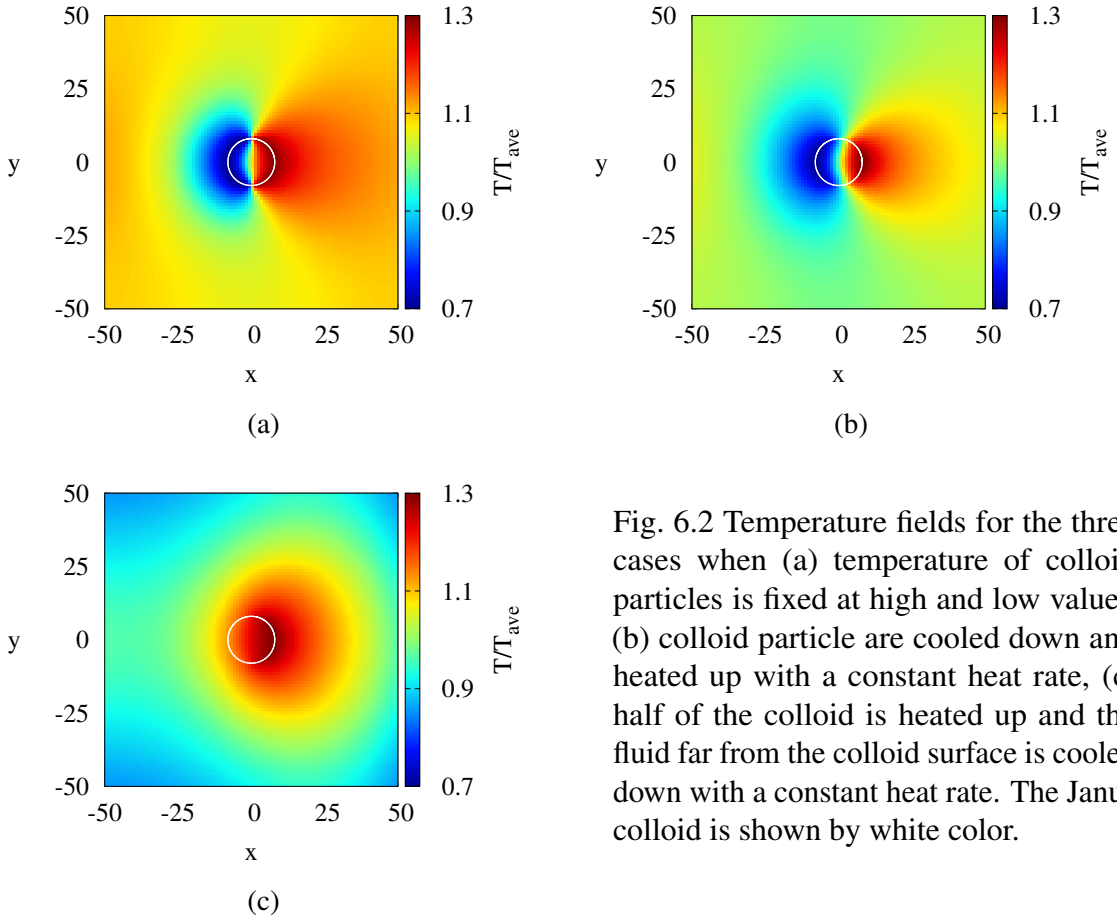

Fig. 6.2 Temperature fields for the three cases when (a) temperature of colloid particles is fixed at high and low values, (b) colloid particle are cooled down and heated up with a constant heat rate, (c) half of the colloid is heated up and the fluid far from the colloid surface is cooled down with a constant heat rate. The Janus colloid is shown by white color.

6.2 Velocity Field

Figure 6.3a shows flow streamlines of the fluid in the colloid frame (colloid is here fixed) where the color code represents the normalized velocity of the flow v/v_p where v_p is colloid velocity in the lab frame. Here temperature on the cold and hot cap are fixed. The droplet boundary is highlighted by the red dashed and white line in 6.3a and 6.3b, respectively. At the droplet interface, the velocity is close zero, indicating that the droplet moves with the colloid in the lab frame (colloid is free to move). Besides the inside of droplet flow is negligible which means in the interface of the droplet and hot cap of colloid velocity of the fluid is zero while in figure 4.10 is shown the flow is generated in the vicinity of the caps. According to discussion in reference [156] the flow is produced by a force in the border of the droplet and fluid where there is the largest concentration gradient and it transfers to the hot cap through the droplet.

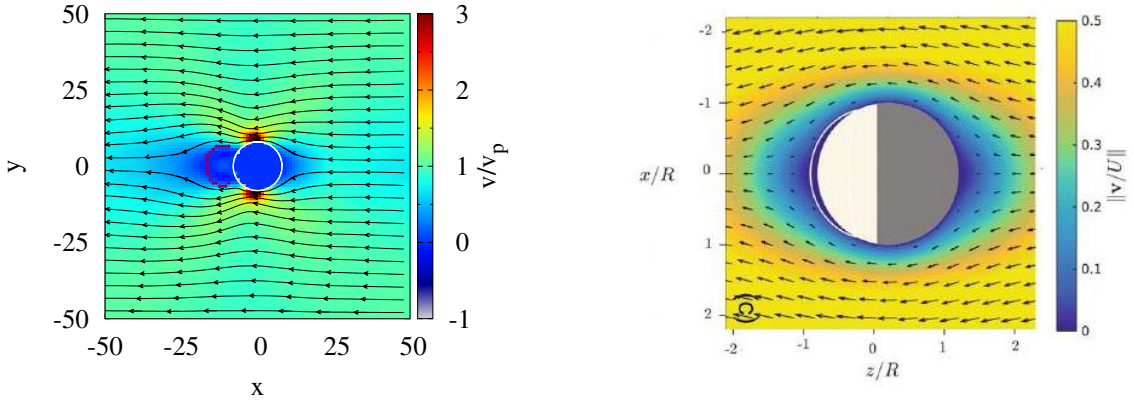

Fig. 6.3 The flow pattern in the temperature field of Janus colloid immersed in the binary mixture close to the critical point with a droplet in the vicinity of the hot cap from (a) simulation with DPDe (b) numerical solution of Navier–Stokes equation. The color code represents the normalized velocity. Figure adopted from reference [156], available under a Creative Commons license.

6.3 Effect of Number Fraction

We evaluate the velocity v_p of the Janus colloid with the droplet in simulations with a fixed particle. In order to determine the Peclet number we assume that the rotational diffusion is independent of the droplet and is calculated using equation (4.12). Smoother temperature profiles for the strategies with a constant heat rate (instead of fixing temperature) result in a

$\varphi_A = 0.01$	$\varphi_A = 0.03$	$\varphi_A = 0.05$
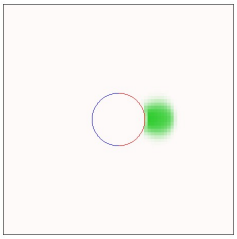	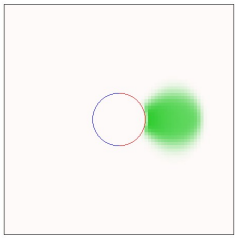	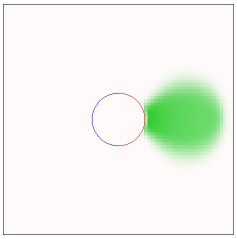

Table 6.1 Droplet shape for different droplet sizes

slower propulsion because the local temperature gradients are smaller. Peclet number versus number fraction of fluid A is shown in figure 6.4. Note that the number fraction of type A is much smaller than the other type in order to reach a small drop size. Additionally by increasing a number fraction the droplet size increases (see table 6.1). Therefore the droplet size can be considered as a number fraction. Peclet numbers reached for a fixed heat rate (green line) are smaller than those for the fixed temperature control (blue line) by about 30%, but their dependence is similar. Interestingly when cooling is performed in the fluid (magenta line), propulsive velocity decreases as a function of number fraction such that at large number fraction $\varphi_A \geq 0.03$ the direction of motion is reversed. The magnitude of propulsive velocity for a small droplet or small number fraction $\varphi_A = 0.01$ is similar to that for the large one $\varphi_A = 0.05$ but in the opposite direction with he droplet on same side (hot cap). In the experiment, a similar dependence is reported with respect to the size of the droplet [156]. However, currently we can not explain this behavior.

6.4 Effect of Wetting

Contact angle is adjusted by changing a_0 and b_0 in equation 5.9 leading to the contact angles shown in figure 5.13. Table 6.2 shows a schematic diagram of the Janus particle with a droplet for different contact angles where the temperature on the colloid is fixed (first scheme) and $\varphi = 0.01$.

The contact angle and droplet size (or in other words shape of the droplet) affect propulsive velocity. Figure 6.5a shows Peclet number as a function of contact angle where each line represents one number fraction in the system with a fixed temperature on the colloid. Peclet number decreases with size of the droplet. As a function of contact angle θ_C, Peclet number first increases, then it remains constant in the range of $34^\circ \leq \theta_C \leq 90^\circ$ and finally decreases for larger θ_C. Figure 6.5b presents Peclet number as a function of contact angle

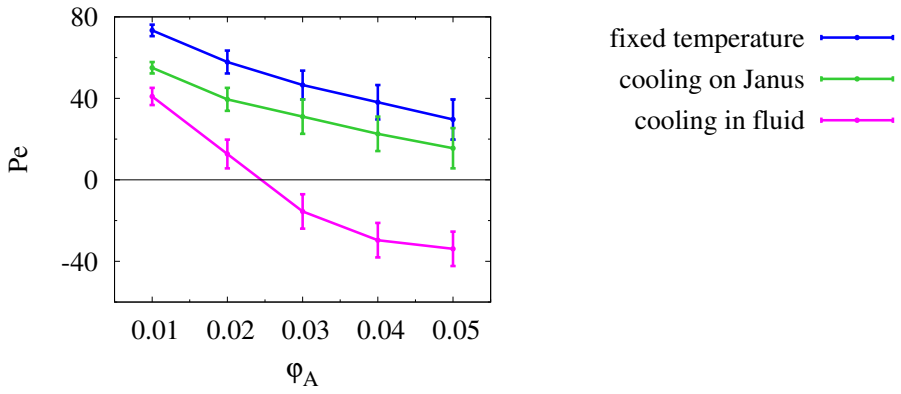

Fig. 6.4 Peclet number as a function of number fraction for different methods of implementing temperature gradient: (*i*) temperature fixed at the two caps (blue), (*ii*) heat rate fixed at the two caps (green) and (*iii*) the Janus particle is heated while cooling is done in the fluid. The maximum temperature $T = 0.83$ is the same for all cases.

$\theta_c = 30°$	$\theta_c = 90°$	$\theta_c = 110°$
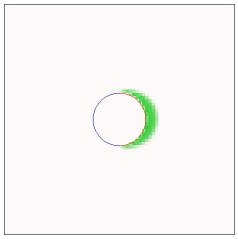	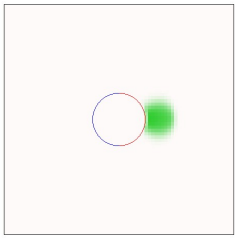	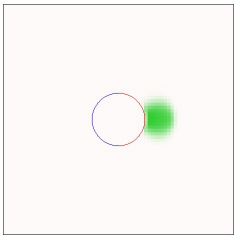

Table 6.2 Droplet shape for different contact angles

with $\varphi_A = 0.01$ for the three different temperature controls (*i*) fixed temperature on the colloid (blue line), (*ii*) fixed heat rate on the colloid (green line) and (*iii*) heating at the colloid with cooling in the fluid (magenta line). The strategies of cooling and heating with a fixed heat rate and for a fix temperature results in similar propulsive velocity trends. However, when cooling is done in the fluid, Peclet number increases for $\theta_C \leq 34°$, and then shocks a different behavior with a minimum at $\theta_C = 90°$. In the third temperature profile, the peak at $\theta_C = 110°$ can be explained by the smaller drop size due to a strong wetting, temperature field or even both. Note that, temperature decreases faster as a function of the distance around the hot cap in comparison to two other cases.

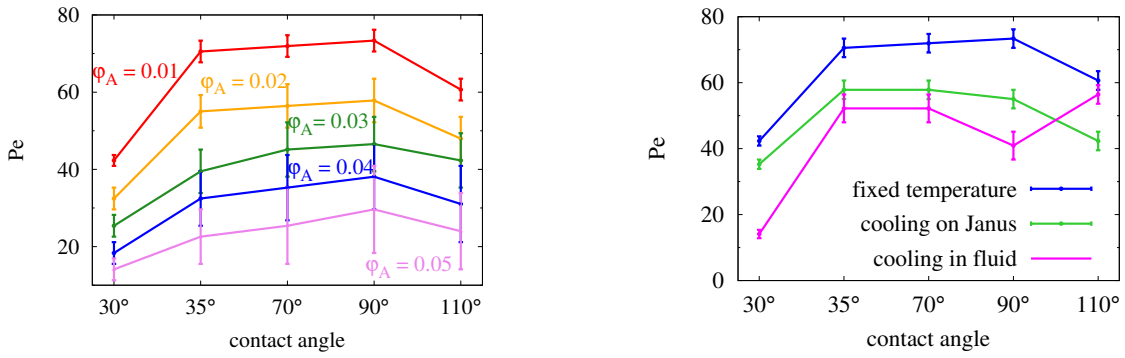

Fig. 6.5 Propulsive velocity as a function of contact angle for (a) various sizes of the droplet with a fixed temperature on the Janus particle and (b) for different temperature control strategies.

6.5 Effect of Temperature Gradient

Effect of temperature gradient on the Peclet number of the Janus particle in a simple fluid is illustrated in figure 4.13 in section 4.3, where for $\Delta T/\bar{T} < 0.7$ propulsive velocity behaves as a linear function of temperature gradient and then it drops out. Note that here, the largest (T_{hot}) and smallest temperature change but average temperature is $\bar{T} = 0.64$ in all cases. A Janus particle in a binary mixture for a fixed temperature on the colloid shows the same trend. By increasing the temperature gradient, the temperature at the hot part increases and the droplet size grows. Figure 6.6 shows droplet size and density as a function of the temperature gradient. For small temperature differences $\Delta T/\bar{T} < 0.2$, temperature at the hot part is below the critical point and there is no droplet formed. By increasing temperature, a droplet forms at the hot side and becomes larger in size. Density for temperature in the range of $0.2 \leq \Delta T/\bar{T} \leq 0.6$ shows a linear increase , while the size of the droplet for temperature in the range of $0.4 \leq \Delta T/\bar{T} \leq 0.6$ decreases linearly. If the temperature is much higher than the critical value $\Delta T/\bar{T} > 0.6$, two-phases are completely separated and no significant changes in size of droplet and density are observed.

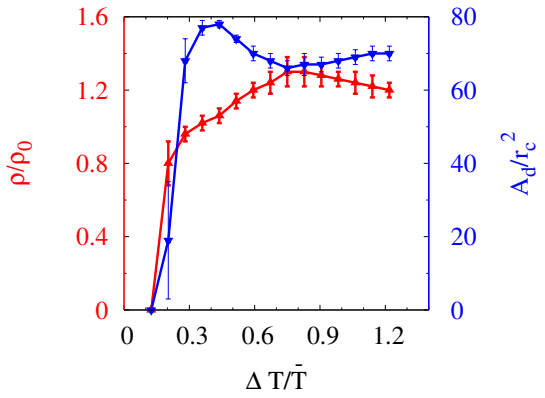

Fig. 6.6 Size of the droplet (blue) and density inside the droplet (red) as a function of temperature gradient for the number fraction fixed at $\varphi_A = 0.01$ and with the fixed temperature strategy.

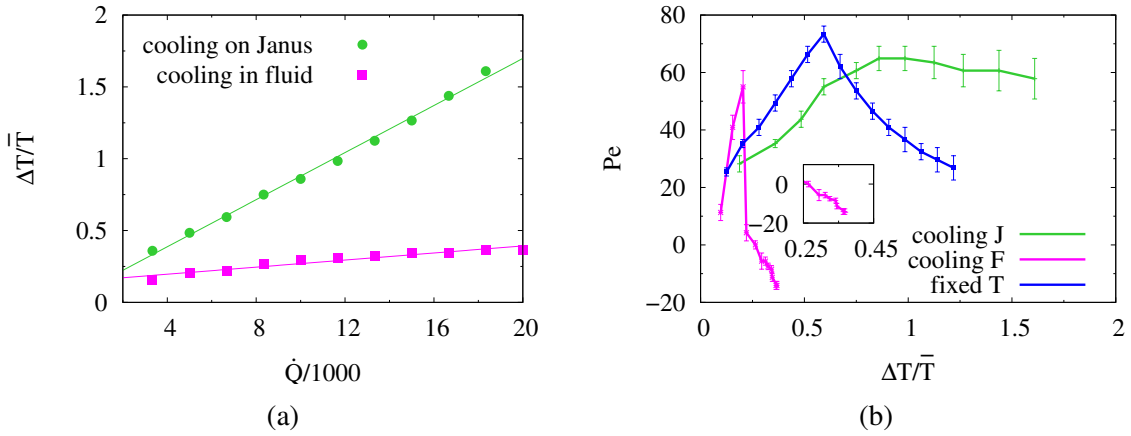

Fig. 6.7 (a) Temperature difference as a function of heat rate and (b) propulsive velocity as a function of temperature difference where green and magenta lines show cooling on Janus colloid and in binary fluid, respectively. The blue line represents data for fixed temperature control. The inset graph shows the range that droplet forms in the cooler cap.

Figure 6.7a shows that the temperature normalized by average temperature is a linear function of heat rate but for the case of cooling is on the colloid it has a larger slope. Note that in this figure, the average temperature is defined as an average temperature of colloid particles and it is higher for the case of cooling in the fluid. Propulsive velocity as a function of $\Delta T/\bar{T}$ has dissimilar trends for the different methods of implementing the temperature gradient (see figure 6.7b). Blue line corresponds to a Janus particle with a fixed temperature, for which Peclet number first increases linearly and then it drops down. According to equation (5.9), temperature gradient results in conservative force gradient around the colloid. At larger ΔT, around the hot (cold) cap area in the fluid with the temperature $T > 0.83$ ($T < 0.45$) is larger.

Note that in this region, the cutoff radius of the repulsive part is constant and therefore also conservative force. From the chapter 4, we know that a constant conservative force with the temperature results in a smaller Peclet number. If cooling and heating are done at the colloid, propulsive velocity increases linearly with a heat rate for $\Delta T/\bar{T} < 1.1$ and for larger heat rates there is a plateau (green line in figure 6.7b). In this case, since the temperature profile is smoother, the conservative force gradient does not disappear completely and propulsive velocity does not decline as a function of the temperature gradient. The results of the system with cooling in the fluid are shown by the magenta line. Peclet number rises for $\Delta T/\bar{T} < 0.2$ with a sharp peak at $\Delta T/\bar{T} = 0.2$. After that it rapidly drops and the direction of motion changes. For negative Peclet numbers, temperature around the Janus colloid is much larger than the critical temperature $\bar{T} > 1$ and a droplet forms in the vicinity of the non-heating cap. The inset graph in figure 6.7b shows this range of ΔT.

6.6 Effect of Surface Tension

Table 6.3 shows a schematic diagram of the Janus particle with a droplet for different surface tensions where the temperature on the colloid is fixed (first scheme) and $\varphi = 0.01$. Investigation of the effect of surface tension on the propulsive velocity of Janus particle is performed for fixed temperature at the Janus colloid $T_{hot} = 0.83$ and $T_{cold} = 0.45$. Figure 5.8 shows that the surface tension of the droplet increases with the strength of interaction between two types of fluids a_{AB}. Here, we study propulsive velocity as a function of the strength of interaction between two species, i.e. surface tension. The droplet is not stable at the hot cap with $T_{hot} = 0.83$, where $a_{AB} = 2.5$ and $\varphi_A = 0.01$. In fact, the droplet has a short lifetime there. In other words, it forms but since the surface tension is low, the droplet is broken by the flow, and then it forms again and again. The effect of number fraction on the critical point also supports that there is no stable droplet for $a_{AB} = 2.5$ and $\varphi_A = 0.01$, while for $\varphi_A = 0.05$, a smaller droplet forms with the area $A_d/r_c^2 = 11.0$ and Peclete number $Pe = 83(4)$. Note that for number fraction $\varphi_A = 0.05$, the droplet shrink to about 16% by changing $a_{AB} = 6$ to $a_{AB} = 3$. Figure 6.8 shows the average density and drop size as a function of number fraction for smaller and larger surface tension. In the systems with smaller surface tension $a_{AB} = 3$, the size of a drop and average density are smaller.

Figure 6.9 shows that for number fraction $\varphi_A = 0.01$, propulsive velocity first decreases as a function of the strength of interaction between two fluid types if $a_{AB} < 4$ while for larger values, v_p converges to a plateau value. Note that for $\varphi_A = 0.01$ a stable droplet forms if $a_{AB} \geq 2.8$.

$a_{AB} = 3$	$a_{AB} = 3.3$	$a_{AB} = 6$
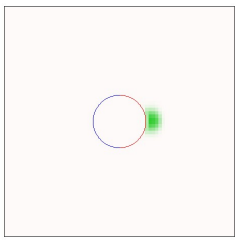	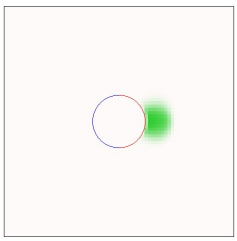	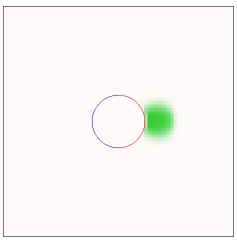

Table 6.3 Droplet shape for different surface tension

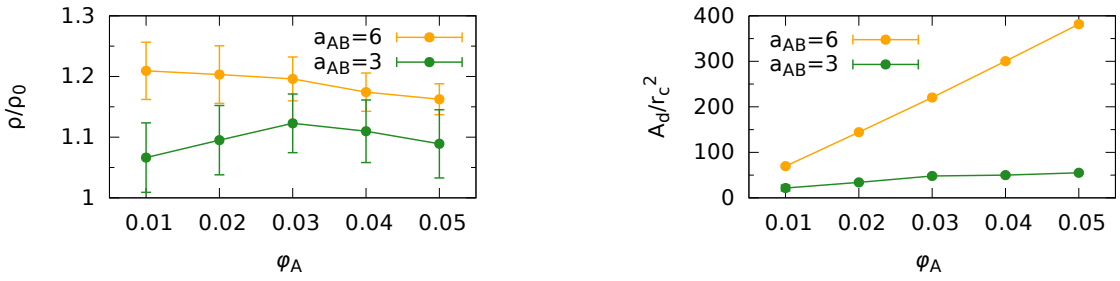

(a) (b)

Fig. 6.8 (a) Density in a drop and (b) drop size as a function of number fraction for two different surface tensions.

As a function of number fraction φ_A, Peclet number decreases more rapidly in the case of a larger surface tension $a_{AB} = 6$ (see figure 6.10).

Effect of surface tension on Peclet number as a function of the strength of interaction between two fluid types and wall (or equivalently the contact angle) is shown in figure 6.11. Peclet number increases when both types of fluids are attracted to the wall equally i.e $\left(b_0^{A-wall}, b_0^{B-wall}\right) = (1,1)$ or the droplet wets the wall stronger i.e $\left(b_0^{A-wall}, b_0^{B-wall}\right) \in \{(0.85,1),(0.9,1),(0.95,1)\}$ in figure 6.11. There is a higher peak in Peclet number at the point where two types interact with the colloid in the same way for $a_{AB} = 3$. If the droplet is attracted strongly to the colloid $\left(b_0^{A-wall}, b_0^{B-wall}\right) \in \{(0.85,1),(0.9,1)\}$ from potential coefficient axis in figure 6.11), surface tension does not affect propulsion. Otherwise, a smaller surface tension results in a stronger propulsion.

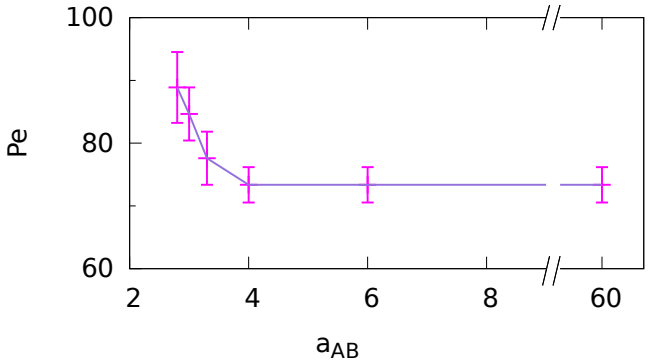

Fig. 6.9 Peclet number as a function of the strength of interactions between unlike fluids. Note that the strength of attraction determines the surface tension of the droplet.

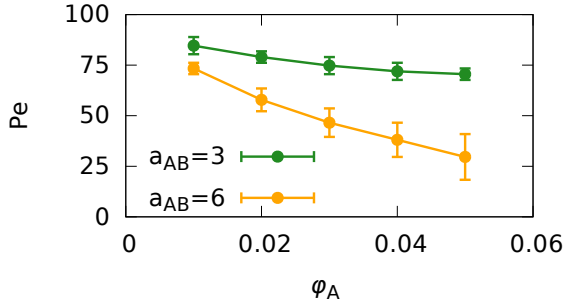

Fig. 6.10 Peclet number as a function of number fraction for two different surface tensions.

6.7 Summary

We have presented a simulation of Janus particle in a binary mixture by DPDe. The contact angle or wetting behavior are changed by colloid-fluid interaction, and surface tension is controlled by fluid-fluid interactions. We study the effect of drop size by temperature gradient and number fraction. Results confirm the propulsive velocity decreases as a function of drop size. Three different methods are used in order to implement temperature gradient: (*i*) temperature is fixed on two values at colloid caps, (*ii*) one cap is heated with $\dot{Q}$ and the other one is cooled with $-\dot{Q}$, and (*iii*) one cap is heated up and the fluid far away from the colloid surface is cooled down. The first two methods are easier to control the temperature gradient, but the third generates a temperature field as in experiments. In the first two methods, propulsive velocity as a function of number fraction and contact angle shows the same trend but the method with fixed temperature presents larger propulsive velocity (about three times). Propulsive velocity increases with contact angle, with a maximum at $\theta = 90^{\circ}$. In this method,

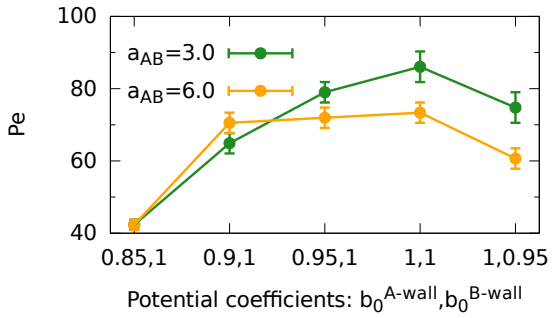

Fig. 6.11 Peclet number as a function of wetting (potential coefficient between the wall and fluid) for two different surface tensions.

propulsive velocity decreases over number fraction and the direction of motion changes. Note that by increasing the number fraction the size of a drop increases. These results are similar to experiments. As a function of contact angle, there is a a local minimum at $\theta = 90^\circ$ and the largest propulsive velocity is at $\theta = 110^\circ$. The maximum at this point can be explained by the smaller drop size which can be due to the higher critical point as a result of large wetting or different temperature field. With increasing the surface tension, Peclet number first decreases and then reaches a plateau. The drop with smaller surface tension shows the same but stronger trend as a function of contact angle i.e. the peak at 90° is higher.

Chapter 7

Conclusions and Outlook

In this work, we have developed a simulation method called DPDe to investigate the behavior of a heated Janus colloid which exhibits self-propelled motion in a critical binary mixture. First, a simple DPDe fluid, and then the implementation of a Janus particle in a one-component fluid with a temperature gradient were exhaustively checked. Afterwards, simulations of a critical binary mixture were performed, and finally the full system, where a Janus particle is immersed in a critical binary mixture in the presence of a temperature gradient, was investigated.

Energy conservation within the isothermal mesoscopic simulation technique DPD is problematic as simulation results show that energy is not conserved exactly [128–130], in spite of the theoretical prediction where the viscous heat flux between two particles are calculated by friction and random forces. In chapter 2, an integration scheme is introduced such that the viscous heat flux is calculated by the variation of mechanical energy. The integration algorithm is verified in chapter 3 by probing energy conservation, equality of internal and kinetic temperatures and radial distribution function for different timesteps, box sizes, models of conservative force and heat conduction. The results confirm that energy is conserved on the order of machine precision.

A fluid in a temperature gradient shows the same results for different definitions of heat conduction which are different functions of local temperature. A density gradient appears in the system as a consequence of temperature gradient and homogeneous pressure in the fluid. The behavior of the DPDe fluid is strongly affected by the employed parameters and in particular by the choice of the conservative force. If the conservative force is a linear function of temperature, a fluid behaves more similar to the ideal fluid in comparison with a conservative force independent of local temperature. Note that an ideal fluid shows the largest density gradient. Simulation results for mass and energy transport are verified by the analytical approach. Accordingly, an expression for the conductivity coefficient of the fluid

is obtained which is a quadratic function of temperature and density. The relation between the conductivity coefficient and either temperature or density were investigated theoretically and experimentally and different fluids show different dependencies on these two physical quantities. In the DPDe fluid, energy is transfered by conduction and through the random motion of particles. The conduction part is proportional to the mesoscopic heat conduction coefficient κ_0. Since, diffusion is a slow process, the mesoscopic conduction coefficient is the main factor that determines the maximum heat flux within the system. In fact, the imposition of a large heat rate within a system with a small mesoscopic conduction coefficient leads to simulation failure, since heat cannot be efficiently spread within the system.

In chapter 4, thermophoretic Janus particle is studied in two dimensions. The Janus particle is modeled by many beads with the temperature of particles at one half of the colloid is fixed at a higher value while the other half assumes a lower value. Then, the fluid attains the temperature of colloidal particles. Due to the temperature gradient, density and pressure gradients are generated, leading to a flow around the colloid in the colloid frame. The boundary conditions at the colloid surface affect the propulsive velocity. For instance, for a small conservative force coefficient representing interactions between Janus particles and fluid particles, the no-slip boundary conditions generate additional friction and the propulsive velocity decreases. Even though different fluid properties such as viscosity and conductivity alter the propulsive velocity, the Peclet number does not change significantly. The average temperature of fluid does not affect the propulsive velocity and therefore, the Peclet number decreases due to the enhancement of rotational diffusion. The density of particles representing the colloid surface, the interaction range and conductivity between colloid and fluid have a minor effect on both the propulsive velocity and the Peclet number. By increasing the size of a colloid and keeping the temperature gradient constant, the Peclet number increases linearly first and then drops. Details of the conservative force interaction between colloid and fluid determine the direction of motion and the magnitude of Peclet number. Namely, by choosing a longer-range attraction and a shorter-range repulsion, a colloid moves to one of the sides (hot or cold) with a stronger attraction. However, the Peclet number can increase up to one order of magnitude if the range of attraction (or equivalently repulsion) is a function of temperature. Rotational dynamics is studied by considering the exponential decay of the autocorrelation function of the orientational vector of the colloid in time. The Einstein relation for rotational diffusion factor in 2D is examined for various colloid sizes. There is a slight shift between theoretical and simulation results which may be due to the assumption of stick boundary conditions in the theory and a partial slip in simulations.

In order to advance to simulations of a Janus particle in a critical binary mixture, we focus in chapter 5 on three aspects of a critical binary mixture: a phase transition profile, the stability of a drop in flow, and the contact angle in the presence of a wall. In the DPDe simulation model, all of these are determined by the conservative interaction. Here, a symmetric binary mixture was considered i.e. the interaction between particles of similar species is the same, but it differs for dissimilar types: $U_{AA} = U_{BB} \neq U_{AB}$. In the original DPD, at a specific number fraction, a binary mixture is mixed at a temperature above a corresponding phase transition temperature and is demixed below. An opposite behavior can also be desirable but not achievable within the original DPDe. Furthermore, the phase transition occurs within a small range of parameters. This restriction on choice of parameters results into a very small surface tension such that a droplet is unstable under flow near the critical point, and the contact angle is not easily adjustable. In chapter 5, an alternative approach to the original DPDe is presented by considering a cubic spline function for the conservative force which gives a good phase transition behavior by changing the transition point between attraction and repulsion parts. Furthermore, the resulting surface tension is large enough and a stable drop is formed under flow as strong as the flow generated by a self-propelled Janus particle in a critical binary mixture. The same choice of a conservative force between a wall and fluid leads to a controllable contact angle which can be adjusted within a wide range of angles.

In chapter 6, using the results obtained in previous chapters, a Janus particle in a binary mixture is simulated. The temperature gradient is implemented through three different methods: (*i*) temperature is fixed at the hot and cold caps at large and small values, respectively, (*ii*) a fixed rate of heat is applied at the colloid surface so that one half receives a fixed amount of heat while the other half loses this same amount, (*iii*) one half of the colloid is heated with a constant rate while the fluid particles far from the colloid surface are cooled by the exactly same amount of heat in total. The first two methods are more desirable in simulations since the temperature gradient can be controlled easily, but the third method gives a temperature field similar to experiments [42, 156]. In order to compare these methods, the maximum temperature at the hot cap is kept similar. The first two methods have same total temperature difference, but the temperature gradient at poles is larger for a Janus particle with fixed temperatures at the caps. In the third method, the temperature difference is three times smaller than in the two other cases. Temperature around the hot cap may be above the critical temperature leading to a drop formation.The size of a droplet is adjusted by modifying the temperature gradient and the volume fraction. The first two methods of implementing temperature gradient show that the propulsive velocity decreases with increasing the number fraction in the fluid mixture, and also that a Janus particle with a

very large droplet size eventually stop moving. Using the third method, propulsive velocity decreases with increasing the droplet size until it reaches zero and afterward the direction of motion changes with a magnitude which can be as large as a Janus particle with a very small droplet. The same trend is reported in a recent experimental study [156]. Contact angle also affects the propulsive velocity such that the first two methods present small propulsive velocity where the droplet contact angle is 30°. By increasing the contact angle, first, the propulsive velocity increases, then exhibits a plateau up to the point where contact angle is 90°, and then the propulsive velocity decreases. Using the third method, the propulsive velocity first shows the same trend but then a plateau appears within a smaller interval and there is a local minimum at $\theta_C = 90°$. Surprisingly, the propulsive velocity increases for very large contact angle, which can be explained by the droplet size. Here, the temperature field leading to the formation of a smaller droplet which explains a larger propulsive velocity. Surface tension plays a key role in the droplet size. For example, when the surface tension is changed by a factor two, the droplet size can increase up to eight times which results into the negligible propulsive velocity. Note that if the surface tension is larger than a certain value, it does not influence the droplet size and propulsive velocity anymore.

The work in this thesis opens a member of opportunities for further interesting investigations. For example, a study of interactions between a Janus particle and a wall would help us understand the behavior of a Janus particle near patterned substrates. Such a system is more realistic for mimicking the behavior of real microswimmers. Interactions between several Janus particles in a critical binary mixture is another interesting problem since it would unravel their collective behavior such as colloidal aggregation. A thermophoretic Janus particle can be used to determine biomolecular interactions [162].

References

[1] David R Lide. *CRC handbook of chemistry and physics*, volume 85. CRC press, 2004.

[2] Marvin J Weber. *Handbook of optical materials*, volume 19. CRC press, 2002.

[3] Reiji Mezaki, Masafumi Mochizuki, and Kohei Ogawa. *Engineering data on mixing*. Elsevier, 1999.

[4] Franziska Matthäus, Marko Jagodič, and Jure Dobnikar. E. coli superdiffusion and chemotaxis—search strategy, precision, and motility. *Biophysical journal*, 97(4):946–957, 2009.

[5] Kyriacos C Leptos, Jeffrey S Guasto, Jerry P Gollub, Adriana I Pesci, and Raymond E Goldstein. Dynamics of enhanced tracer diffusion in suspensions of swimming eukaryotic microorganisms. *Physical Review Letters*, 103(19):198103, 2009.

[6] Peter JM Van Haastert and Peter N Devreotes. Chemotaxis: signalling the way forward. *Nature reviews Molecular cell biology*, 5(8):626, 2004.

[7] Sidney L Tamm and George Adrian Horridge. The relation between the orientation of the central fibrils and the direction of beat in cilia of opalina. *Proc. R. Soc. Lond. B*, 175(1040):219–233, 1970. DOI: https://doi.org/10.1098/rspb.1970.0020.

[8] Christopher Brennen and Howard Winet. Fluid mechanics of propulsion by cilia and flagella. *Annual Review of Fluid Mechanics*, 9(1):339–398, 1977. DOI: https://doi.org/10.1146/annurev.fl.09.010177.002011.

[9] Emiley A Eloe, Federico M Lauro, Rudi F Vogel, and Douglas H Bartlett. The deep-sea bacterium photobacterium profundum ss9 utilizes separate flagellar systems for swimming and swarming under high-pressure conditions. *Applied and environmental microbiology*, 74(20):6298–6305, 2008. DOI: https://doi.org/10.1128/AEM.01316-08.

[10] Giovanni Volpe, Ivo Buttinoni, Dominik Vogt, Hans-Jürgen Kümmerer, and Clemens Bechinger. Microswimmers in patterned environments. *Soft Matter*, 7(19):8810–8815, 2011.

[11] Patrick Degen. Self-propelling capsules as artificial microswimmers. *Current Opinion in Colloid & Interface Science*, 19(6):611–619, 2014.

[12] Leonardo F Valadares, Yu-Guo Tao, Nicole S Zacharia, Vladimir Kitaev, Fernando Galembeck, Raymond Kapral, and Geoffrey A Ozin. Catalytic nanomotors: Self-propelled sphere dimers. *Small*, 6(4):565–572, 2010.

[13] Jonathan R Howse, Richard AL Jones, Anthony J Ryan, Tim Gough, Reza Vafabakhsh, and Ramin Golestanian. Self-motile colloidal particles: from directed propulsion to random walk. *Physical review letters*, 99(4):048102, 2007.

[14] Pulak K Ghosh, Yunyun Li, Fabio Marchesoni, and Franco Nori. Pseudochemotactic drifts of artificial microswimmers. *Physical Review E*, 92(1):012114, 2015.

[15] Mingcheng Yang, Adam Wysocki, and Marisol Ripoll. Hydrodynamic simulations of self-phoretic microswimmers. *Soft Matter*, 10(33):6208–6218, 2014.

[16] Eric E Keaveny and Martin R Maxey. Interactions between comoving magnetic microswimmers. *Physical Review E*, 77(4):041910, 2008.

[17] Jens Elgeti, Roland G Winkler, and Gerhard Gompper. Physics of microswimmers—single particle motion and collective behavior: a review. *Reports on progress in physics*, 78(5):056601, 2015.

[18] Ramin Golestanian. Collective behavior of thermally active colloids. *Physical review letters*, 108(3):038303, 2012.

[19] Borge Ten Hagen, Raphael Wittkowski, Daisuke Takagi, Felix Kümmel, Clemens Bechinger, and Hartmut Löwen. Can the self-propulsion of anisotropic microswimmers be described by using forces and torques? *Journal of Physics: Condensed Matter*, 27(19):194110, 2015.

[20] Mingjun Xuan, Jingxin Shao, Xiankun Lin, Luru Dai, and Qiang He. Self-propelled janus mesoporous silica nanomotors with sub-100 nm diameters for drug encapsulation and delivery. *ChemPhysChem*, 15(11):2255–2260, 2014. DOI: https://doi.org/10.1002/cphc.201402111.

[21] Daniel Kagan, Rawiwan Laocharoensuk, Maria Zimmerman, Corbin Clawson, Shankar Balasubramanian, Dae Kang, Daniel Bishop, Sirilak Sattayasamitsathit, Liangfang Zhang, and Joseph Wang. Rapid delivery of drug carriers propelled and navigated by catalytic nanoshuttles. *Small*, 6(23):2741–2747, 2010.

[22] Wei Gao, Daniel Kagan, On Shun Pak, Corbin Clawson, Susana Campuzano, Erdembileg Chuluun-Erdene, Erik Shipton, Eric E Fullerton, Liangfang Zhang, Eric Lauga, et al. Cargo-towing fuel-free magnetic nanoswimmers for targeted drug delivery. *small*, 8(3):460–467, 2012.

[23] Wei Wang, Wentao Duan, Suzanne Ahmed, Thomas E Mallouk, and Ayusman Sen. Small power: Autonomous nano-and micromotors propelled by self-generated gradients. *Nano Today*, 8(5):531–554, 2013.

[24] Geoffrey A Ozin, Ian Manners, Sébastien Fournier-Bidoz, and André Arsenault. Dream nanomachines. *Advanced Materials*, 17(24):3011–3018, 2005.

[25] Lluís Soler and Samuel Sánchez. Catalytic nanomotors for environmental monitoring and water remediation. *Nanoscale*, 6(13):7175–7182, 2014.

[26] Rémi Dreyfus, Jean Baudry, Marcus L Roper, Marc Fermigier, et al. Microscopic artificial swimmers. *Nature*, 437(7060):862, 2005.

[27] Stephen J Ebbens and Jonathan R Howse. In pursuit of propulsion at the nanoscale. *Soft Matter*, 6(4):726–738, 2010.

[28] Euan R Kay, David A Leigh, and Francesco Zerbetto. Synthetic molecular motors and mechanical machines. *Angewandte Chemie International Edition*, 46(1-2):72–191, 2007.

[29] Walter F Paxton, Shakuntala Sundararajan, Thomas E Mallouk, and Ayusman Sen. Chemical locomotion. *Angewandte Chemie International Edition*, 45(33):5420–5429, 2006.

[30] Manfred Schliwa and Gunther Woehlke. Molecular motors: switching on kinesin. *Nature*, 411(6836):424–426, 2001.

[31] Elena M Shchukina and Dmitry G Shchukin. Layer-by-layer coated emulsion microparticles as storage and delivery tool. *Current opinion in colloid & interface science*, 17(5):281–289, 2012.

[32] Brian J Williams, Sandeep V Anand, Jagannathan Rajagopalan, and M Taher A Saif. A self-propelled biohybrid swimmer at low reynolds number. *Nature communications*, 5:3081, 2014. DOI: https://doi.org/10.1038/ncomms4081.

[33] Li Zhang, Jake J Abbott, Lixin Dong, Bradley E Kratochvil, Dominik Bell, and Bradley J Nelson. Artificial bacterial flagella: Fabrication and magnetic control. *Applied Physics Letters*, 94(6):064107, 2009.

[34] M Leonetti. Cell movement by osmotic current. *EPL (Europhysics Letters)*, 32(7):561, 1995.

[35] Benedikt Sabass and Udo Seifert. Dynamics and efficiency of a self-propelled, diffusiophoretic swimmer. *The Journal of chemical physics*, 136(6):064508, 2012.

[36] WE Uspal, Mikhail N Popescu, S Dietrich, and M Tasinkevych. Self-propulsion of a catalytically active particle near a planar wall: from reflection to sliding and hovering. *Soft Matter*, 11(3):434–438, 2015.

[37] Jeremie Palacci, Stefano Sacanna, Asher Preska Steinberg, David J Pine, and Paul M Chaikin. Living crystals of light-activated colloidal surfers. *Science*, 339(6122):936–940, 2013.

[38] Klaus Kroy, Dipanjan Chakraborty, and Frank Cichos. Hot microswimmers. *The European Physical Journal Special Topics*, 225(11-12):2207–2225, 2016.

[39] Romy Schachoff, Markus Selmke, Andreas Bregulla, Frank Cichos, Daniel Rings, Dipanjan Chakraborty, Klaus Kroy, Katrin Günther, Anja Henning-Knechtel, Evgeni Sperling, et al. Hot brownian motion and photophoretic self-propulsion. *Diffusion-fundamentals. org*, 23:1–19, 2015.

[40] Santiago Muiños-Landin, Keyan Ghazi-Zahedi, and Frank Cichos. Reinforcement learning of artificial microswimmers. *arXiv preprint arXiv:1803.06425*, 2018.

[41] Ramin Golestanian, Tanniemola B Liverpool, and Armand Ajdari. Propulsion of a molecular machine by asymmetric distribution of reaction products. *Physical review letters*, 94(22):220801, 2005.

[42] Ivo Buttinoni, Giovanni Volpe, Felix Kümmel, Giorgio Volpe, and Clemens Bechinger. Active brownian motion tunable by light. *Journal of Physics: Condensed Matter*, 24(28):284129, 2012. DOI: https://doi.org/10.1088/0953-8984/24/28/284129.

[43] Hong-Ren Jiang, Natsuhiko Yoshinaga, and Masaki Sano. Active motion of a janus particle by self-thermophoresis in a defocused laser beam. *Physical review letters*, 105(26):268302, 2010.

[44] Larysa Baraban, Robert Streubel, Denys Makarov, Luyang Han, Dmitriy Karnaushenko, Oliver G Schmidt, and Gianaurelio Cuniberti. Fuel-free locomotion of janus motors: magnetically induced thermophoresis. *ACS nano*, 7(2):1360–1367, 2013.

[45] Mingcheng Yang and Marisol Ripoll. A self-propelled thermophoretic microgear. *Soft Matter*, 10(7):1006–1011, 2014. DOI: https://doi.org/10.1039/C3SM52417E.

[46] Yu-Liang Chen, Cheng-Xiang Yang, and Hong-Ren Jiang. Electrically enhanced self-thermophoresis of laser-heated janus particles under a rotating electric field. *Scientific reports*, 8(1):5945, 2018. DOI: https://doi.org/10.1038/s41598-018-24343-w.

[47] Martin Wagner and Marisol Ripoll. Hydrodynamic front-like swarming of phoretically active dimeric colloids. *EPL (Europhysics Letters)*, 119(6):66007, 2017. DOI: https://doi.org/10.1209/0295-5075/119/66007.

[48] Mojtaba Abdollahi and Seyed Javad Ahmadi. Application of ideal temperature gradient technology to optimize the chemical exchange and distillation process of boron isotopes separation by (ch3) 2o-bf3 complex. *Chemical Engineering and Processing: Process Intensification*, 76:26–32, 2014.

[49] J Calvin Giddings. Field-flow fractionation: analysis of macromolecular, colloidal, and particulate materials. *Science*, 260(5113):1456–1465, 1993.

[50] Mr Nikunj Adroja, Shruti B Mehta, and Mr Pratik Shah. Review of thermoelectricity to improve energy quality. In *International Journal of Emerging Technologies and Innovative Research JETIR*, volume 2. JETIR, 2015.

[51] Semen N Semenov and Martin E Schimpf. Molecular thermodiffusion (thermophoresis) in liquid mixtures. *Physical Review E*, 72(4):041202, 2005.

[52] CY Soong, WK Li, CH Liu, and PY Tzeng. Theoretical analysis for photophoresis of a microscale hydrophobic particle in liquids. *Optics express*, 18(3):2168–2182, 2010.

[53] Georgy Lebon, David Jou, and José Casas-Vázquez. *Understanding non-equilibrium thermodynamics*, volume 295. Springer, 2008.

[54] Eric Bringuier. Connection between thermophoresis and thermodiffusion in a liquid binary mixture. *Philosophical Magazine*, 91(11):1653–1664, 2011.

[55] Morteza Eslamian and M Ziad Saghir. On thermophoresis modeling in inert nanofluids. *International Journal of Thermal Sciences*, 80:58–64, 2014.

[56] Howard Brenner. Self-thermophoresis and thermal self-diffusion in liquids and gases. *Physical Review E*, 82(3):036325, 2010.

[57] Howard Brenner. A nonmolecular derivation of maxwell's thermal-creep boundary condition in gases and liquids via application of the lechatelier–braun principle to maxwell's thermal stress. *Physics of Fluids*, 21(5):053602, 2009.

[58] JK Platten and Pierre Costesèque. Charles soret. a short biography a. *The European Physical Journal E*, 15(3):235–239, 2004.

[59] Mingcheng Yang and Marisol Ripoll. Driving forces and polymer hydrodynamics in the soret effect. *Journal of Physics: Condensed Matter*, 24(19):195101, 2012. DOI: https://doi.org/10.1088/0953-8984/24/19/195101 .

[60] Marco Braibanti, Daniele Vigolo, and Roberto Piazza. Does thermophoretic mobility depend on particle size? *Physical review letters*, 100(10):108303, 2008. DOI: https://doi.org/10.1103/PhysRevLett.100.108303.

[61] Daniel Lüsebrink, Mingcheng Yang, and Marisol Ripoll. Thermophoresis of colloids by mesoscale simulations. *Journal of Physics: Condensed Matter*, 24(28):284132, 2012.

[62] Sela Samin and René van Roij. Self-propulsion mechanism of active janus particles in near-critical binary mixtures. *Physical review letters*, 115(18):188305, 2015.

[63] Carl Ludwig. *Diffusion zwischen ungleich erwärmten Orten gleich zusammengesetzter Lösung*. Aus der KK Hof-und Staatsdruckerei, in Commission bei W. Braumüller, Buchhändler des KK Hofes und der K. Akademie der Wissenschaften, 1856.

[64] MA Rahman and MZ Saghir. Thermodiffusion or soret effect: Historical review. *International Journal of Heat and Mass Transfer*, 73:693–705, 2014.

[65] Rio Kita and Simone Wiegand. Soret coefficient of poly (n-isopropylacrylamide)/water in the vicinity of coil- globule transition temperature. *Macromolecules*, 38(11):4554–4556, 2005. DOI: https://doi.org/10.1021/ma050526+.

[66] Saghir M. Ziad Srinivasan, Seshasai. *Thermodiffusion in Multicomponent Mixtures*. Springer, New York, 2013.

[67] Signe Kjelstrup and Dick Bedeaux. *Non-equilibrium thermodynamics of heterogeneous systems*, volume 16. World Scientific, 2008.

[68] Sybren Ruurds De Groot and Peter Mazur. *Non-equilibrium thermodynamics*. Courier Corporation, 2013.

[69] David MacGowan and Denis J Evans. Heat and matter transport in binary liquid mixtures. *Physical Review A*, 34(3):2133, 1986.

[70] W-T_ Ashurst and WG Hoover. Dense-fluid shear viscosity via nonequilibrium molecular dynamics. *Physical Review A*, 11(2):658, 1975.

[71] Audrey Hammack, Yeng-Long Chen, and Jennifer Kreft Pearce. Role of dissolved salts in thermophoresis of dna: lattice-boltzmann-based simulations. *Physical Review E*, 83(3):031915, 2011.

[72] Guillaume Matte-Deschênes, David Vidal, François Bertrand, and Robert E Hayes. Numerical investigation of the impact of thermophoresis on the capture efficiency of diesel particulate filters. *The Canadian Journal of Chemical Engineering*, 94(2):291–303, 2016.

[73] Jérôme Burelbach, David B Brückner, Daan Frenkel, and Erika Eiser. Thermophoretic forces on a mesoscopic scale. *Soft matter*, 14(36):7446–7454, 2018.

[74] Dmitry A Fedosov, Ankush Sengupta, and Gerhard Gompper. Effect of fluid–colloid interactions on the mobility of a thermophoretic microswimmer in non-ideal fluids. *Soft matter*, 11(33):6703–6715, 2015.

[75] S Jayaraj, KK Dinesh, and KL Pillai. Thermophoresis in natural convection with variable properties. *Heat and Mass Transfer*, 34(6):469–475, 1999.

[76] Davide Castelvecchi. *Focus: Mystery of Isotope Separation in Lava is Solved*, 2012.

[77] Doreen Niether, Dzmitry Afanasenkau, Jan KG Dhont, and Simone Wiegand. Accumulation of formamide in hydrothermal pores to form prebiotic nucleobases. *Proceedings of the National Academy of Sciences*, 113(16):4272–4277, 2016.

[78] Michael W Geis, Roderick R Kunz, and Margaret B Stern. Thermophoretic pump and concentrator, July 2 2002. US Patent 6,413,781.

[79] Emma L Talbot, Jurij Kotar, Lucia Parolini, Lorenzo Di Michele, and Pietro Cicuta. Thermophoretic migration of vesicles depends on mean temperature and head group chemistry. *Nature communications*, 8:15351, 2017.

[80] Moran Jerabek-Willemsen, Timon André, Randy Wanner, Heide Marie Roth, Stefan Duhr, Philipp Baaske, and Dennis Breitsprecher. Microscale thermophoresis: Interaction analysis and beyond. *Journal of Molecular Structure*, 1077:101–113, 2014. DOI: https://doi.org/10.1016/j.molstruc.2014.03.009.

[81] Horace Lamb. *Hydrodynamics*. Cambridge university press, 1993.

[82] Daan Frenkel and Berend Smit. *Understanding molecular simulation: from algorithms to applications*, volume 1. Elsevier, 2001.

[83] Sebastian Kmiecik, Dominik Gront, Michal Kolinski, Lukasz Wieteska, Aleksandra Elzbieta Dawid, and Andrzej Kolinski. Coarse-grained protein models and their applications. *Chemical Reviews*, 116(14):7898–7936, 2016.

[84] David Tritton. *Physical Fluid Dynamics*. Oxford Scince, 2nd eddition edition, 1988.

[85] Sauro Succi. *The lattice Boltzmann equation: for fluid dynamics and beyond*. Oxford university press, 2001.

[86] Guy R McNamara and Gianluigi Zanetti. Use of the boltzmann equation to simulate lattice-gas automata. *Physical Review Letters*, 61(20):2332, 1988.

[87] Markus Wittmann, Thomas Zeiser, Georg Hager, and Gerhard Wellein. Comparison of different propagation steps for lattice boltzmann methods. *Computers & Mathematics with Applications*, 65(6):924–935, 2013.

[88] Anatoly Malevanets and Raymond Kapral. Mesoscopic model for solvent dynamics. *The Journal of chemical physics*, 110(17):8605–8613, 1999.

[89] Anatoly Malevanets and Raymond Kapral. Solute molecular dynamics in a mesoscale solvent. *The Journal of Chemical Physics*, 112(16):7260–7269, 2000.

[90] JMVA Koelman and PJ Hoogerbrugge. Dynamic simulations of hard-sphere suspensions under steady shear. *EPL (Europhysics Letters)*, 21(3):363, 1993.

[91] PJ Hoogerbrugge and JMVA Koelman. Simulating microscopic hydrodynamic phenomena with dissipative particle dynamics. *EPL (Europhysics Letters)*, 19(3):155, 1992.

[92] Pep Espanñol and Patrick Warren. Statistical mechanics of dissipative particle dynamics. *EPL (Europhysics Letters)*, 30(4):191, 1995.

[93] CA Marsh, G Backx, and MH Ernst. Static and dynamic properties of dissipative particle dynamics. *Physical Review E*, 56(2):1676, 1997.

[94] I Pagonabarraga, MHJ Hagen, and D Frenkel. Self-consistent dissipative particle dynamics algorithm. *EPL (Europhysics Letters)*, 42(4):377, 1998.

[95] AJ Masters and PB Warren. Kinetic theory for dissipative particle dynamics: The importance of collisions. *EPL (Europhysics Letters)*, 48(1):1, 1999.

[96] Y Kong, CW Manke, WG Madden, and AG Schlijper. Effect of solvent quality on the conformation and relaxation of polymers via dissipative particle dynamics. *The Journal of chemical physics*, 107(2):592–602, 1997.

[97] NA Spenley. Scaling laws for polymers in dissipative particle dynamics. *EPL (Europhysics Letters)*, 49(4):534, 2000.

[98] Peter V Coveney and Keir E Novik. Computer simulations of domain growth and phase separation in two-dimensional binary immiscible fluids using dissipative particle dynamics. *Physical Review E*, 54(5):5134, 1996.

[99] CM Wijmans, B Smit, and RD Groot. Phase behavior of monomeric mixtures and polymer solutions with soft interaction potentials. *The Journal of Chemical Physics*, 114(17):7644–7654, 2001.

[100] Marieke Kranenburg, Maddalena Venturoli, and Berend Smit. Molecular simulations of mesoscopic bilayer phases. *Physical Review E*, 67(6):060901, 2003.

[101] Robert D Groot and KL Rabone. Mesoscopic simulation of cell membrane damage, morphology change and rupture by nonionic surfactants. *Biophysical journal*, 81(2):725–736, 2001.

[102] Robert D Groot, Patrick B Warren, et al. Dissipative particle dynamics: Bridging the gap between atomistic and mesoscopic simulation. *Journal of Chemical Physics*, 107(11):4423, 1997.

[103] Robert D Groot and Timothy J Madden. Dynamic simulation of diblock copolymer microphase separation. *The Journal of chemical physics*, 108(20):8713–8724, 1998.

[104] Dmitry A Fedosov, Igor V Pivkin, and George Em Karniadakis. Velocity limit in dpd simulations of wall-bounded flows. *Journal of Computational Physics*, 227(4):2540–2559, 2008.

[105] Igor V Pivkin and George Em Karniadakis. A new method to impose no-slip boundary conditions in dissipative particle dynamics. *Journal of Computational Physics*, 207(1):114–128, 2005.

[106] Amitesh Maiti and Simon McGrother. Bead–bead interaction parameters in dissipative particle dynamics: relation to bead-size, solubility parameter, and surface tension. *The Journal of chemical physics*, 120(3):1594–1601, 2004.

[107] PB Warren. Vapor-liquid coexistence in many-body dissipative particle dynamics. *Physical Review E*, 68(6):066702, 2003.

[108] Xijun Fan, Nhan Phan-Thien, Shuo Chen, Xuhong Wu, and Teng Yong Ng. Simulating flow of dna suspension using dissipative particle dynamics. *Physics of Fluids (1994-present)*, 18(6):063102, 2006.

[109] Y Shimizu, S Sawada, and KS Ikeda. Classical dynamical simulation of spontaneous alloying. *The European Physical Journal D-Atomic, Molecular, Optical and Plasma Physics*, 4(3):365–372, 1998.

[110] Sten Sarman and Denis J Evans. Heat flow and mass diffusion in binary lennard-jones mixtures. *Physical Review A*, 45(4):2370, 1992.

[111] R Qiao and P He. Simulation of heat conduction in nanocomposite using energy-conserving dissipative particle dynamics. *Molecular Simulation*, 33(8):677–683, 2007.

[112] P He and R Qiao. Self-consistent fluctuating hydrodynamics simulations of thermal transport in nanoparticle suspensions. *Journal of Applied Physics*, 103(9):094305, 2008.

[113] Frank J Alexander, Shiyi Chen, and JD Sterling. Lattice boltzmann thermohydrodynamics. *Physical Review E*, 47(4):R2249, 1993.

[114] Nikolaos I Prasianakis and Iliya V Karlin. Lattice boltzmann method for thermal flow simulation on standard lattices. *Physical Review E*, 76(1):016702, 2007.

[115] Wen-Shu Jiaung, Jeng-Rong Ho, and Chun-Pao Kuo. Lattice boltzmann method for the heat conduction problem with phase change. *Numerical Heat Transfer: Part B: Fundamentals*, 39(2):167–187, 2001.

[116] Subhash C Mishra and Hillol K Roy. Solving transient conduction and radiation heat transfer problems using the lattice boltzmann method and the finite volume method. *Journal of Computational Physics*, 223(1):89–107, 2007.

[117] Jinku Wang, Moran Wang, and Zhixin Li. A lattice boltzmann algorithm for fluid–solid conjugate heat transfer. *International journal of thermal sciences*, 46(3):228–234, 2007.

[118] Daniel Lüsebrink and Marisol Ripoll. Temperature inhomogeneities simulated with multiparticle-collision dynamics. *The Journal of chemical physics*, 136(8):084106, 2012.

[119] Zihan Tan, Mingcheng Yang, and Marisol Ripoll. Anisotropic thermophoresis. *Soft matter*, 13(40):7283–7291, 2017.

[120] Pep Español. Dissipative particle dynamics with energy conservation. *EPL (Europhysics Letters)*, 40(6):631, 1997.

[121] J Bonet Avalos and AD Mackie. Dissipative particle dynamics with energy conservation. *EPL (Europhysics Letters)*, 40(2):141, 1997.

[122] Eiyad Abu-Nada. Natural convection heat transfer simulation using energy conservative dissipative particle dynamics. *Physical Review E*, 81(5):056704, 2010.

[123] Toru Yamada, Anurag Kumar, Yutaka Asako, Otto J Gregory, and Mohammad Faghri. Forced convection heat transfer simulation using dissipative particle dynamics. *Numerical Heat Transfer, Part A: Applications*, 60(8):651–665, 2011.

[124] Zhen Li, Yu-Hang Tang, Huan Lei, Bruce Caswell, and George Em Karniadakis. Energy-conserving dissipative particle dynamics with temperature-dependent properties. *Journal of Computational Physics*, 265:113–127, 2014.

[125] Marisol Ripoll. Kinetic theory of dissipative particle dynamics models. *UNED, Spain*, 2002.

[126] Marisol Ripoll and Matthieu H Ernst. Model system for classical fluids out of equilibrium. *Physical Review E*, 71(4):041104, 2005.

[127] Toru Yamada, Shugo Itoh, Yohei Morinishi, and Shinji Tamano. Improving computational accuracy in dissipative particle dynamics via a high order symplectic method. *The Journal of chemical physics*, 148(22):224101, 2018.

[128] Martin Lísal, John K Brennan, and Josep Bonet Avalos. Dissipative particle dynamics at isothermal, isobaric, isoenergetic, and isoenthalpic conditions using shardlow-like splitting algorithms. *The Journal of chemical physics*, 135(20):204105, 2011.

[129] Ahmed-Amine Homman, Jean-Bernard Maillet, Julien Roussel, and Gabriel Stoltz. New parallelizable schemes for integrating the dissipative particle dynamics with energy conservation. *The Journal of chemical physics*, 144(2):024112, 2016.

[130] James P Larentzos, John K Brennan, Joshua D Moore, Martin Lísal, and William D Mattson. Parallel implementation of isothermal and isoenergetic dissipative particle dynamics using shardlow-like splitting algorithms. *Computer Physics Communications*, 185(7):1987–1998, 2014.

[131] Ricardo López-Ruiz and Xavier Calbet. Derivation of the maxwellian distribution from the microcanonical ensemble. *American Journal of Physics*, 75(8):752–753, 2007.

[132] Dirk Reith and Florian Müller-Plathe. On the nature of thermal diffusion in binary lennard-jones liquids. *The Journal of Chemical Physics*, 112(5):2436–2443, 2000.

[133] Sydney Chapman and Thomas George Cowling. *The mathematical theory of non-uniform gases: an account of the kinetic theory of viscosity, thermal conduction and diffusion in gases*. Cambridge university press, 1970.

[134] Leslie A Guildner. Thermal conductivity of gases. iii. some values of the thermal conductivities of argon, helium, and nitrogen from ∠0 c to ∠75 c at pressures of 1 x 105 to 2.5 x 107 pascals. *Journal of Research of the National Bureau of Standards-A. Physics and Chemistry*, 79, 1975.

[135] Howard JM Hanley, Robert D McCarty, and William M Haynes. The viscosity and thermal conductivity coefficients for dense gaseous and liquid argon, krypton, xenon, nitrogen, and oxygen. *Journal of Physical and Chemical Reference Data*, 3(4):979–1017, 1974.

[136] Hans Ziebland and JTA Burton. The thermal conductivity of liquid and gaseous oxygen. *British Journal of applied physics*, 6(12):416, 1955.

[137] SC Saxena and TKS Narayanan. Schmidt number for normal hydrogen and para-hydrogen. *Canadian Journal of Physics*, 40(4):527–530, 1962.

[138] EB Winn. The self-diffusion coefficient of nitrogen. *Physical Review*, 74(6):698, 1948.

[139] J Kestin, K Knierim, EA Mason, B Najafi, ST Ro, and M Waldman. Equilibrium and transport properties of the noble gases and their mixtures at low density. *Journal of physical and chemical reference data*, 13(1):229–303, 1984.

[140] Elnaz Zohravi, Ebrahim Shirani, and Ahmadreza Pishevar. Influence of the conservative force on transport coefficients in the dpd method. *Molecular Simulation*, 44(3):254–261, 2018.

[141] JR Henderson and Frank van Swol. On the interface between a fluid and a planar wall: theory and simulations of a hard sphere fluid at a hard wall. *Molecular Physics*, 51(4):991–1010, 1984.

[142] R Golestanian, TB Liverpool, and A Ajdari. Designing phoretic micro-and nano-swimmers. *New Journal of Physics*, 9(5):126, 2007.

[143] Masao Doi and Samuel Frederick Edwards. *The theory of polymer dynamics*, volume 73. oxford university press, 1988.

[144] Klemen Bohinc, Aleš Iglič, and Tomaž Slivnik. *Linearized Poisson Boltzmann theory in cylindrical geometry*. 2008.

[145] R Piazza and A Parola. Thermophoresis in colloidal suspensions. *Journal of Physics: Condensed Matter*, 20(15):153102, 2008.

[146] Kyriakos A Eslahian, Arghya Majee, Michael Maskos, and Alois Würger. Specific salt effects on thermophoresis of charged colloids. *Soft Matter*, 10(12):1931–1936, 2014.

[147] Stefan Duhr and Dieter Braun. Why molecules move along a temperature gradient. *Proceedings of the National Academy of Sciences*, 103(52):19678–19682, 2006.

[148] Daniel Lüsebrink. *Colloidal Suspensions in Temperature Gradients with Mesoscopic Simulations*. PhD thesis, Universität zu Köln, 2011.

[149] Alois Würger. Thermal non-equilibrium transport in colloids. *Reports on Progress in Physics*, 73(12):126601, 2010.

[150] Moubin Liu, Paul Meakin, and Hai Huang. Dissipative particle dynamics with attractive and repulsive particle-particle interactions. *Physics of Fluids*, 18(1):017101, 2006.

[151] Moubin Liu, Paul Meakin, and Hai Huang. Dissipative particle dynamics simulation of multiphase fluid flow in microchannels and microchannel networks. *Physics of Fluids*, 19(3):033302, 2007.

[152] Henrique Moyses, Jérémie Palacci, Stefano Sacanna, and David G Grier. Trochoidal trajectories of self-propelled janus particles in a diverging laser beam. *Soft Matter*, 12(30):6357–6364, 2016.

[153] Thomas Bickel, Arghya Majee, and Alois Würger. Flow pattern in the vicinity of self-propelling hot janus particles. *Physical Review E*, 88(1):012301, 2013.

[154] Zhiguang Wu, Tieyan Si, Wei Gao, Xiankun Lin, Joseph Wang, and Qiang He. Superfast near-infrared light-driven polymer multilayer rockets. *Small*, 12(5):577–582, 2016.

[155] Ruo-Yu Dong, Yi Zhou, Chun Yang, and Bing-Yang Cao. Translational thermophoresis and rotational movement of peanut-like colloids under temperature gradient. *Microfluidics and Nanofluidics*, 19(4):805–811, 2015.

[156] Juan Ruben Gomez-Solano, Sela Samin, Celia Lozano, Pablo Ruedas-Batuecas, René Roij, and Clemens Bechinger. Tuning the motility and directionality of self-propelled colloids. *Scientific Reports*, 7(1):14891, 2017. DOI: https://doi.org/10.1038/s41598-017-14126-0.

[157] Alois Würger. Self-diffusiophoresis of janus particles in near-critical mixtures. *Physical review letters*, 115(18):188304, 2015.

[158] Roy Stanley Burdon. *Surface tension and the spreading of liquids*. Cambridge University Press, 2014.

[159] Shigeo Maruyama, Tatsuto Kimura, and Ming-Chang Lu. Molecular scale aspects of liquid contact on a solid surface. In *National Heat Transfer Symposium of Japan*, volume 2, pages 577–578. Japan Heat Transfer Society; 1999, 2002.

[160] Sochi Matsumoto, Shigeo Maruyama, and Hideki Saruwatari. Molecular dynamics simulation of a liquid droplet on a solid surface. *Japanese Journal of Tribology*, 42:143–152, 1997.

[161] Aurélien F Stalder, Tobias Melchior, Michael Müller, Daniel Sage, Thierry Blu, and Michael Unser. Low-bond axisymmetric drop shape analysis for surface tension and contact angle measurements of sessile drops. *Colloids and Surfaces A: Physicochemical and Engineering Aspects*, 364(1-3):72–81, 2010.

[162] Sabrina Simoncelli, Samuel Johnson, Franziska Kriegel, Jan Lipfert, and Jochen Feldmann. Stretching and heating single dna molecules with optically trapped gold–silica janus particles. *Acs Photonics*, 4(11):2843–2851, 2017.

Appendix A

Distribution Function in Microcanonical Ensemble

We consider an isolated system with N number of particles and total energy E. In statistical mechanics, this system is called the microcanonical ensemble. If Ω shows the number of microstate in the system (microscopic configurations) and all of the microstates is equally probable, the entropy is obtained by $S = k_B \ln(\Omega)$. The total entropy can be expressed by $S = \sum_i s(\varepsilon_i)$ where $s(\varepsilon_i)$ is entropy of $i-$th particle which carries energy ε_i. The simplest case is for an ideal solid which mechanical energy is zero and total energy obtains from $E = \sum_i \varepsilon_i$. A microstate with that each particle carries the special amount of energy is $\Omega(\varepsilon_1, \varepsilon_2, ..) = \mathrm{e}^{\sum s_i(\varepsilon_i)/k_B}$. Therefore the total number of microstate is given by:

$$\Omega(E,N) = \sum_j \Omega_j = \int_0^E \mathrm{e}^{\sum s_i(\varepsilon_i)/k_B} \delta\left(\sum_i \varepsilon_i - E\right) \mathrm{d}\varepsilon_1 \mathrm{d}\varepsilon_2 \cdots \mathrm{d}\varepsilon_N \tag{A.1}$$

The entropy of a particle is related to the internal energy by the fundamental thermodynamic relation: $\mathrm{d}s_i(\varepsilon_i)/\mathrm{d}\varepsilon_i = T^{-1}$. On the other hand, we chose $\varepsilon_i = c_v T_i$. Hence the internal energy and entropy of a particle are related by $s_i(\varepsilon_i) = c_v \ln(\varepsilon_i)$. By substituting this relation in the equation A.1:

$$\begin{cases} \Omega(E,N) & = \int_0^E \varepsilon_1^{c_v/k_B} \cdots \varepsilon_N^{c_v/k_B} \delta\left(\sum_i \varepsilon_i - E\right) \mathrm{d}\varepsilon_1 \mathrm{d}\varepsilon_2 \cdots \mathrm{d}\varepsilon_N \\ & = E^{N(1+c_v/k_B)-1} \int_0^1 x_1^{c_v/k_B} \cdots x_N^{c_v/k_B} \delta\left(\sum_i \varepsilon_i - E\right) \mathrm{d}x_1 \cdots \mathrm{d}x_N \\ & = E^{N(1+c_v/k_B)-1} \widetilde{\Omega}(N) \end{cases} \tag{A.2}$$

The probability that the system is found in the state with $\varepsilon_1, \varepsilon_2, \cdots, \varepsilon_N$ is given by the number of states under the condition $\varepsilon_1, \varepsilon_2, \cdots, \varepsilon_N$ over the total number of state:

$$P(\varepsilon_1, \varepsilon_2, \cdots, \varepsilon_N) = \frac{\Omega(\varepsilon_1, \varepsilon_2, \cdots, \varepsilon_N)}{\Omega_{tot}} = \frac{e^{\sum_i s_i(\varepsilon_i)/k_B}}{\Omega_{tot}} \delta\left(\sum_i \varepsilon_i - E\right) \tag{A.3}$$

The distribution function $\psi(\varepsilon_{i_0})$ gives the probability that a particle with the index of i_0 carries the energy ε_{i_0}. Equations A.2 and A.3 give:

$$\begin{cases} \psi(\varepsilon_{i_0}) & = \int_0^E P(\varepsilon_1, \varepsilon_2, \cdots, \varepsilon_N) \mathrm{d}\varepsilon_1 \cdots \mathrm{d}\varepsilon_{i_0-1} \mathrm{d}\varepsilon_{i_0+1} \cdots \mathrm{d}\varepsilon_N \\ & = \frac{\varepsilon_{i_0}^{c_v/k_B}}{E^{c_v/k_B+1}} \left(\frac{E-\varepsilon}{E}\right)^{(N-1)(c_v/k_B+1)-1} \frac{\widetilde{\Omega}(N-1)}{\widetilde{\Omega}(N)} \end{cases} \tag{A.4}$$

The normalization $\int_0^E \psi(\varepsilon)\mathrm{d}\varepsilon = 1$ gives $\frac{\widetilde{\Omega}(N)}{\widetilde{\Omega}(N-1)} = B(x,y)$ where $x = c_v/k_B + 1, y = (N-1)(c_v/k_B+1)$ and $B(x,y)$ is Beta function and it is related to the gamma function by: $B(x,y) = \Gamma(x)\Gamma(y)/\Gamma(x,y)$. The final result of distribution function is:

$$\psi(\varepsilon) = \frac{\Gamma(N(c_v/k_B+1))}{\Gamma(c_v/k_B+1)\Gamma((N-1)(c_v/k_B+1)} \frac{1}{E} \left(\frac{\varepsilon}{E}\right)^{c_v/k_B} \left(1-\frac{\varepsilon}{E}\right)^{(N-1)(c_v/k_B+1)-1} \tag{A.5}$$

Appendix B

Colloid-Solvent Boundary Conditions

In order to set the proper dissipative force coefficient γ, we assume there is a flow in the $x-$direction parallel to the plane. A particle with index of i is on the plane and j is a particle in the fluid which interacts with i. See figure B.1.

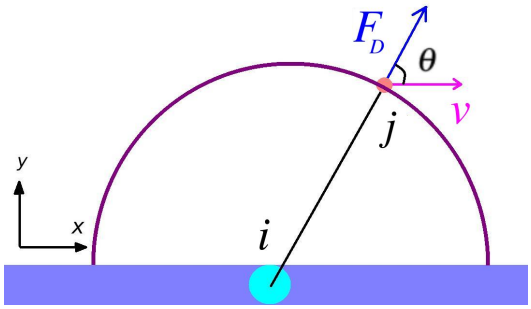

Fig. B.1

Total shear force **F** due to the flow is parallel to the plane and it is related to the shear stress in 2 dimensional system by $F = \tau L$ where L is the length of the wall. In the incompressible and Newtonian fluid shear stress is given by $\tau = \eta\dot{\gamma} = \eta v/y$. On the other hand, the total force on flat plane in the parallel direction to it due to the dissipative force $F_{||}^D = \mathbf{F}^D.\hat{x}$ is:

$$F = N_L \int_A ng(r)F_{||}^D \mathrm{d}A \tag{B.1}$$

Which N_L is a number of particles on the plane in length of L, and $g(r)$ is radial distribution function and $\mathrm{d}A$ is surface element that fluid particle exist in there and $\mathrm{d}A = r\mathrm{d}r\mathrm{d}\theta$ where r is in the range of cut-off radius r_c and θ is $0 < \theta < \pi$. The dissipative force is given by

equation 2.17. Therefore in the cutoff range:

$$F_{||}^{D} = -\gamma_{FC}\left(1 - r/r_c\right)^{2s}\left(\mathbf{v}_{ij}\cdot\hat{\mathbf{r}}_{ij}\right)\left(\hat{\mathbf{r}}_{ij}\cdot\hat{x}\right) \tag{B.2}$$

$$= -\gamma_{FC}\left(1 - r/r_c\right)^{2s}\dot{\gamma}y\cos(\theta)\cos(\theta) \tag{B.3}$$

$$= -\gamma_{FC}\left(1 - r/r_c\right)^{2s}\dot{\gamma}r\sin(\theta)\cos^2(\theta) \tag{B.4}$$

In the absence of conservative interactions between colloid-fluid radial distribution function is given by $g(r) = 1.0$, therefore:

$$\gamma_{FC} = \frac{3\eta}{2nn_c\int_0^{r_c} r^2(1 - r/r_c)^{2s}dr} \tag{B.5}$$

Where n and n_c are respectively number density of fluid in the area and the colloid's particle density in length and s is the exponent of equation 4.1.

Erklärung

Ich versichere, dass ich die von mir vorgelegte Dissertation selbständig angefertigt, die benutzten Quellen und Hilfsmittel vollständig angegeben und die Stellen der Arbeit einschließlich Tabellen, Karten und Abbildungen, die anderen Werken im Wortlaut oder dem Sinn nach entnommen sind, in jedem Einzelfall als Entlehnung kenntlich gemacht habe; dass diese Dissertation noch keiner anderen Fakultät oder Universität zur Prüfung vorgelegen hat; daß sie abgesehen von unten angegebenen Teilpublikationen noch nicht veröffentlicht worden ist sowie, dass ich eine solche Veröffentlichung vor Abschluss des Promotionsverfahrens nicht vornehmen werde. Die Bestimmungen dieser Promotionsordnung sind mir bekannt. Die von mir vorgelegte Dissertation ist von Prof. Dr. Gerhard Gompper betreut worden.

Jülich, den 10.03.2019

Personal Details

Full name	Fatemeh Alidadi Soleymani
Email	alidadi.fatemeh@gmail.com
Date of Birth	December 6, 1989
Citizenship	Iran

Education

10/2015–present	**PhD in Physics**, *Forschungszentrum Jülich*, Jülich, Germany *PhD Thesis*: Mesoscopic modeling of a thermophoretic swimmer
10/2012–2/2015	**MSc in Soft Condensed Matter Physics**, *Sharif University of Technology,*, Tehran, Iran,18.5 on a 20 scale *Master Thesis*: Simulation of phase behavior of discotic liquid crystals.
10/2008–10/2012	**BSc in Physics**, *Isfahan University of Technology,* Isfahan, Iran, 19 on a 20 scale *Bachelor Thesis*: Behavior of correlated-electrons in optical lattices.

Jülich, 10.03.2019